Université du Québec

Institut National de la Recherche Scientifique

Centre Énergie, Matériaux et Télécommunications (INRS-EMT)

High Pulse-to-Pulse Stability High Power Femtosecond Yb-doped Fiber Laser

By

Javad Soltanian

A thesis submitted for the achievement of the degree of

Master of Science, M.Sc

in Energy and Materials Sciences

Jury Members

President of the jury and Internal Examiner	José Azaña *INRS-EMT*
External Examiner	Feruz Ganikhanov *University of Rhode Island*
Director of Research	François Légaré *INRS-EMT*

DEDICATION

This thesis is dedicated to my beloved

Parents

&

Siblings

ACKNOWLEDGEMENTS

I was lucky enough to perform my master's degree at the Institut National de la Recherche Scientifique (INRS) at the Université du Québec. My deepest gratitude goes to my supervisor Prof. Francois Légaré. I am grateful to him for choosing me for the master's program and providing me with a full scholarship for the duration of my studies. I am truly grateful and appreciative of the opportunity to join his team. I believe his patience and direction facilitated my entry into this sector. Moreover, his insightful remarks prompted me to refine my thoughts and elevate the quality of my work.

During my study, I have received a great deal of support and assistance from my brother Dr. Reza Soltanian who introduced me to INRS and the Ultra-Fast Science and Technology group. He is always happy to share his experience with me and I have learned a lot from him. I owe a debt of gratitude to him.

Finally, I would like to thank my whole family, especially my parents, for providing me with unfailing support and continuous encouragement my entire life. Throughout my years of study and life, I have received support from them. I sincerely appreciate all your excellent assistance in helping me get to this stage.

This master thesis has been carried out at Institute National of Scientific Research (INRS) with cooperation of O/E Land company and several people deserve recognition for their support and help, and I would appreciate all of them for their support.

Javad Soltanian, Winter, 2023

ABSTRACT

While completing my degree at INRS, I have worked on generating, high pulse-to-pulse (P2P) stability high power femtosecond ytterbium-doped-fiber laser at 1064 nm wavelength for second harmonic generation (SHG) microscopy application.

Stability measurement of ultrashort optical pulses in real-time is crucial for numerous applications such as frequency comb generation, arbitrary optical waveform generation, timing, and frequency distribution by optical fiber links. Strong demand exists for reliable femtosecond lasers at 1 μm wavelength for imaging applications in the medical field, especially wide-field SHG microscopy using a high average power (more than 4 W) and high-repetition-rate (in the range of MHz) laser oscillator to achieve high-speed imaging over a large area.

This thesis gives a comprehensive investigation of passively mode-locked Yb-doped polarization-maintaining fiber lasers operating in all-normal dispersion (ANDi) domain at 1.06 μm wavelength region.

The stable mode-locking operation in seed is a result of utilizing a uniform fiber Bragg grating (FBG) with a bandwidth of 0.2 nm, minimizing the cavity length and a semiconductor saturable absorber mirror (SESAM), to limit the pulse fluence of the generated pulse train so that not exceeding 3 times the saturation fluence of the saturable absorber (SA). The average output power, pulse width and repetition rate of 14 mW, 10 ps and 42 MHz was achieved respectively from the seed corresponding to the pulse fluence of about 200 μJ/cm^2. The generated pulse was then directly amplified by a two-stage single mode (SM) amplifier and one stage high power post amplification to reach more than 10 W of average output power. Since the peak power of the pulse in the post-amplifier is high, self-phase modulation (SPM) occurs leading to the broadening of the bandwidth to about 20 nm. The compression from 10 ps to about 200 fs was achieved by a transparent grating pair with groove density of 1,000 Grooves/mm. For measuring pulse to pulse fluctuations, the average output power of collimated beam from 7 W to sub 100 mW was decreased by using a polarizer and half wave plate as an attenuator. Then, the histogram chart was used to measure more than one million pulse amplitudes by a 40 GSA/s oscilloscope.

In conclusion, the P2P stability of about 2.4%and 3.4% was realized for the seed and output of 1,064 nm mode locked fiber laser respectively. A pulse duration of 210 fs was achieved in a linear-cavity YDF laser running at a fundamental repetition rate of 42 MHz and average output power of 7 W, using SPM from the post-amplifier.

Keywords: Nonlinear pulse propagation; pulse-to-pulse stability; Self-phase modulation (SPM); femtosecond fiber laser; Second harmonic generation microscopy; Fiber laser, Passive mode-locking, Saturable absorber, Yb-doped fiber, Polarization maintaining fiber.

RÉSUMÉ

Au cours de ma maîtrise à l'INRS, j'ai travaillé sur la génération d'un laser femtoseconde à fibre dopée à l'Ytterbium (Yb) de haute puissance et de grande stabilité d'impulsion à impulsion (IAI) à une longueur d'onde de 1064nm pour une application de microscopie par génération de seconde harmonique (GSH).

La mesure de la stabilité des impulsions optiques ultracourtes en temps réel est cruciale pour diverses applications telles que la génération de peignes de fréquence, la génération de formes d'ondes optiques arbitraires, la synchronisation, la distribution de fréquence par les liaisons par fibre optique et une forte demande existe pour des lasers femtosecondes fiables à une longueur d'onde de 1µm pour les applications d'imagerie dans le domaine médical, en particulier la microscopie GSH à grand champ utilisant un oscillateur laser à haute puissance moyenne (plus de 4W) et à haut taux de répétition (dans la gamme de MHz) pour obtenir une imagerie à grande vitesse sur une grande surface.

Cette thèse présente une étude complète des lasers à fibre à maintien de polarisation dopés à l'Yb, à verrouillage de mode passif, fonctionnant dans le domaine de la dispersion entièrement normale (DiEN) dans la région de longueur d'onde de 1,06µm.

Le fonctionnement stable du verrouillage de mode en « germe » est le résultat de l'utilisation d'un réseau de Bragg de fibre (FBG) uniforme de 0,2 nm, de la minimisation de la longueur de la cavité et d'un miroir semi-conducteur à absorbant saturable (MSESA) pour limiter la fluence d'impulsion du train d'impulsions généré afin de ne pas dépasser 3 fois la fluence de saturation de l'absorbeur saturable (AS). La puissance de sortie moyenne, la largeur d'impulsion et la fréquence de répétition de 14mW, 10ps et 42MHz ont été obtenues respectivement à partir de la « germe » correspondant à la fluence d'impulsion d'environ 200µJ/cm2. L'impulsion générée a ensuite été directement amplifiée par un amplificateur monomode (AM) à deux étages et une post-amplification haute puissance à un étage pour atteindre plus de 10W de puissance de sortie moyenne. Comme la puissance de crête de l'impulsion dans le post-amplificateur est élevée, une auto-modulation de phase (AMP) se produit, ce qui entraîne un élargissement de la bande passante à environ 20 nm. La compression de 10ps à environ 200fs a été obtenue par une paire de réseaux transparents avec une densité de 1000 rainures/mm. Pour mesurer les fluctuations d'une impulsion à l'autre, la puissance de sortie moyenne du faisceau collimaté de 7W à moins de 100mW a été réduite en utilisant un polariseur et une plaque demi-onde comme atténuateur. Ensuite, le graphique de l'histogramme a été représenté pour la mesure de l'amplitude de plus d'un million d'impulsions par un oscilloscope 40GSA/s.

En conclusion, la stabilité IAI d'environ 2,4 et 3,4 pour cent a été réalisée pour le « germe » et la sortie du laser à fibre à verrouillage de mode 1064nm respectivement. Une durée d'impulsion de 210fs a été obtenue dans un laser YDF à cavité linéaire fonctionnant à une fréquence de répétition fondamentale de 42MHz et une puissance de sortie moyenne de 7W, en utilisant le AMP du post-amplificateur.

Mots-clés : Propagation non linéaire des impulsions ; stabilité d'une impulsion à l'autre ; auto-modulation de phase (AMP) ; laser à fibre femtoseconde ; microscopie à génération de seconde harmonique ; laser à fibre, verrouillage de mode passif, absorbeur saturable, fibre dopée à l'Yb, fibre à maintien de polarisation.

SYNOPSIS

Au cours de ma maîtrise, sous la supervision du professeur François Légaré, j'ai travaillé sur un sujet lié à la génération, la caractérisation et les applications d'impulsions laser ultra-courtes à fibre. Avant ma maîtrise, j'avais une expérience très limitée en optique et ce projet auquel j'ai participé au cours des deux dernières années m'a permis d'acquérir une expérience en optique non linéaire. Plus précisément, le sujet sur lequel j'ai travaillé est la génération d'un laser femtoseconde à fibre dopée à l'ytterbium de haute stabilité d'impulsion à impulsion (IAI) et de haute puissance à une longueur d'onde de 1064nm pour une application de microscopie par génération de seconde harmonique (GSH).

Les lasers femtoseconde à fibre à verrouillage de mode jouent un rôle indispensable dans la télémétrie spatiale, l'ophtalmologie, la spectroscopie térahertz, le micro-usinage des matériaux, etc. En plus de leurs applications dans la recherche scientifique, les lasers à fibre ultrarapides sont également pratiques pour la vie quotidienne : les lasers à fibre ultrarapides sont capables de générer des impulsions femtosecondes avec une puissance de crête élevée et un large spectre, qui peuvent être utilisés comme source de lumière pour les systèmes d'imagerie optique non linéaire dans le domaine biomédical [1]. Il ne s'agit pas seulement d'un outil important permettant aux gens d'explorer le monde, mais aussi d'un domaine pilier de la technologie laser.

Cette thèse présente la génération d'impulsions femtosecondes à l'aide d'un laser à fibre ultrarapide à verrouillage de mode passif. L'étude fournie dans cette thèse s'inscrit dans deux catégories de recherche principales. Premièrement, présenter un examen complet du laser à fibre à maintien de polarisation (MP) à mode passif fonctionnant dans la région de longueur d'onde de 1μm. Ensuite, nous avons prouvé les caractéristiques d'impulsion d'un laser basé sur un miroir semi-conducteur d'absorption saturable (MSESA) avec une cavité linéaire. Des techniques standard de caractérisation des impulsions ultracourtes ont été utilisées pour diagnostiquer les comportements du laser. Le spectre optique et le spectre RF ont également été examinés. Les schémas laser proposés dans cette étude utilisaient une fibre active dopée à l'Yb comme milieu de gain et fonctionnaient dans tous les régimes de dispersion normale. Des expériences ont été menées sur le laser MSESA à cavité linéaire proposé dans une région à verrouillage de mode. Dans la deuxième section de cette thèse, des études de microscopie non linéaire sont rapportées comme une application de ce laser. Nous allons ici passer brièvement en revue chacun de ces sujets.

I. Laser femtoseconde à fibre dopée à l'ytterbium à haute stabilité d'impulsion à impulsion (IAI) et à haute puissance

En 1960, *Theodore Maiman* a développé le premier laser à rubis, et le prototype du laser à fibre est également apparu dans les années 1960. Par la suite, *Diabolize et al.* [46] ont introduit le concept de laser à fibre pulsé en 1983. Si l'on considère les régions à impulsions courtes et ultracourtes (impulsions de quelques picosecondes ou moins), l'utilisation des lasers à fibre pour la création d'impulsions était le deuxième défi le plus difficile à relever pour les chercheurs. En effet, le confinement de la lumière dans un volume restreint influe sur l'évolutivité de la puissance de sortie des lasers à fibre, car il se traduit généralement par diverses caractéristiques non linéaires. En utilisant des lasers à fibre active hautement dopés et l'amplification d'impulsions chirpées, des lasers à fibre ultrarapides de forte puissance ont été créés en 1990 [47].

Les lasers à fibre pulsés sont utilisés dans de nombreux secteurs, notamment la communication optique, l'imagerie médicale [48], la spectroscopie [49], le dépôt par laser pulsé, la métrologie de précision et la microconcordance [50], et bien d'autres encore. En tant que sources laser potentielles et puissantes, les lasers à fibres influencent l'évolution des applications laser. Les lasers à fibre haute performance et haute fonctionnalité ont des propriétés avantageuses qui les rendent indispensables dans une variété d'applications pratiques. Les progrès technologiques ont accéléré le développement de nouvelles technologies laser, et les inventions efficaces sont très demandées.

En raison de ses diverses caractéristiques, le laser à fibre est considéré comme l'un des types de laser les plus prometteurs actuellement disponibles. En raison de leur capacité à générer diverses longueurs d'onde, les lasers à fibre sont largement utilisés dans les applications industrielles. Les lasers à fibre sont très polyvalents ; ils peuvent donc être utilisés dans de nombreux contextes, notamment industriels, médicaux et de communication. En plus de toutes les qualités énumérées ci-dessus, les lasers à fibre sont excellents en raison de leur petite taille, de leur longue durée de vie, de leur capacité à offrir une puissance de sortie élevée, de leur grande fiabilité et de la qualité irréprochable de leur faisceau [51].

Deux mécanismes peuvent être appliqués pour produire des impulsions ultracourtes dans les lasers à fibre : La technique de Q-switching [2, 3] et celle du mode-locking [4-6]. Les lasers à fibre à verrouillage de mode sont maintenant disponibles dans une gamme de longueurs d'onde, utilisant généralement l'Ytterbium (Yb), l'Erbium (Er) ou le Thulium (Tm) comme dopants de terre rare. Chacun de ces dopants présente des avantages et des inconvénients. Par exemple, la fibre SMF28 présente une dispersion anormale à 1,55 micron, ce qui rend relativement simple le verrouillage de mode des lasers à fibre dopée à l'Er en utilisant la propagation par soliton [7]. La largeur d'impulsion générée par la technique de Q-switching est généralement de l'ordre de la nanoseconde, tandis que la largeur d'impulsion générée par la technique de verrouillage de mode peut atteindre le niveau de la femtoseconde. Par conséquent, les lasers à fibre ultrarapides peuvent également être appelés lasers à fibre à verrouillage de mode ultrarapides. Ils se composent de quatre parties : 1) une source de pompage ; 2) un réseau de fibres ou un miroir de fibres comme réflecteur pour former une cavité résonnante ; 3) des fibres dopées aux terres rares comme milieu de gain ; 4) un dispositif de modulation à verrouillage de mode. Le dispositif de modulation à verrouillage de mode est considéré comme le cœur d'un laser à fibre à verrouillage de mode, qui détermine les paramètres caractéristiques des impulsions à verrouillage de mode.

1- Source de pompe

Les lasers à fibre, comme tous les autres systèmes laser, nécessitent une source d'excitation pour pomper l'énergie dans le système. Cela se fait par pompage de la fibre optique. Cette source peut être connectée à une fibre à grand cœur qui est ensuite fusionnée en une fibre à double gaine. La double gaine permet à la fibre multimode de haute puissance d'être guidée dans le grand cœur extérieur en même temps que le laser monomode s'accumule dans le petit cœur intérieur. Selon le matériau de gain dont la fibre est dopée, la bande d'absorption peut être large ou étroite, ce qui signifie que dans certains cas, les diodes laser traditionnelles à haute puissance sont acceptables, mais dans d'autres cas, des diodes à longueur d'onde stabilisée sont nécessaires. Dans ce travail, nous avons utilisé la lumière de pompage d'une diode laser à fibre monomode de 400mW émettant à 976nm pour les étapes d'amorçage et de pré-amplification et des pompes multimodes de 10W-976nm pour l'alimentation de l'étape d'amplification de puissance.

2- Réseaux de Bragg fibré (RBF) and réseaux de Bragg fibré chirpé (RBFC)

Une perturbation périodique ou apériodique de l'indice de réfraction effectif dans le cœur d'une fibre optique constitue un réseau de Bragg de fibre décrit à la figure 2.14. En général, la perturbation est grossièrement périodique sur une longueur donnée, par exemple quelques millimètres ou centimètres, et la période est de l'ordre de centaines de nanomètres, voire beaucoup plus pour les réseaux de fibres à longue période. Pour de courts intervalles de temps de modulation de l'indice, la perturbation de l'indice de réfraction entraîne la réflexion de la lumière dans une petite gamme de longueurs d'onde satisfaisant la condition de Bragg calculée par l'équation 2.5. Cette condition stipule essentiellement que le nombre d'onde du réseau correspond à la différence entre les vecteurs d'onde (opposés) des ondes incidente et réfléchie. Dans cette situation, les amplitudes complexes correspondant aux contributions du champ réfléchi provenant des différentes régions du réseau sont en phase et peuvent donc s'additionner de manière constructive ; il s'agit d'une forme de correspondance de phase. Si le réseau est suffisamment long, même une faible modulation de l'indice est suffisante pour obtenir une réflexion presque complète. Les autres longueurs d'onde de la lumière qui ne satisfont pas à la condition de Bragg ne sont pratiquement pas affectées par le réseau de

Bragg, à l'exception des lobes latéraux qui apparaissent fréquemment dans le spectre de réflexion. La largeur de bande de réflexion du réseau de fibres est influencée à la fois par la longueur et l'intensité de la modulation de l'indice de réfraction. Les réseaux longs avec une faible modulation de l'indice produisent les valeurs de bande passante les plus étroites, qui conviennent à des applications telles que la production de lasers à fibre à fréquence unique et de filtres optiques spécifiques, comme le montre la figure 2.15. De grandes largeurs de bande peuvent être obtenues non seulement avec des réseaux courts et robustes, mais aussi avec des modèles plus longs et apériodiques [125].

Les RBFC peuvent être utilisés pour compenser la dispersion des guides d'ondes à fibres optiques. Lorsqu'ils sont utilisés en mode réflexion (contrairement au mode transmission), ces réseaux de Bragg présentent une dispersion importante. De plus, le signe de la dispersion en mode réflexion est facilement contrôlable. Ensemble, ces deux caractéristiques suggèrent l'utilisation de réseaux de Bragg chirpé pour la compensation de la dispersion dans les systèmes à fibres optiques [8].

3- Fibré dopes à terres rares

Le cœur de la fibre optique peut être rendu actif et utilisé pour diriger et amplifier la lumière dans les lasers ultrarapides en le dopant avec des éléments actifs pour le laser [90]. Les fibres dopées aux terres rares ont été découvertes dans les années 1960, et cette découverte a permis de créer de nouveaux lasers avec une qualité de faisceau parfaite. Les applications à base de fibres actives gagnent en popularité, notamment dans les domaines des télécommunications, de la microscopie non linéaire et du traitement des matériaux [91]. Les éléments de terres rares, notamment l'ytterbium (Yb), l'erbium (Eb) et le thulium, constituent les ions dopants. En se connectant à des verres et des cristaux présentant une efficacité d'absorption et d'émission plus élevée, les structures électroniques de ces éléments permettent la création d'atomes triplement ionisés [92]. Par conséquent, les fibres deviennent actives lorsqu'elles sont dopées avec ces matériaux. La caractéristique la plus fascinante de ces fibres spécialisées est leur capacité à absorber les photons pompés, qui sont normalement de plus courte longueur d'onde, et à exciter les électrons dans des états métastables, ce qui permet d'augmenter l'intensité de la lumière en stimulant l'émission [93].

4- Verrouillage de mode

Il existe deux types de méthodes de verrouillage de mode : le verrouillage de mode actif et le verrouillage de mode passif, qui dépendent de l'existence ou non d'une intervention externe. Le verrouillage de mode actif contrôle les paramètres de la cavité résonante par un signal périodique externe. La méthode habituelle consiste à incorporer un absorbeur saturable dans la cavité du laser et à utiliser ses caractéristiques d'absorption non linéaire, que nous avons utilisées pour générer un laser à fibre pulsé stable dans cette thèse. Si l'impulsion traverse l'absorbeur saturable, la consommation de la partie centrale à haute intensité est faible, et la perte de la partie à faible intensité des deux extrémités est importante, ce qui permet d'obtenir l'effet de rétrécissement de l'impulsion. Les absorbeurs saturables peuvent être divisés en deux catégories : les absorbeurs saturables artificiels, basés sur l'effet d'interférence non linéaire de la fibre, et les absorbeurs saturables réels, basés sur les propriétés d'absorption saturable non linéaire des matériaux.

Le verrouillage passif du mode génère des impulsions en insérant l'absorbeur saturable (AS) dans le résonateur laser, ce qui est une technique plus efficace pour générer des impulsions femtosecondes ultracourtes. L'absorbeur saturable joue un rôle décisif dans la performance des impulsions ; il comprend des absorbeurs saturables artificiels et des absorbeurs saturables réels.

Le MSESA est un type d'absorbeur saturable réel qui est apparu au début des années 1990. Depuis lors, de nombreux chercheurs ont étudié ses applications dans les lasers à fibre à verrouillage de mode passif [9-12]. Sa structure de base comprend le réflecteur de Bragg (qui réagit aux caractéristiques spectrales) et des matériaux avec des caractéristiques d'absorption dépendantes de l'intensité (qui absorbent la lumière à une longueur d'onde spécifique) [13]. Parce qu'il n'a rien à voir avec l'état de polarisation, le laser à fibre à verrouillage de mode MSESA a non seulement une bonne stabilité, mais aussi une forte capacité à résister aux interférences du milieu environnant. Le temps de réponse de récupération du MSESA est très lent, ce qui rend difficile la génération d'impulsions femtosecondes par les lasers à fibre à verrouillage de mode basés sur le SESAM. En tant qu'élément de verrouillage de mode, le seuil d'endommagement du MSESA est relativement bas, et il est facile de le détruire à haute puissance.

Dans ce travail, un laser à fibre dopée à l'Ytterbium (LFPY) verrouillé en mode utilisant un RBF uniforme et un MSESA commercial dans une cavité à structure linéaire est généré. Le montage expérimental de la graine est présenté à la figure 4.2. Le MSESA avec une fluence de saturation de 130 µJ/cm2 et un temps de récupération de ~500fs qui garantissent l'auto-démarrage et un verrouillage de mode stable est connecté au port de signal du multiplexage par répartition en longueur d'onde (MLD) et la lumière de pompage d'une diode laser monomode à fibre de 400mW émettant à 976 nm est lancée dans la cavité linéaire par épissure au port de pompage du MLD. Une fibre à maintien de polarisation (MP) dopée à l'Yb, d'une longueur de 60 centimètres, avec une absorption de cœur d'environ 400 dB/m à 976 nm, est connectée au port commun du MLD. A l'extrémité de la fibre active, un coupleur 50:50 sépare le signal et 50% est utilisé pour le RBF et la terminaison libre de la fibre à l'extrémité du FBG est coupée en angle pour réduire les réflexions indésirables. Le RBF uniforme est inscrit dans le cœur d'une fibre MP. Le RBF a un pic de réflectance d'environ 99%, centré à 1064nm avec une largeur de bande spectrale de 0,38nm. Deux isolateurs PM sont connectés à la sortie du coupleur pour garantir une transmission unidirectionnelle de la lumière et éviter toute réflexion vers la graine principale. À l'aide d'un analyseur de spectre optique (ASO), d'un oscilloscope 40GSA/s et d'un photodétecteur unique, le spectre et le train d'impulsions du laser à verrouillage de mode sont mesurés simultanément. Le spectre radiofréquence (RF) du laser à fibre est contrôlé à l'aide d'un analyseur de spectre. Le taux de répétition de 42 MHz est atteint, ce qui, selon l'équation (3.23), correspond bien à la longueur de la cavité, comme le montre le train d'impulsions de la figure 4.3.a, la trace d'autocorrélation de l'impulsion générée est mesurée à environ 10ps en largeur totale et demi-maximum (LTDM) en utilisant l'autocorrélateur FR-103WS comme le montre la figure 4.3.b, le laser a obtenu un rapport signal/bruit exceptionnel de 90dB comme le montre la figure 4.3.c. Le spectre d'émission du laser est illustré à la figure 4.3.d. La longueur d'onde centrale est de 1064 nm avec une largeur de bande de 3 dB de 0,2 nm. De plus, la puissance de sortie moyenne d'environ 15mW est atteinte à la sortie de la graine.

Entre le laser d'amorçage et l'étage d'amplification de puissance, des préamplificateurs à deux étages sont utilisés. Au premier étage du préamplificateur, la sortie du laser d'amorçage est connectée au port signal du MLD et la même diode laser que le laser d'amorçage est connectée au port pompe du MLD. Un morceau de la même fibre MP dopée à l'Yb que celle utilisée dans la partie d'amorçage est connecté au port commun du MLD. L'extrémité de la fibre active est connectée au premier port du circulateur MP. Le deuxième port du circulateur est épissé au RBF MP chirpé et la terminaison de la fibre libre à l'extrémité du MP-RBFC est coupée en angle pour réduire les réflexions indésirables. Le MP-RBFC est écrit en utilisant un masque de phase chirpé de 0,145 nm/mm pour filtrer le spectre indésirable tel que les émissions spontanées d'amplification (ESA). Ce MP-RBFC a un pic de réflectance de 99,96%, centré à 1064nm avec une largeur de bande spectrale de 15,7nm. Enfin, le troisième port du circulateur est utilisé comme sortie du premier étage de préamplification.

Au deuxième étage du préamplificateur, la sortie du premier préamplificateur est connectée au port signal du MLD, et la même diode laser que celle des deux derniers étages est connectée au port pompe du MLD. Un morceau de la même fibre MP dopée à l'Yb que celle utilisée dans les deux dernières parties est connecté au port commun du MLD. L'extrémité de la fibre active est connectée à l'isolateur haute puissance et l'autre côté de l'isolateur est utilisé comme port de sortie pour cet étage. Le montage expérimental des premiers et deuxièmes étages de préamplification est présenté respectivement dans les figures 4.4 et 4.5.

Les résultats de ces deux étages d'amplification sont les suivants :

1- Augmentation de la puissance de sortie de la source d'amorçage à 20 et 130mW après la première et la deuxième étape d'amplification monomode respectivement.

2- La largeur de bande spectrale du laser est augmentée à 0,5nm et 1nm après chaque préamplification de premier et deuxième étage grâce à la auto-modulation de phase (AMP).

3- Filtrage du spectre indésirable tel que les émissions spontanées d'amplification (ESA).

La dernière étape d'amplification du système est l'amplificateur de puissance dont la configuration est illustrée à la figure 4.7. A ce stade, la sortie, provenant des préamplifications, est connectée au port signal du combineur, et deux pompes multimodes 10W-980nm sont épissées au port pompe du combineur pour amplifier la puissance moyenne du signal d'entrée de 130mW à plus de 10W après l'étape de post-amplification. La sortie du combineur est connectée à une fibre à large zone de mode dopée à l'Yb de 1,5 m (FPLZ 10/130), puis à une fibre passive à large zone de mode de 1,5 m (PFLZ 10/125). Comme la puissance de crête de l'impulsion dans le post-amplificateur est élevée, un AMP se produit, ce qui entraîne un élargissement de la bande passante à environ 20 nm. Ensuite, le stripper de la pompe est construit pour éliminer l'excès de puissance de la pompe. Enfin, la sortie est connectée à un collimateur pour collimater la lumière avec un diamètre de faisceau de 1,5mm.

L'étape suivante est celle du compresseur d'impulsions, qui est expliquée brièvement dans ce qui suit. La compression d'impulsions est une méthode efficace qui tire parti de la corrélation entre la largeur de l'impulsion et son spectre optique. Il est possible d'amplifier les impulsions au-delà des seuils de dommages conventionnels qui sont imposés par les composants optiques du système laser. Il est possible de réduire la largeur d'impulsion en appliquant une dispersion du côté opposé, également appelée dispersion négative, afin d'obtenir les impulsions les plus courtes après une propagation dispersive. Cela ramènerait les impulsions à leur plus petite longueur possible. Comme la plupart des matériaux dans la région spectrale de 1 µm présentent une dispersion positive, il est généralement nécessaire d'employer des méthodes alternatives pour appliquer une dispersion négative. Afin de satisfaire cet objectif, l'une des méthodes les plus fréquemment utilisées consiste à utiliser des paires de réseaux de diffraction. Par rapport à d'autres techniques permettant d'obtenir une dispersion négative, comme l'utilisation de prismes, les réseaux peuvent atteindre des niveaux de dispersion négative beaucoup plus élevés dans un espace plus réduit que ces autres techniques. La dispersion négative est obtenue par une paire de réseaux dans sa forme la plus fondamentale, car les différentes longueurs d'onde empruntent des chemins différents. Cela est dû au fait que les grandes longueurs d'onde ont une vitesse de propagation plus élevée. Par conséquent, les grandes longueurs d'onde doivent parcourir un chemin plus long que les petites longueurs d'onde pour comprimer l'impulsion. Lorsqu'une impulsion laser à large spectre est incidente sur un réseau de diffraction, les différentes longueurs d'onde qui composent l'impulsion se diffractent sur le réseau selon des angles qui dépendent de la longueur d'onde. Si la longueur d'onde de cette impulsion est "chirpée" de manière à ce que la fréquence augmente pendant la durée de l'impulsion, la diffraction étalera la lumière de manière proportionnelle, la première partie de l'impulsion (les plus grandes longueurs d'onde) se diffractant à un angle plus important. La partie arrière de l'impulsion (longueurs d'onde plus courtes) sera diffractée à un angle plus petit et sera dirigée vers le bord avant du second réseau. Lorsque la lumière diffracte à partir du deuxième réseau, qui est orienté parallèlement au premier réseau, les différentes parties de l'impulsion (avec leurs différentes longueurs d'onde correspondantes) se diffractent selon des angles qui produisent une impulsion dont les parties sont presque synchronisées dans le temps. La puissance de crête augmente considérablement, tandis que l'énergie totale reste pratiquement la même. Par conséquent, la largeur d'impulsion initiale de 10ps est comprimée à 200fs dans la section de compression d'impulsion. Comme la perte d'insertion de chaque réseau de transmission est d'environ 7 %, on s'attend à une perte totale d'environ 28 % en raison du quadruple passage du faisceau à travers les réseaux dans le compresseur et, par conséquent, la puissance de sortie moyenne chute de 10 W à 7 W (pour plus de détails, voir la figure 4.11).

Comme la mesure de la stabilité des impulsions optiques ultracourtes en temps réel est cruciale pour diverses applications telles que la microscopie de génération de seconde harmonique (GSH) à grand champ, le faisceau de sortie du laser a été collimaté pour mesurer les fluctuations de puissance d'une impulsion à l'autre de ce laser à fibre pulsé. Les fluctuations d'impulsion à impulsion ont été mesurées en utilisant la méthode fournie dans la référence [175, 176]. Comme l'énergie des impulsions est liée à leur puissance de crête, les événements indésirables et leurs caractéristiques associées peuvent être saisis par une mesure de l'énergie des impulsions d'un coup à l'autre. Dans nos essais, cette mesure a été réalisée à l'aide d'une photodiode et d'un oscilloscope analogique de 40 GSA/s. Cet appareil offre une mesure de l'énergie moyenne et de l'énergie de pointe. Cet appareil permet de mesurer l'énergie moyenne de chaque impulsion dans nos expériences. Cela permet de caractériser les fluctuations de la densité de puissance. Pour quantifier les oscillations de la densité spectrale de puissance, des histogrammes ont été tracés sur un million d'acquisitions d'impulsions avec la même amplitude de signal de la photodiode et le même niveau de déclenchement pour chaque mesure. Comme la détection linéaire a été utilisée, il n'y a pas eu d'effets de saturation. La proportion des fluctuations d'un coup à l'autre a été calculée à l'aide de l'équation 4.12. Grâce à cette partie, la stabilité IAI d'environ 2,4 et 3,4 pour cent est réalisée pour l'amorce et la sortie du laser à fibre à verrouillage de mode de 1064nm respectivement.

II. Microscopie optique non linéaire

Au cours des deux dernières décennies, la microscopie par génération de seconde harmonique (GSH) est devenue une méthode clé pour l'imagerie optique, avec de nombreuses applications dans les sciences des matériaux et biomédicales. Dans ce processus optique non linéaire, un matériau hautement polarisable avec une organisation structurelle non centrosymétrique est exposé à des impulsions laser ultrabrèves, ce qui entraîne la génération de photons à exactement la moitié de la longueur d'onde (deux fois la fréquence) de la lumière d'entrée [14]. Afin d'induire un GSH enregistrable, et plus généralement des processus optiques non linéaires, sans endommager l'échantillon, l'énergie laser doit être confinée dans une durée d'impulsion ultra courte (femtosecondes) [15]. En raison de cette exigence, les progrès réalisés dans le développement de technologies laser à verrouillage de mode ultrarapides fiables et robustes ont été essentiels pour l'amélioration des techniques de microscopie optique non linéaire [14, 16], en particulier pour l'imagerie biomédicale. Grâce à ces sources laser, des systèmes de microscopie clés en main ont été développés et sont désormais largement répandus dans les laboratoires de recherche.

La microscopie de fluorescence multiphotonique, en particulier la microscopie à excitation à deux photons (EF2P), présente de nombreuses similitudes avec la GSH, de sorte qu'elles peuvent être combinées sur le même instrument [17]. Les deux procédés à deux photons utilisent généralement des lasers ultrarapides proches de l'infrarouge (NIR, 700-1300 nm) pour l'excitation/génération, et des images tridimensionnelles (3D) sont obtenues avec une résolution inférieure au micron dans la direction latérale et au micron dans la direction axiale [18, 19]. Ces longueurs d'onde relativement longues assurent également une grande profondeur de pénétration dans les tissus (jusqu'à 1 mm) [20, 21]. En raison de la nature non linéaire de l'interaction lumière-matière en microscopie multiphotonique, la sélectivité du plan focal est obtenue sans l'utilisation de trous d'épingle ou d'autres optiques confocales utilisées en microscopie confocale [22]. En outre, la résolution spatiale est améliorée en raison de la non-linéarité des processus. Cette méthode simplifie considérablement la préparation des échantillons et permet même des études in vivo sur de petits animaux [23]. De plus, le confinement de l'interaction non linéaire limite la phototoxicité et le photoblanchiment [24]. Malgré de nombreuses similitudes au niveau de la microscopie, les modalités GSH et EF2P sont basées sur des processus fondamentalement différents : dans la GSH, la conversion de fréquence est réalisée à travers des états virtuels sans transfert net d'énergie au système, contrairement à la EF2P qui implique un transfert de population des états électroniques fondamentaux aux états électroniques excités.

Dans le contexte de la microscopie, EF2P et GSH présentent de nombreuses similitudes techniques qui permettent de les combiner facilement et efficacement sur le même instrument. Comme indiqué précédemment, la longueur d'onde du laser se situe traditionnellement dans la région NIR-I entre (700-1000 nm) [21] pour éviter l'absorption par les biomatériaux (eau, hémoglobine) [25], mais d'autres "fenêtres" optiques correspondant à ce critère sont disponibles. L'imagerie des tissus profonds est de la plus haute importance lorsqu'il s'agit d'échantillons biologiques. La profondeur d'imagerie dépend de la longueur d'onde d'excitation du laser [19, 26]. En utilisant des longueurs d'onde plus grandes, par exemple NIR-II (1000-1300nm), une pénétration plus profonde des tissus peut être atteinte puisque suffisamment de lumière peut atteindre le volume focal du tissu avec une diffusion minimale [19, 26]. Pour favoriser la génération efficace du signal optique non linéaire, la durée typique des impulsions est d'environ 100 femtosecondes à un taux de répétition de quelques dizaines de MHz [19].

L'imagerie GSH par balayage est une méthode bien établie et a été utilisée avec succès pour de nombreuses applications. Cependant, l'une des principales limites de cette mise en œuvre est son faible débit d'imagerie (photons détectés par image et par seconde), qui est également un facteur limitant l'utilisation de l'imagerie GSH sans marquage pour les processus biologiques très rapides [27]. Pour améliorer le débit d'imagerie, deux stratégies peuvent être envisagées : soit augmenter la vitesse de balayage, soit utiliser une microscopie sans balayage [28]. Pour cette dernière stratégie, la microscopie GSH à champ large (GSH-CL) est une technique dans laquelle toute la zone d'intérêt est éclairée simultanément et les signaux sont détectés sur une caméra [28]. Traditionnellement, la microscopie GSH-CL est réalisée à l'aide d'impulsions µJ et de lasers à fréquence de répétition moyenne (kHz). Il a été prouvé que la microscopie GSH-CL améliore le débit d'imagerie de 2 à 3 ordres de grandeur par rapport à la microscopie à balayage [28]. L'une des variantes de la microscopie GSH à champ large est la microscopie GSH holographique, mais elle a été limitée à l'étude des matériaux nanocristallins [29]. En raison de la délicatesse des échantillons de cellules vivantes, certaines précautions doivent être prises afin d'éviter tout photodommage. Plusieurs études ont étudié le seuil d'endommagement en microscopie GSH-CL pour différentes lignées cellulaires dont la principale conclusion est de maintenir l'énergie des impulsions et donc le dépôt de chaleur en dessous du seuil d'endommagement des échantillons [30]. Des progrès récents ont permis de concevoir un microscope GSH-CL à haute fréquence de répétition (MHz) pour l'imagerie en direct de tissus musculaires contractés, qui utilise des impulsions laser d'une énergie d'environ 60nJ par impulsion [30].

L'objectif principal du projet était de construire un laser à fibre pulsée unique en son genre à utiliser comme source de lumière d'excitation pour la microscopie GSH-CL. Ainsi, un microscope GSH construit sur mesure est conçu pour tester l'efficacité du laser. L'alignement du faisceau étant essentiel pour minimiser les pertes de signal en microscopie GSH, tous les composants optiques sont fixés sur la table à l'aide de supports pour améliorer l'efficacité et réduire la susceptibilité à un mauvais alignement. Le faisceau de sortie du laser est précisément aligné pour se propager à travers la plaque demi-onde et le polariseur, qui sont utilisés pour contrôler la quantité de puissance. La première lentille est utilisée pour focaliser le faisceau laser sur le cristal BBO lors de l'impact avec le faisceau d'excitation, le cristal BBO émet une lumière à fréquence doublée (532nm) dans les deux directions avant et arrière. De plus, la deuxième lentille est positionnée après le cristal pour corriger la divergence du faisceau afin que le détecteur du microscope collecte le maximum de lumière incidente. Pour les mesures GSH vers l'avant, le dispositif fonctionne en mode transmission, dans lequel la composante avant de la lumière GSH se propage dans la même direction que le faisceau laser. Le séparateur d'harmoniques filtrera la lumière laser de 1064nm, permettant au photodétecteur de détecter uniquement le signal GSH. En conséquence, le dispositif GSH produit 2,5 W de lumière verte (532 nm), soit une efficacité d'environ 40 %.

Le GSH efficace se produira dans la condition appelée correspondance de phase. Le BBO étant un cristal anisotrope, le changement de l'angle du cristal affectera les conditions d'adaptation de phase en modifiant les indices de réfraction dans le cristal. Dans cette activité, le cristal BBO est fixé solidement au centre du support rotatif. Le faisceau laser est ensuite collimaté pour se propager à travers le centre du cristal. Comme le processus GSH est sensible à la rupture de symétrie causée par une interface entre deux milieux, l'incidence du faisceau sur le bord du cristal augmenterait de manière significative l'intensité du GSH. Ceci implique que lorsque la lumière se réfracte dans un cristal BBO, elle se divise en deux rayons : le rayon ordinaire, qui suit la loi de Snell, et le rayon extraordinaire, qui ne la suit pas. Ces rayons sont polarisés linéairement et orthogonalement l'un par rapport à l'autre, le rayon ordinaire étant polarisé orthogonalement à l'axe optique, ce qui entraîne des vitesses de phase et des indices de réfraction différents pour les deux rayons.

En conclusion, en optique non linéaire, un faisceau optique focalisé sur un échantillon produit une réponse proportionnelle au faisceau d'excitation. Ce phénomène est applicable, par exemple, à la microscopie, où il sert d'outil de base pour l'analyse des métamatériaux optiques et des échantillons biologiques. Par rapport aux techniques de microscopie optique linéaire, les avantages des techniques non linéaires sont une pénétration plus profonde des tissus et un contraste plus important. La GSH est à la base de l'une des techniques de microscopie non linéaire les plus populaires. La longueur d'onde du signal en GSH est égale à la moitié de la longueur d'onde du champ d'excitation initial. Les microscopies GSH peuvent être utilisées, par exemple, pour étudier les effets de surface des nanoparticules et les processus des systèmes biologiques.

Comme la vitesse d'acquisition des images en microscopie est limitée par la vitesse de balayage du laser, dans la microscopie GSH à grand champ, qui est une sorte de microscopie GSH, toute la zone d'intérêt est éclairée simultanément et les signaux sont détectés par une caméra. Cette dernière stratégie permet une imagerie rapide de grandes zones, mais elle nécessite de courtes impulsions laser à haute énergie. En raison de la sensibilité des échantillons de cellules vivantes, des précautions particulières doivent être prises pour éviter les photodommages. Pour une pénétration plus profonde des tissus, des longueurs d'onde plus longues, de l'ordre de 1000 à 1300 nm, sont utilisées pour minimiser la diffusion.

L'un des principaux éléments du dispositif de microscopie non linéaire est le laser pulsé qui sert de source de lumière d'excitation. En outre, le laser nécessite un environnement stable et une grande stabilité IAI pour fonctionner efficacement, ce que j'ai présenté dans cette thèse.

L'étude fournie dans cette thèse s'inscrit dans deux catégories de recherche principales. Premièrement, présenter un examen complet du laser à fibre à maintien de polarisation à mode passif fonctionnant dans la région de longueur d'onde de 1μm. Par conséquent, nous avons prouvé les caractéristiques d'impulsion d'un laser basé sur MSESA avec une cavité linéaire. Des techniques standard de caractérisation des impulsions ultracourtes ont été employées pour diagnostiquer les comportements du laser. Le spectre optique et le spectre RF ont également été examinés. Les schémas laser proposés dans cette étude utilisaient une fibre active dopée à l'Yb comme milieu de gain et fonctionnaient dans tous les régimes de dispersion normale. Des expériences ont été menées sur le laser MSESA à cavité linéaire proposé dans une région à verrouillage de mode avec une puissance de sortie moyenne de 7W. Sur l'oscilloscope, le taux de répétition fondamental a été observé à 42MHz, ce qui correspond à une longueur de cavité d'environ 2,5m. Après compression, la largeur d'impulsion de 200fs a été mesurée à l'aide d'un autocorrélateur. En conséquence, la puissance de crête et l'énergie de l'impulsion étaient respectivement de 798 kW et 166nJ. En outre, la stabilité P2P de la graine et de la sortie du laser à fibre optique 1064nm à verrouillage de mode était d'environ 2,4% et 3,4%, respectivement. Dans la deuxième section de cette thèse, des études de microscopie non linéaire ont été rapportées comme une application de ce laser.

Comme j'ai couvert la majorité de la caractérisation et des mesures de ces lasers à fibre pulsés dans cette étude, je suis convaincu que les observations présentées dans cette thèse apporteront plus de bénéfices aux chercheurs dans le domaine des lasers à fibre.

TABLE OF CONTENTS

LIST OF FIGURES

LIST OF ABBREVIATIONS AND SYMBOLS

Abbreviations

AOPDF	Acousto-optic programmable dispersion filters
APM	Additive pulse mode-locking
ANDi	All normal dispersion
ASE	Amplification spontaneous emissions
CARS	Coherent anti- stokes Raman scattering
CCD	Charge coupled device
CFBG	Chirped fiber Bragg grating
CPA	Chirped pulse amplification
CW	Continuous wave
DCF	Dispersion compensating fiber
DBR	Distributed Bragg reflector
EM	Electromagnetic
ECM	Extra cellular matrix
FBG	Fiber Bragg grating
FWM	Four wave mixing
FTSI	Fourier transform spectral interferometry
FROG	Frequency resolved optical gating
FWHM	Full width half maximum
GDD	Group delay dispersion
GVD	Group velocity dispersion
KLM	Kerr-lens mode locking
LMA	Large-mode-area
ML	Mode locking
MM	Multi-mode
NALM	Non-linear amplifying loop mirror
NOLM	Non-linear optical loop mirror
NLOM	Nonlinear optical microscopy
NLO	Nonlinear optics
NPE	Non-linear polarization evolution
NA	Numerical aperture
OCT	Optical coherence tomography
OSA	Optical spectrum analyzer
PLMA	Passive-large-mode-area
PM	Polarization maintaining
P2P	Pulse-to-pulse
QWs	Quantum wells
RF	Radio frequency
RI	Refractive index
SHG	Second harmonic generation
SPM	Self-phase modulations
SESAMs	Semiconductor saturable absorber mirrors
SNR	Signal-to-noise ratio
SM	Single mode
SPEF	Single-photon excited fluorescence

SPIDER	Spectral phase interferometry for direct electric field reconstruction
SFG	Sum frequency generation
THG	Third harmonic generation
TOD	Third order dispersion
3D	Three-dimension
TIR	Total internal reflection
2D	Two-dimension
TPEF	Two-photon excited fluorescence
TPE	Two-photon fluorescence excitation
WDMs	Wavelength division multiplexers
WF-SHG	Wide-field SHG microscopy
YDFAs	Ytterbium-doped fiber amplifiers
YDFL	Ytterbium-doped fiber laser

Chemicals

BBO	Beta barium borate (crystal)
LBO	Lithium triborate (crystal)
YB	Ytterbium
ER	Erbium

Units

m	Meter
mm	Millimeter (10^{-3}Meter)
µm	Micrometer (10^{-6}Meter)
nm	Nanometer (10^{-9}Meter)
J	Joule
mJ	Millijoule (10^{-3}Joule)
µJ	Microjoule (10^{-6}Joule)
nj	Nanojoule (10^{-9}Joule)
kHz	Kilohertz (10^{3} Hertz)
MHz	Megahertz (10^{6} Hertz)
s	Second
ns	Nanosecond (10^{-9}Second)
ps	Picosecond (10^{-12} Second)
fs	Femtosecond (10^{-15}Second)
as	Attosecond (10^{-18}Second)
W	Watt
mW	Milliwatt (10^{-3} Watt)
C	Centigrade
$\frac{J}{cm^2}$	Joule per centimeter square
µJ/cm²	Micro joule per centimeter square

nm/mm	Nanometer per millimeter
%	Percent
dB	Decibel
ps/nm/km	Picosecond per nanometer per kilometer
W/cm^2	Watt per centimeter square

Notations

I(t)	Pulse intensity
Φ (t)	Phase
S(ω)	Spectrum
φ(ω)	Spectral phase
$E_{unk}(\omega)$	Unknown phasor in frequency domain
$E_{ref}(\omega)$	Reference phasor in frequency domain
τ	Time
E	Electric field
ω	Angular frequency
λ	Wavelength
n	Refractive index
c	Speed of light
ϕ_c	Critical angel
ϕ_a	Incident angel
α	Core radius
B_m	Modal birefringence
Λ	Grating period
ΔF	Mode separation
L	Length
x	Polarization unit vector
v_g	Group velocity
D	Dispersion parameter
ε_0	Vacuum permittivity
χ (j) (j=1, 2…)	Jth order susceptibility
P	Instantaneous power
Aeff	Effective mode area
$\Delta\tau_p$	Pulse width
$\Delta\omega_s$	Spectral band width
I_{max}	Peak intensity

α_c	Regular cavity losses
α_m	Additional loss of the modulator
f	Frequency of laser
τ_{out}	Primary pulse width
τ_{in}	Final pulse width
θ_i	Angle of incidence
d	Grating line density
φ_2	Amount of dispersion
N	Number of passes
m	Diffraction order
θ_L	Littrow angle
θ_D	Angle of diffraction
P_{peak}	Peak power
P_{avg}	Average output power
$\mathrm{F}_{\mathrm{sat}}$	Saturation fluence
ΔR	Modulation depth
z	Vertical location in the epitaxial layer stack
F	Pulse fluence
d	Focused beam spot diameter
$\vec{P}$	Polarization of the medium
ψ	Complex amplitude of the incident beam
Δk	Phase mismatch between the excitation and the emitted light

Chapter 1: Introduction

1.1 History of laser

Albert Einstein introduced stimulated emission, a physical amplification phenomenon, in 1916, over 42 years before the fabrication of the first laser [31]. An incident optical signal of the appropriate frequency causes an excited electron to lose energy and return to a lower level, resulting in the emission of radiation. The first indirect evidence of stimulated emission was published by *Rudolf Ladenburg* in 1928 [32]. In 1953, *Charles H. Townes* and *James. P Gorden* built the first ever maser (microwave amplification by stimulated emission of radiation) [33]. This device's launch sparked the notion of extending this technique to higher frequencies. Thus began the race to construct the first laser [34]. *H. Maiman* constructed the first laser (ruby crystal medium) in 1960 [35], and this technology has been vital for studying a wide range of nonlinear optical processes, such as second harmonic generation (first observed by *Franken et al.* in 1961) [36]. Second harmonic generation (SHG) is currently employed in a wide range of applications, especially laser scanning microscopy for material and biomedical imaging [21].

There are numerous applications (particularly nonlinear effects) that rely on peak power, hence validating the need for pulsed lasers. Q-switching (also known as giant pulse formation) lasers were one of the initial steps toward the development of lasers with high peak power. This concept was first presented in 1958 by *Gordon Gould* [34], and then independently in 1962, *Fred J. McClung* and *Robert W. Hellwarth* achieved 100 times more peak power than conventional ruby lasers using the Kerrcell switching method. A typical Q-switching laser may generate light pulses of 10 to 20 ns duration [37].

Mode locking is another effective technique for generating pulsed lasers. In this approach, optical pulses can be as short as the Fourier transform of the bandwidth [16], and the path to ultrafast pulse generation has been accelerated by the broad spectral bandwidth of dye lasers. In 1972, *Erich Ippen* and *Charles Shank* reported that passive mode locking continuous wave (CW) dye lasers could generate 1.5 ps pulses [38].

Dye lasers had many limits, and maintenance of dye solutions was particularly difficult and complicated. This problem prompted the development of solid-state lasers. In 1987, it was reported that pulses as short as 6 fs could be produced by combining the effects of pulse broadening and dispersion compensation. However, generating pulses below 100 fs was very difficult [39]. The introduction of Ti-Sapphire lasers (1982, CW) coupled passive Kerr lens mode-locking (1990) revolutionized the ultrafast field by producing pulses as short as 60 fs by circulation within the oscillator cavity [40]. In other words, Kerr lens mode locking paved the way for femtosecond pulses with high peak power to be generated straight from the laser cavity.

In laser technology, the introduction of chirped pulse amplification (CPA) was a key accomplishment (Figure 1.1) [41]. This method eliminated the restriction on pulse amplification induced by the nonlinear phenomena known as self-focusing [42]. The combination of a mode-locking Ti-Sapphire laser and a CPA produces a high-power pulse. With the aid of gas-filled hollow core fibers [43], a Ti-Sapphire laser system has generated powerful single-cycle pulses [44]. This method is commonly employed in ultrafast laboratories for applications in strong-field physics [45].

Besides that, *Diabolize et al.* [46] introduced the concept of pulsed fiber laser in 1983. Considering the short and ultrashort pulse regions (pulses of a few picoseconds or less), the use of fiber lasers for pulse creation was the next most difficult challenge that researchers had to accomplish. This was since light confinement within a restricted volume influenced the scalability of the fiber lasers' output power since it typically results in various nonlinear features. Utilizing highly doped active fiber lasers and chirped pulse amplification, ultrafast fiber lasers with high power were created in 1990 [47].

Pulsed fiber lasers are utilized in a variety of industries, including optical communication, medical imaging [48], spectroscopy [49], pulsed laser deposition, precision metrology, and micro matching [50], and many others. As potential and powerful laser sources, fiber lasers influence the advancement of laser applications. High-performance and high-functional fiber lasers have advantageous properties which make them indispensable in a variety of practical applications. Technological advancements have accelerated the development of new laser technologies, and efficient inventions are in high demand.

Due to its diverse characteristics, fiber laser is regarded as one of the most promising laser types currently available. Because of their capacity to generate diverse wavelengths, fiber lasers are widely used in industrial applications. Fiber lasers are highly versatile; thus, they can be utilized in a variety of settings, including industrial, communications, and medical. In addition to all the qualities listed above, fiber lasers are excellent due to their small size, lengthy lifespan, capacity to offer high power output, great dependability, and flawless beam quality [51].

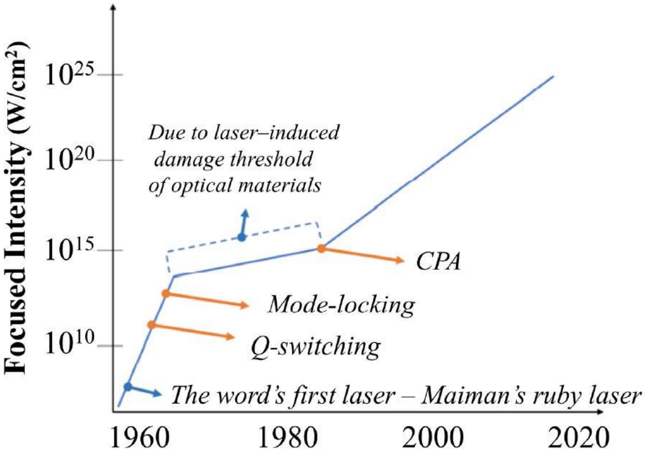

Fig. 1.1: History of laser intensity [52].

1.2 Ultrashort pulses and applications

Electromagnetic radiation pulses with a very short amount are known as ultrashort pulses. A typical ultrashort pulse is 10 to 100 fs (1 fs = 10^{-15} seconds) in temporal width. The shortest ultrashort pulses are several attoseconds (1 as = 10^{-18} seconds) long, and the longest can be up to a few picoseconds (1 ps = 10^{-12} seconds). Owing to their short temporal extent, these pulses, must necessarily have large spectral bandwidths. This is easily understood using the Fourier transform relation between the time and frequency domains: the creation of a short pulse in time needs the coherent superposition of a wide range of frequencies. This bandwidth also depends on the pulse envelope's carrier frequency. For a given pulse width, the necessary bandwidth reduces as the carrier frequency increases.

Due to the short durations of these pulses, it is possible to reach high peak intensities ($\sim 10^{12}$ W/cm^2) with very low average powers and research phenomena that occur over small period scales. As a result of their high peak intensities, these pulses have several attractive applications. An example of such an application is micromachining [53, 54].

The time scale on which femtosecond pulses can ablate material is so short that only a small quantity of energy is lost as heat [55, 56]. This helps overcome the challenges provided by thermally produced stress, which leads to the formation of fractures and fissures and plagues nearly every other machining technique. In coherent control experiments, where the course of a chemical process can be altered by illuminating shaped ultrashort pulses on the reactants, ultrashort pulses are also utilized [57-60]. This permits the directed cleavage of chemical bonds in molecules, so regulating the outcome of a chemical reaction [61]. Recent developments in medical imaging have included multi-photon imaging [62, 63], CARS (Coherent Anti-Stokes Raman Scattering) microscopy [64], and OCT (Optical Coherence Tomography) [65-67]. Multi-photon microscopy involves the detection of second or third harmonic signals created within bio tissue by longer-wavelength-centered pulses. This enables greater tissue probing depths and improved imaging resolution. The signal is created exclusively at the beam's focal point, and the extended wavelengths of the probe scatter less in the tissue, allowing for deeper focused spot placement. The focal point scans the entire tissue volume, and the resulting higher harmonic photons scatter in the tissue and emerge at the surface of the sample, where they may be identified, enabling the creation of a multilayer topographical map of the biological sample. Another possible application is ultrafast communications and optical switches [68], which are being widely researched.

Additionally, attosecond pulses and soft x-rays are produced using ultrashort pulses [69], which have aided to investigate quicker time-scale physical events and to develop and research exotic nonlinear optical effects including optical beam filamentation [70, 71].

There are many more applications of ultrashort pulses that are not listed here. Ultrashort laser pulses continue to play an important role in the development of various technologies, and they also provide an excellent tool for studying the physics of processes occurring on extremely short time scales. For most desired applications, the study and development of pulse measurement techniques and ways to change pulse properties, such as pulse compression, pulse shaping, and dispersion control, are essential.

1.3 Generation of ultrashort pulses

Based on their mode of operation, laser sources can be divided into two categories: pulsed lasers and continuous wave (CW) emitting lasers. In principle, these lasers can be achieved in a variety of systems, including gas lasers (He-Ne or CO2), semiconductor lasers (Nd:YAG, Ti:Sapphire), and dye lasers (including Rhodamine or Malachite green solutions). CW lasers have spectral widths that are relatively narrow. Using a fast shutter at the output of a CW-laser, e.g., by inserting a Pockels cell and a linear polarizer in the cavity, it is possible to generate laser pulses with temporal widths as low as 10 nanoseconds to 100 nanoseconds. As the correct voltage is put across a Pockels cell, it functions as a waveplate, and when light passes through it, its polarization changes from 's' to 'p,' and it is then rejected by the linear polarizer. This technique is known as "active switching," and its speed is constrained by the maximum speeds that can be achieved with electronic switching.

Utilizing a saturable absorber in a cavity is an alternative method for producing pulses. This allows for faster switching rates, and the resulting pulses are between 500 femtoseconds and a few picoseconds in duration. Typically, a dye is employed as the saturable absorber, which absorbs low-intensity light but turns transparent at a particular saturation threshold. Therefore, the leading and trailing edges of a pulse in the cavity suffer absorptive losses and are repressed, while the high intensity zone near the pulse's core acquires strength. This procedure shortens the pulse and heightens the peak intensity. This switching method is known as passive switching or passive mode locking [72, 73].

Laser gain medium in recent lasers is Ti:Sapphire. This technology can generate pulses with durations ranging from a few femtoseconds or a few optical cycles to many picoseconds [73]. In these lasers, the crystal is optically pumped by a solid-state diode laser, and the laser cavity may emit light over a broad range of wavelengths, from 650nm to 1100nm. The material emits in a continuous-wave (CW) mode, but the cavity can be optimized to emit in a pulse mode. In the cavity, the CW and pulsed beams competed for the gain medium's energy. To produce mode locking or to generate pulses, the Kerr-lensing phenomena is employed [74]. In Kerr lensing, high-energy laser beams self-focus while passing through a material due to the optical Kerr effect's nonlinear refractive index shift. The induced refractive index changes across the cross-section of a Gaussian beam and is greater in the beam's center than its edges. Due to thermal lensing (caused by the pump), the crystal works as a waveguide for both beams, but for the pulsed beam, the beam width is further decreased due to Kerr-lensing. This leads to a smaller beam spot than that of the CW beam on the flat mirrors at the cavity's ends. In previous systems, an aperture was added in front of the ending mirrors to cut-off the continuous-wave (CW) beam and favor the pulsed beam operation. In later systems, however, a soft aperture is employed, in which the pump beam is focused to a narrow beam width in the crystal by means of a telescope in the cavity; this increases the overlap of the pump with the smaller pulsed beam, which consequently experiences a significantly greater gain than the CW beam.

1.4 Ultrashort pulse measurement

There are a variety of ultrashort pulse measurement techniques available. Precise measurement of the ultrashort pulses' temporal profile necessitates complete knowledge of the pulse intensity, I(t), and phase Φ (t). The measurement of intensity and phase is not straightforward, and the methods that can be utilized are mentioned below. Pulse measurement can be performed in the spectral domain, i.e., by measuring the spectrum S(ω) and the spectral phase φ(ω), because Fourier transforms uniquely relate the field in the frequency domain to the field in the time domain. Pulse measuring techniques, such as spectral interferometry and its variants, are linear, meaning they do not utilize nonlinear interactions to generate signals. Interferometric methods are advantageous due to their great sensitivity, which enables the measurement of very weak pulses (10^{-21}joules or zeptojoules per pulse) and complex pulses. Spectral interferometry usually necessitates a pre-defined reference pulse, which poses a challenge for certain applications. Since self-referential approaches rely on nonlinear interactions to generate the signal, they require large pulse energies. FROG (frequency resolved optical gating), which is a temporal frequency domain measurement, and SPIDER (spectral phase interferometry for direct electric field reconstruction) are two fundamental examples of such approaches.

1.5 Pulse measurement using interferometry

The spectral phase of an ultrashort pulse is determined by mixing it interferometrically with a reference pulse in a spectrometer. In spectral interferometry, the reference beam and the unknown beam are collinear and transmitted to a spectrometer. With adequate resolution, the spectrometer records the spectral fringes caused by the interference of the reference and the unknown. The fringe spacing of the recorded spectrum includes phase-difference information as illustrated in the following two equations, where $E_{unk}(\omega)$ and $E_{ref}(\omega)$ are the phasors representing the unknown and reference complex fields in frequency domain, respectively, and are delayed by time τ.

$$\mathbf{S}(\boldsymbol{\omega}) = \left| |\boldsymbol{E}_{\boldsymbol{unk}}(\boldsymbol{\omega})| e^{i\varphi_{unk}(\omega)} + |\boldsymbol{E}_{\boldsymbol{ref}}(\boldsymbol{\omega})| e^{i\varphi_{ref}(\omega)} e^{-i\omega\tau} \right|^{2} \qquad \textbf{Eq (1.1)}$$

The oscillating term has the phase Δφ(ω) which is given by:

$$\Delta\phi(\omega)= \boldsymbol{\varphi_{unk}}\ (\omega) - \boldsymbol{\varphi_{ref}}\ (\omega) + \boldsymbol{\omega\tau} \qquad \textbf{Eq (1.2)}$$

There are several techniques available for extracting the phase difference from the interferogram's measured spectrum. The algorithm for Fourier transform spectral interferometry (FTSI) is the most common method employed [75], in which the measured spectrum is Fourier transformed to the time domain [76]. The resulting Fourier transform has a peak representing the background intensity and two side bands representing the cross term and its complex conjugate. Any of the side bands may be trimmed, zero-shifted, and Fourier converted back to the frequency domain. After separating the reference spectrum, it is possible to acquire both the spectrum and spectral phase relative to the reference pulse.

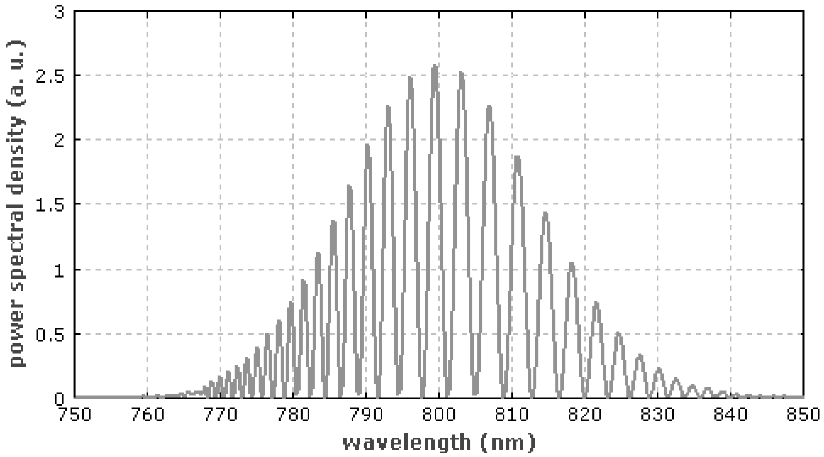

Fig. 1.2: Shows the spectrum of two 50 fs femtoseconds pulses delayed by 500fs [77].

In SI, the alignment is problematic since the two beams must be collinear. In addition, this method filters in the time domain, which prohibits us from exploiting the spectrometer's full spectrum resolution. However, there are variants of SI that circumvent these problems. Crossed beam spectral interferometry employs a two-dimensional CCD (Charge coupled device) array and captures the spatial fringes created by crossing two big beams spatially in the dimension orthogonal to the spectrometer's wavelength axis [78]. For the spatial fringes to be seen, the pulses must have zero delay. It exploits the full spectral resolution of the spectrometer by filtering the signal in k-space and utilizing the second dimension of the camera, as shown in figure 1.2.

1.6 Dispersion control of Ultrashort pulses

In general, ultrashort pulses have broad bandwidths, and because various colors travel at different speeds in a dispersive medium, ultrashort pulses tend to disperse over time. Stretching a pulse causes its peak intensity to diminish, which is undesirable in several applications. In this part, we discuss dispersion control (or pulse compression) techniques and their underlying operational principles. The electric field of an ultrashort pulse can be characterized completely in time by describing its intensity, I(t), and phase, ϕ (t), as functions of time.

$$\boldsymbol{E(t) = \sqrt{I(t)}\ \exp\{-i\phi(t)\}} \qquad \textbf{Eq (1.3)}$$

This corresponds to the pulse electric field in the frequency domain, as represented by the spectrum.
S (ω – ω$_0$), and the spectral phase φ (ω – ω$_0$), where ω$_0$ is the carrier frequency.

$$\boldsymbol{\tilde{E}\ (\omega - \omega_0) = \sqrt{S\ (\omega - \omega_0)}\ \exp\ \{-i\phi\ (\omega - \omega_0)\}} \qquad \textbf{Eq (1.4)}$$

When the spectral phase is constant across all frequencies, the shortest pulse width allowable by the Fourier transform relation for a given spectral bandwidth is achieved. A spectral phase which is not zero causes the pulse to spread in time. A Taylor series expansion of the spectral phase about the center frequency provides the primary pulse width control terms [79].

$$\boldsymbol{\varphi\ (\omega - \omega_0) = \varphi_0 + \varphi_1(\omega - \omega_0) + \frac{\varphi_2}{2!}(\omega - \omega_0)^2 + \frac{\varphi_3}{3!}(\omega - \omega_0)^3 + \frac{\varphi_4}{4!}(\omega - \omega_0)^4 + \ldots} \qquad \textbf{Eq (1.5)}$$

The coefficient of the linear term in the above expression is the group delay, which is the arrival time of the colors. The physical meaning of the quadratic term or quadratic spectral phase is that the delay varies linearly with frequency, which is also known as the linear chirp. Group delay dispersion (GDD) is represented by the factor of the quadratic term. GDD is positive over all dispersive materials at normal conditions. To nullify the effect, negative GDD must be supplied in some methods. Dispersion compensating fibers (DCF) can contribute negative GDD in fiber optics (figure1.3).

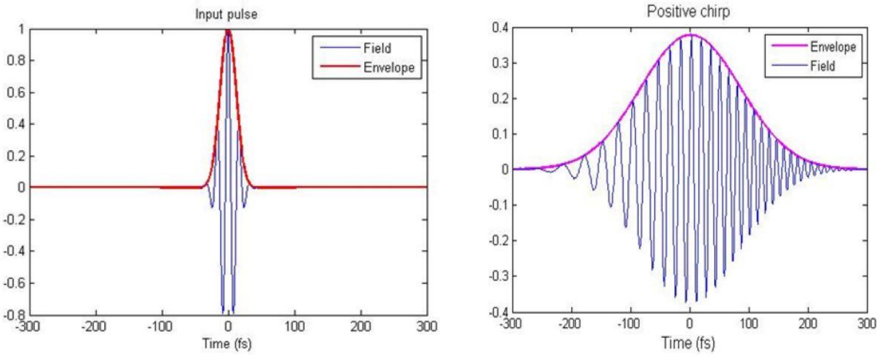

Fig. 1.3: An example which illustrates that the pulse width increases because of the quadratic phase or linear chirp. As duration increases, the peak intensity decreases [80].

The third order phase term relates to the third order dispersion (TOD) and influences the pulses in addition to stretching them. Because of this condition, the red and blue colors arrive either before or after the green color. These colors beat together to produce ringing of the intensity envelope of the pulse closer to the pulse's edges (figure 1.4). The sign of the TOD determines whether the ringing occurs on the pulse's leading edge or following edge. A pulse compressor must add negative TOD to compensate for the positive TOD introduced by materials.

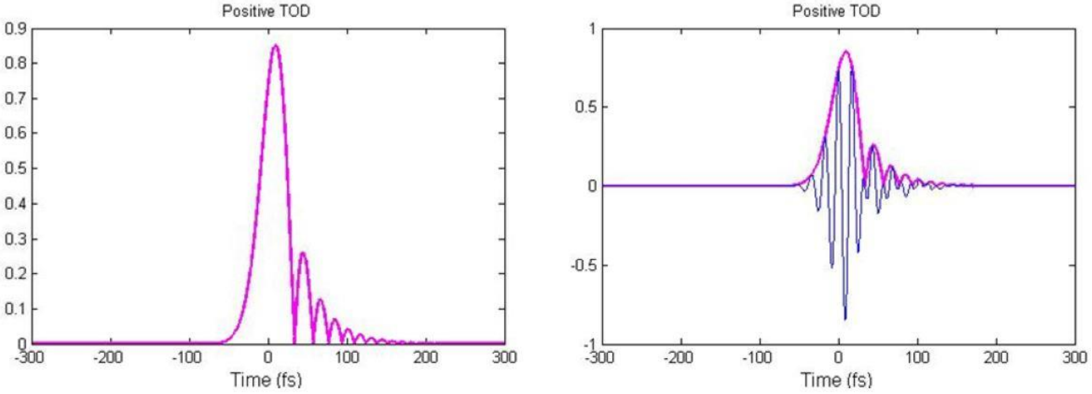

Fig. 1.4: An example of TOD causes ringing in the pulse envelope [80].

In the presence of spatiotemporal couplings such as spatial chirp, pulse front tilt, and angular dispersion, the spectral bandwidth and spectral phase can also change over the cross section of the beam. Because the spectral bandwidth at any position is less than the total spectral bandwidth of the beam, the shortest pulse width cannot be obtained at all positions across the beam in these circumstances. In addition, the beam cannot be focused to its diffraction-limited point in the presence of spatiotemporal couplings for the given beam size and lens characteristics [79]. In numerous applications, the spatial coherence of the laser beam is important. The spatial mode quality of a beam is defined by the beam width and the spatial-frequency bandwidth [81]. In a similar fashion, the complexity of the pulse in the time domain is determined by the time-bandwidth product, which is the combination of the temporal pulse width and the spectral bandwidth. High values of either the space bandwidth product or the time bandwidth product indicate a complicated pulse and poor beam quality. The following equations provide a thorough mathematical description of the pulsed electric fields in space and which time is frequently required:

$$E\,(x, y, z, t) = \sqrt{I(x,y,z,t)}\ \exp\{-i\phi\,(x,y,z,t)\} \qquad \textbf{Eq (1.6)}$$

$$\tilde{E}\,(x, y, z, \omega - \omega_0) = \sqrt{S(x,y,z,\omega - \omega_0)}\ \exp\{-i\phi\,(x,y,z,\omega - \omega_0)\} \qquad \textbf{Eq (1.7)}$$

1.7 Nonlinear methods for pulse compression

Several nonlinear techniques are used to compress pulses by utilizing nonlinear interactions. These methods, however, go outside the scope of the work described in this thesis, but the topic of nonlinear pulse compression needs a brief review for the sake of a comprehensive discussion on pulse compression. This section provides an overview of several nonlinear pulse compression methods.

Electro-optic phase modulators may apply an arbitrary spectral phase to the pulse to generate shaped pulses or a quadratic phase to compress or stretch a pulse [82]. Acousto-optic programmable dispersion filters (AOPDF) can be used for pulse stretching and compression as well as pulse shaping [83]. It has been reported that pulse compression utilizing tapered photonic crystal fibers can generate pulses as short as 20fs [84, 85]. Additionally, filamentation of the beam can lead to pulse compression [86]. Due to the space-time duality of Maxwell's equations, it is feasible to conduct temporal imaging like spatial imaging. Time domain magnification or demagnification is equivalent to pulse stretching and compression. Parametric time lensing is a technique that employs a four-wave mixing process to add a quadratic temporal phase to a pulse and has been proven for pulse measurement and dispersion compensation [87]. Also pulse compression using a pair of diffraction gratings, which we used as a compressor part for this work, and pulse compression using chirped mirrors are another two ways for pulse compression.

Chapter 2: Optical fiber and fiber components

2.1 Optical fiber

Optical fibers are the most fundamental component of fiber optics. They are used to transfer light over hundreds of kilometers. Even though optical fibers are made by glass (silica), they are not fragile, and it is feasible to bend them substantially even around the fingers, without breaking. Silica is the standard glass type for optical fibers due to its outstanding characteristics, low propagation losses, and high mechanical flexibility under pulling and bending [88]. Core, Cladding, Buffer, and Jacket are the four basic structural components of an optical fiber. Figure 2.1 provides a visual description of the location of each of these components within the optical fiber system. The core, with a typical diameter of 5-10μm is covered by another layer known as cladding (typically with a diameter of 125μm), which has a lower refractive index than the core. Cladding is crucial for preventing transmission losses from the core to outer space. The buffer layer encircles the cladding layer to protect the optical fiber from more damage and to prevent scattering losses. Jacket refers to the most outer layer of the fiber, which serves to identify and classify the various fiber kinds [89].

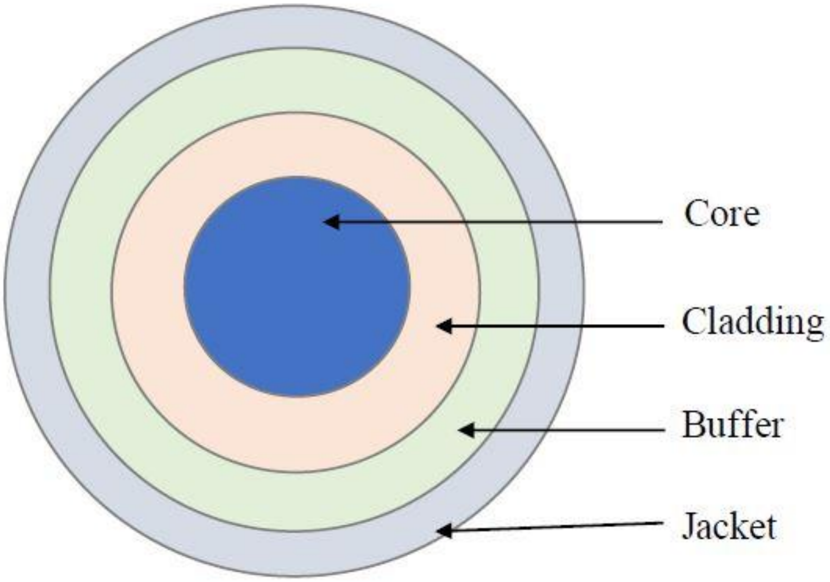

Fig. 2.1: Structure of the optical fiber [89].

The optical fiber's operating principle is related to the total internal reflection (TIR) at the core-cladding boundary [90]. When a light ray from a medium having a higher refractive index (n_1) approaches a medium with a lower refractive index (n_2), this phenomenon occurs at the interface between two transparent media. Nevertheless, this only occurs if the incidence angle (θ_1) exceeds the critical angle (θ_c) as illustrated in figure 2.2, where the overall TIR concept and related light confinement within the optical fiber are depicted.

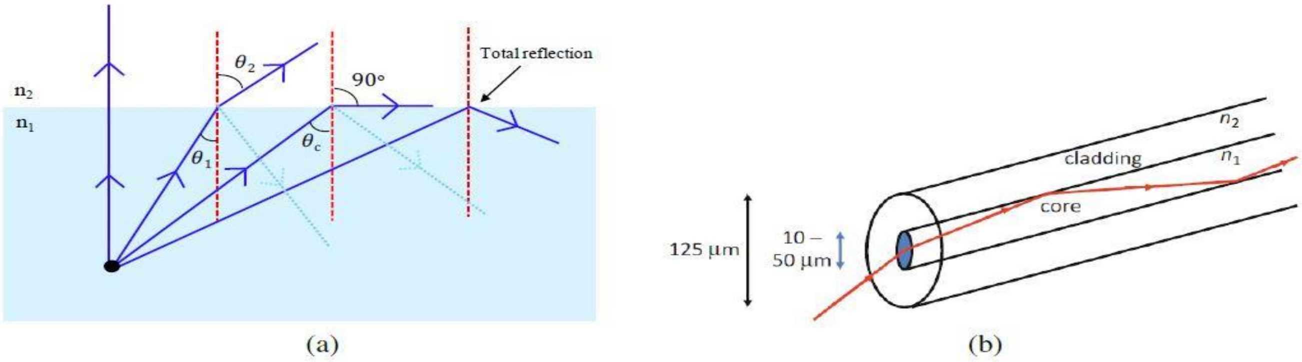

Fig. 2.2: (a) total internal reflection and (b) ray confinement within an optical fiber [91].

Optical fibers can be classified based on criteria such as the profile of the fiber's refractive index, the material used to produce the fiber, and the number of light propagation modes within the fiber. Active and passive fibers are two other classifications. Based on the refractive index profile, optical fibers are categorized as step-index fibers and graded-index fibers. Optical fibers are made from both plastic and glass, depending on the materials used. According to the mode of light transmission within the fiber, single-mode and multimode fibers are distinguished. In the next sections, detailed descriptions of several types of fibers are provided.

Total internal reflection controls the propagation of electromagnetic (EM) waves in an optical fiber between core-cladding boundaries. Snell's Law can be applied to calculate the necessary circumstances for total internal reflection. Once one ray enters to the optical fiber, it will be able to propagate along the core if the angle of incidence at the core-cladding boundary is greater than the critical angle. Rays which do not satisfy equation (2.1) will therefore leak out completely after multi-incident reflections at core-cladding boundaries.

$$\boldsymbol{\phi_c = \sin^{-1}(\frac{n_2}{n_1})} \qquad \textbf{Eq (2.1)}$$

The angle of incidence at the front facet of the fiber governs the coupling of light into the fiber. The permitted incidence angles for total internal reflection can be stated as a function of the core and cladding refractive indices.

$$\boldsymbol{\phi_a = \sin^{-1}\sqrt{n_1^2 - n_2^2} = \sin^{-1} NA} \qquad \textbf{Eq (2.2)}$$

The numerical aperture (NA) of a fiber is a crucial characteristic to consider since it affects the maximum optical coupling into the fiber. Consequently, a high NA fiber permits a greater amount of light to be efficiently coupled into the fiber.

2.1.1 Active fibers

The optical fiber core can be made active and used for amplifying in ultrafast lasers by doping it with laser-active elements [92]. Rare-earth doped fibers were first discovered in the 1960s, and the discovery allowed for the creation of new lasers with perfect beam quality. Particularly in telecommunication, non-linear microscopy, and material processing, active fiber-based applications are gaining popularity [93]. Rare-earth elements including ytterbium (Yb), erbium (Eb), and thulium make up the dopant ions. By connecting to glasses and crystals with higher absorption and emission efficiency, those elements' electron structures allow for the creation of triply ionized atoms [94]. As a result, fibers become active when doped with these materials. The most intriguing feature of these specialty fibers is their ability to absorb pumped photons, which are normally shorter wavelengths, and excite electrons into metastable states, which helps to increase light intensity by stimulating emission [95].

Ytterbium is a member of the periodic table's group of rare-earth elements which currently is one of the most widely utilized materials in silica fibers, providing a gain in the 1μm wavelength region [88]. Recent advancements have heightened interest in these fibers due to their ability to amplify signals between 975nm and 1200nm. As shown in figure 2.3(a), only sublevels of the ground-state manifold ($F_{7/2}$) and excited-state manifold ($F_{5/2}$) are relevant for all optical wavelengths.

In addition, As shown in figure 2.3(b), the usual absorption spectrum ranges from 900 nm to 1000 nm, with the peak absorption occurring at 975 nm. Compared to other rare-earth ions, the spectroscopy of Yb^{+3} is simple to understand [96]. Ytterbium-doped fiber amplifiers (YDFAs) sidestep numerous problems of other rare-earth-doped fibers by giving better output energy and power conversion efficiency, in addition to a broad absorption spectrum [97]. For the work described in this thesis, the operational wavelengths for the lasers and amplifiers are1064 nm, limiting the options for pump wavelengths for direct diode pumping. I've employed 975 nm pumping since it permits significant absorption and modifies the lowest possible device length, which is essential in high peak power applications to minimize nonlinear effects. Nevertheless, pumping at this wavelength reflects a three-level behavior, and only a 50% population inversion can be produced using this approach. In addition, because the absorption bandwidth is rather narrow, the amplifier output will be sensitive to any spectral shift of the pump resulting from fluctuations in diode temperature and/or injection current. Up to 97% upper state population can be achieved with 915 nm pumping because the active medium behaves like a quasi-four-level system [99].

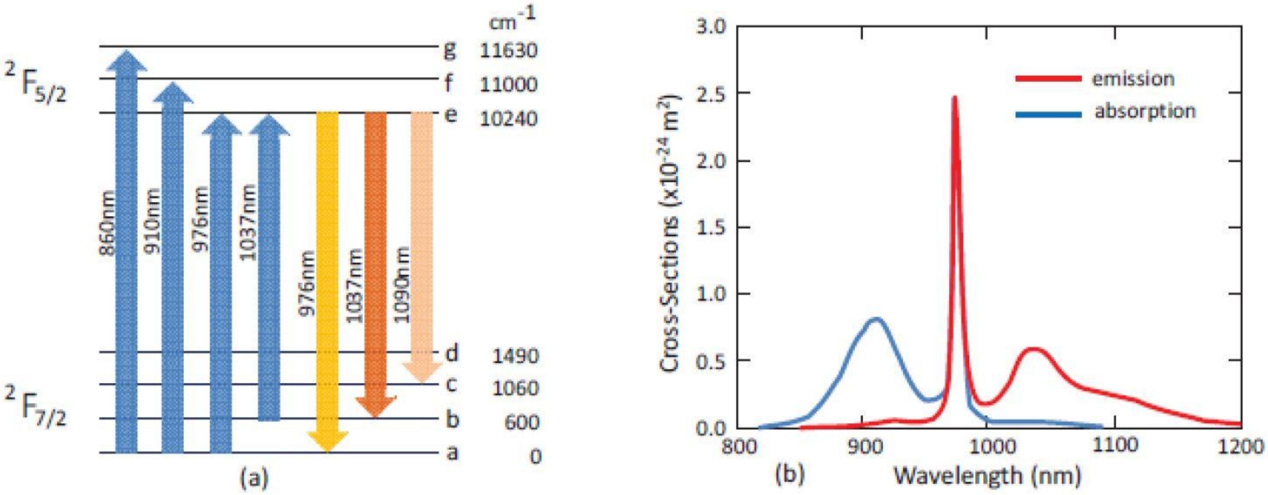

Fig. 2.3: (a) Energy level diagram of ytterbium and (b) absorption and emission cross section of Yb^{3+} [98].

2.1.2 Passive fibers

Passive fibers are optical fibers without rear-earth ions in the fiber core. This means that they can only passively propagate light. There is no light amplification during transmission; indeed, there are losses in propagation. In contrast to active fibers, propagation losses in passive fibers are significantly lower. Generally, passive fibers can be classified according to parameters such as mode number and refractive index profile [88].

2.1.2.1 Passive fibers by mode number

Optical fibers are divided into two kinds based on the number of optical routes permitted for mode propagation: single mode (SM) fiber and multi-mode (MM) fiber. Figure 2.4 displays the visual presentation of the SM and MM fibers. Single mode fiber or mono-mode fiber has a small core diameter, which is usually less than 10 μm that allows only one mode of light to travel [89]. Then the reflections formed as light travels through the fiber are limited, and beam attenuation is decreased, allowing the beam to go further. Furthermore, since optical fibers permit single light modes at specific wavelengths, their bandwidths can be expanded [100]. Single-mode fibers are chosen for long-distance communications and ultrashort laser pulses. In contrast, MM fibers are designed to simultaneously transport several modes.

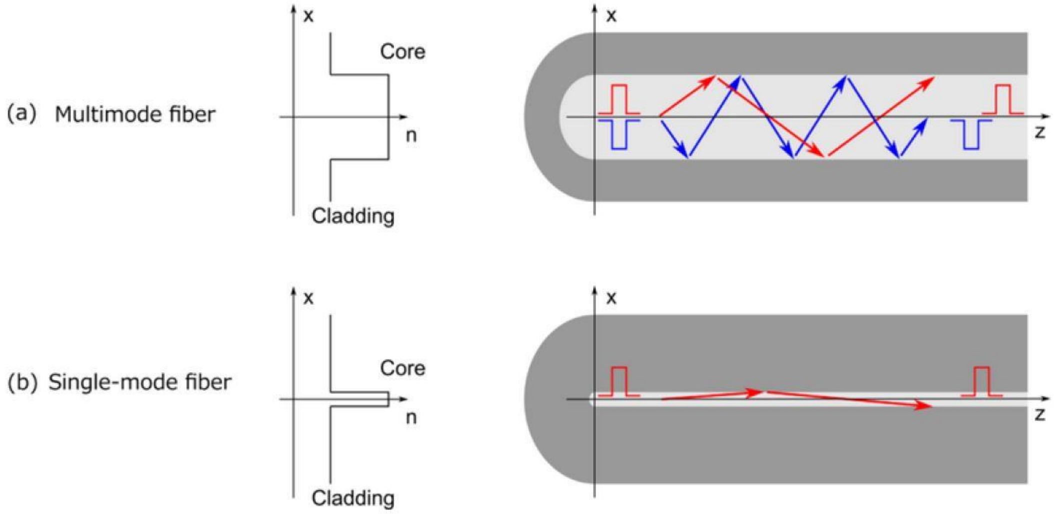

Fig. 2.4: A schematic of the (a): multi-mode fiber and (b): single-mode fiber [101].

Multiple light rays are permitted to propagate along random routes due to the large core diameter of MM fibers which are usually 50-~ 60 µm, resulting in temporary pulse broadening and data distortion. These fibers are therefore suited for local area networks with short broadcast range [102].

To calculate the number of accepted modes, a special normalized frequency parameter referred to as the V number is used, as shown in equation 2.3, where α is the core radius, λ is the vacuum wavelength, NA is the numerical aperture, n_{core} is the refractive index of the core, and $n_{cladding}$ is the refractive index of the cladding [103].

$$\mathbf{V = \frac{2\pi}{\lambda}\alpha\, NA = \frac{2\pi}{\lambda}\alpha \sqrt{n_{Core}^2 - n_{Cladding}^2}} \qquad \textbf{Eq (2.3)}$$

When the V number is less than 2.405, the fiber permits a single mode, allowing the single-mode propagation of the fiber to be evaluated for a particular wavelength. Otherwise, the V number is extremely high in multimode fibers [88].

2.1.2.2 Passive fibers by refractive index profile

According to the refractive index, there are two types of fiber. The first is called step index fiber, and the second is called graded index fiber. Step-index fibers are the simple ones, as the refractive index is uniform throughout the core and cladding. In this instance, the velocity of the incident optical ray in the fiber is dependent on the incident angle of the light [104]. As seen in figure 2.5(a), light started at a modest incident angle propagates with a higher velocity (red ray) by taking a shorter propagation path, whereas the other ray follows a longer path. Different arrival times in step-index fibers cause dispersion, resulting in a blurred and degraded signal at the optical fiber's terminus. A graded-index fiber which is shown in Figure 2.5(b) is one in which the core's refractive index varies progressively in the radial direction and reaches its highest value at the fiber center [105]. Due to the region's high refractive index, the light rays that travel along the fiber core have comparatively sluggish speeds in the fiber. This profile of refractive index permits all rays to reach the fiber end simultaneously. This decreases dispersion and allows the step-index fiber to overcome its limitations [106].

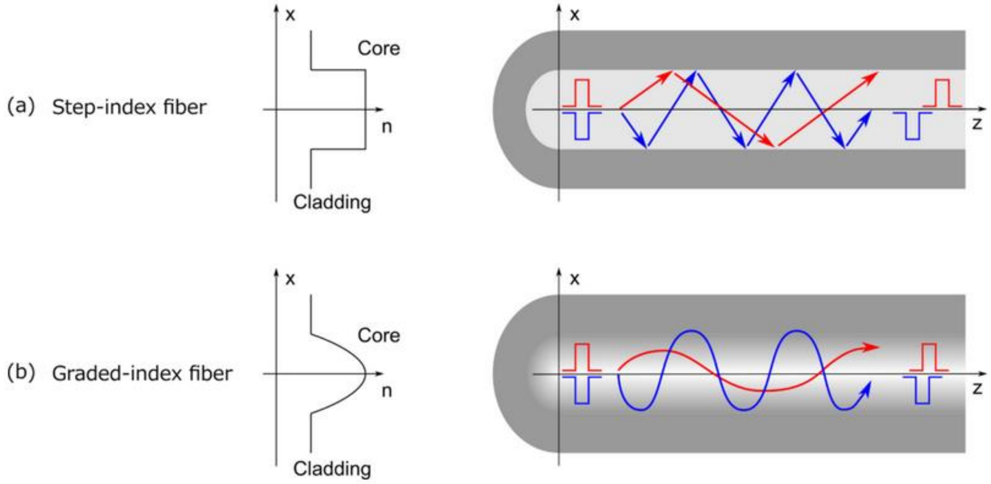

Fig. 2.5: Light transmission inside fiber: (a) a step index fiber and (b) a graded index fiber [101].

2.1.3 Polarization Maintaining fiber

Polarization maintaining (PM) fibers are certain forms of conventional optical fibers that preserve and maintain the well-oriented linear polarization state of an input signal during the propagation of the signal [107]. For certain applications, such as fiber lasers, fiber interferometers and modulators, and sensors, it is essential to maintain the fixed polarization state of light [89]. Theoretically, optical fibers are supposed to be symmetric, free of birefringence, and preserve their polarization state throughout propagation. In fact, however, the fibers always exhibit some birefringence due to local defects, which induce progressive changes in the polarization of light through power cross-coupling. Thus, the polarization condition of the output is constantly uncertain [101]. Therefore, PM fibers have been implemented to mitigate this issue.

The PM fiber is a specialized fiber that breaks the optical fiber's symmetry by inserting a systematic linear birefringence along the fiber's length (as shown in figure 2.6) to induce the fiber's high inherent birefringence [88]. As seen in figure 2.7, there are two basic orthogonal birefringence axis that direct light through the fiber. The polarization direction with a higher propagation constant is marked by the slow axis, while the polarization direction with a lower propagation constant is defined by the fast axis. However, the slow axis is better for high-quality light confinement in the presence of external perturbations. In a normal optical fiber, both axes contribute to transmission at the same velocity and making energy cross-coupling between propagation modes straightforward [108]. Thus, PM fibers are built to enforce the perpendicularly polarized modes to guide at various velocities and prevent crosstalk. According to the technique for achieving birefringence, there are two kinds of PM Fiber types: stress-birefringence fibers and form birefringence fibers. In stress-birefringence fibers, the birefringence is produced by inserting two stress rods along the cladding region on opposing sides of the core. Figure 2.6 shows how an elliptical core structure without stress rods induces form-birefringence.

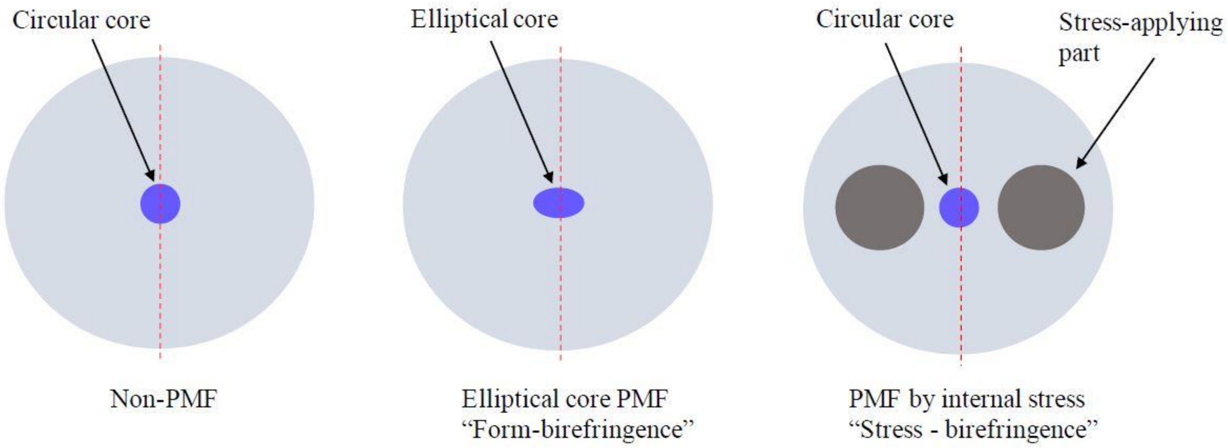

Fig. 2.6: Schematic of Non-PM fiber and PM fiber [91].

2.1.3.1 Form-birefringence fiber

Form birefringence is characterized by a highly elliptical core for the two axes (figure 2.6). In this instance, the fiber is made with an elliptical core and a circular cladding. The asymmetric design of the core generates a geometric anisotropy and an asymmetric tension on the core, which results in differing propagation constants along the fiber axes. In contrast to other polarization-maintaining fibers, the total birefringence of polarization-maintaining fibers is a combination of geometric and stress-induced birefringence [109].

2.1.3.2 Stress-Birefringence Fibers

In recent years, "Bowtie," "PANDA," and "Elliptical Jacket," [107, 110, 111] geometries have become the most popular varieties of PM fibers, and their schematic architectures are shown in figure 2.7. The contexts underlying each of these fiber architectures are the same, meaning that the fiber cores are surrounded by a glass composition with a high thermal expansion coefficient that contracts more rapidly than the remaining fiber components [112]. Whenever the fiber is cooled, these stress components generate a particular mechanical tension on the core that is responsible for the inherent birefringence. The birefringence strength is dependent on the applied stress. Consequently, a higher mechanical stress results in a higher mode propagation constant and birefringence, and the opposite [107]. All three of these designs can yield sufficient birefringence for a given application, and the choice of PM geometry is determined by the application-specific conditions [113]. For instance, "Bowtie" fibers are designed with a large numerical aperture for sensor applications, but "PANDA" fibers are used for fiber lasers and telecommunications.

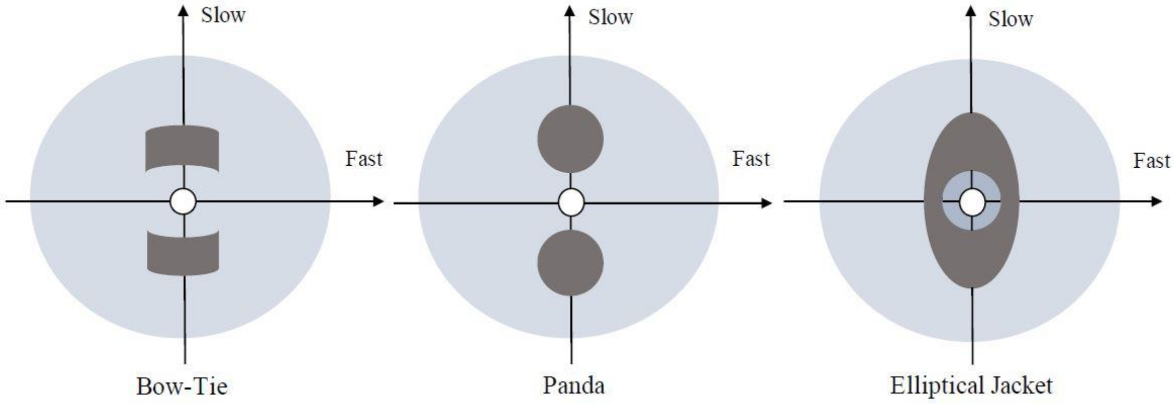

Fig. 2.7: Cross-sections of the “Bowtie,” “PANDA,” and “Elliptical Jacket” geometries [91].

2.1.4 Birefringence in fibers

Birefringence is a phenomenon that happens in fiber when the propagation of light is divided into two separate channels. This phenomenon is the result of variable refractive indices in the core of the fiber, which are affected by the polarization direction of light. Suitable optical fiber with a circular core permits the propagation of two perpendicularly polarized waves with the same propagation constant. Therefore, the polarization condition of the waves should remain unchanged during propagation. Moreover, this is not the case with genuine fibers, as their core form often varies over their length, resulting in a distinct index difference between the two orthogonal modes. Additionally, non-uniform tension owing to bending is possible [114]. Consequently, due to the changes in birefringence of the fiber the two orthogonal modes are connected. Thus, the polarization state will not be maintained across lengthy fiber lengths.

Most of the time, modal birefringence is used to describe a fiber's circular symmetry, and its formula is as follows:

$$\boldsymbol{B_m} = \left|\overline{\boldsymbol{n_x}} - \overline{\boldsymbol{n_y}}\right| \qquad \textbf{Eq (2.4)}$$

where n_x and n_y are the refractive indices for the two polarized waves.

By increasing the fiber's modal birefringence, the polarization state can be preserved. Since coupling between polarizations will be difficult, the fiber will be insensitive to changes in polarization states (caused by bending or temperature change). Birefringence for single mode fiber is typically 10^{-6}.

2.1.5 LMA and PLMA Double-clad Fibers

Though the need for high power fiber lasers and amplifiers in a variety of applications is growing quickly, the appearance of nonlinear effects prevents greater scaling of power. Although silica is not a very nonlinear material, the nonlinear effects in optical fibers can nevertheless be considerable due to their long propagation lengths and tiny mode area. To avoid such issues, the peak intensity in the fiber must be decreased, which can be accomplished by increasing the effective mode area, resulting in an increase in nonlinear thresholds. Large-mode-area (LMA) and passive-large-mode-area (PLMA) fibers are therefore introduced and utilized in high-power fiber lasers to handle high intensities with little nonlinear constraint [115].

Early LMA fiber structure was based on standard multimode step-index fiber in which the core diameter was made sufficiently large to permit an increase in the mode field diameter of the fundamental mode, at the expense of multiple transverse guided modes. Due to the fact that the optical power in the LMA fiber is dispersed throughout all guided modes, the output beam quality was inferior to that of a single mode fiber. A novel LMA fiber design with a low NA core was presented in order to improve beam quality [116]. As the normalized frequency (V number) always satisfies the single-mode criterion, a decrease in NA allows for an expansion of the mode region. However, LMA fibers with low NA are susceptible to bending, and the lowest NA that can be designed in LMA fiber format is restricted by the fabrication process and the bending loss of the fundamental mode [117].

Figure 2.8 depicts a common LMA double-cladding fiber doped with ytterbium. This type of fiber is primarily utilized in the amplifier stage, where high-intensity radiation is emitted. The LMA fiber's refractive index profile and doping distribution are both optimized for single-mode operation. The core center is comprised of a low NA with rare-earth ions scattered preferentially across the core's x-section to permit maximal gain for the fundamental mode and ensure single mode operation of the fiber laser system. The outer ring with a higher index reduces the core bend loss and the susceptibility of the mode field width to the core size fluctuation [118].

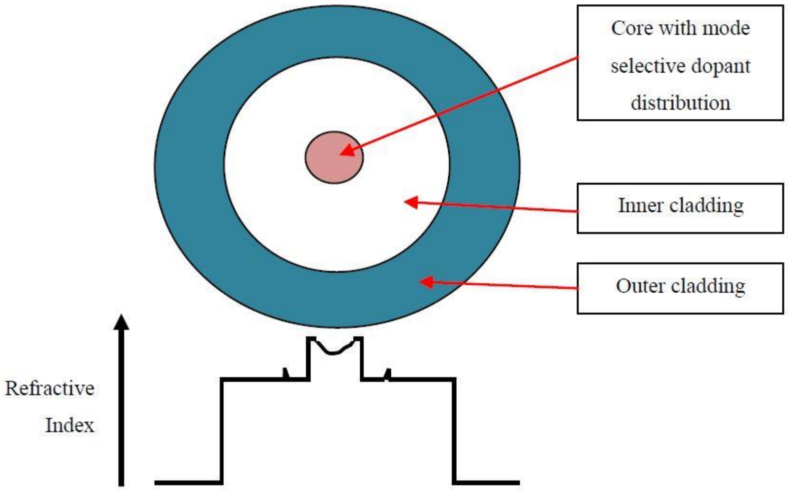

Fig. 2.8: A typical design of double clad LMA fiber.

2.2 Optical fiber component

There is a wide variety of different types of fiber-optic elements, all of which join to one another by means of fibers. Some of these are fundamentally composed of fibers, while others are composed of entirely different materials but are connected to fibers, which means that they provide fibers for input and output purposes. In other words, they offer fibers as an input and an output. The majority of fiber laser components contribute to the dispersion of the cavity. Fiber couplers, such as output couplers and wavelength division multiplexers (WDMs), fiber isolators, fiber pigtailed pump diodes, and gain fiber are typical components. All these components are easily available and based on commercially mature technology. The following are brief explanations of some components which are used in fiber optics.

2.2.1 Fiber-coupled diode lasers

For many applications, it is convenient to connect the output of a laser diode to an optical fire so that the light can be delivered to the desired location. Several benefits [119] are associated with fiber-coupled diode lasers, which are also known as fiber-integrated or fiber-pigtailed:

1- The light that comes out of the fiber has a circular and smooth (homogenized) intensity profile and a symmetric beam quality, which is particularly convenient in many circumstances.
2- For instance, setting up an end-pumped solid-state laser with a circular pump spot requires less complicated optics.
3- It becomes possible to eliminate the laser diodes and associated cooling systems, for example, from a solid-state laser head, making it more compact and freeing up more space for other components.

4- It is simple to replace defective fiber-coupled diode lasers without altering the alignment of the equipment that uses the light.
5- It is simple to combine fiber-coupled devices with other fiber-optic components.

2.2.2 Fiber-couplers

Fiber couplers are fundamental components of many fiber-optic networks. It is a device consisting of one or more input fibers and one or more output fibers. One or more outputs can receive light from a single input fiber, with the power distribution potentially dependent on wavelength and polarization. It is possible to thermally taper and fuse two or more fibers, bringing their cores into proximity along a short length of fiber, say a few centimeters. Fused couplers of this type can also be manufactured with PM fibers, which then result in polarization-maintaining couplers (PM couplers) or splitters. Some couplers make use of fibers that have been side-polished, which allows access to the fiber core. The results of a numerical simulation of the beam propagation through a fiber coupler are depicted in figure 2.9. In this portion of the process, the light distribution oscillates between the two cores of the fiber, and in the end, the original (upper) fiber retains most of its power. The coupling, on the other hand, can seem substantially different for light with different wavelengths. Consequently, this kind of coupler can only function within a specific optical bandwidth. It is possible to utilize them as dichroic couplers or beam combiners, for instance, to separate or combine two wavelength components (such as pump and signal light in a fiber amplifier). Fiber couplers are typically directional couplers, which means that optical power that is supplied into one of the input ports cannot practically flow back into one of the input ports. Return loss is frequently specified, and its value, which indicates how much weaker the back-reflected light is in comparison with the input, is typically rather high. This value may be found in many optical designs (many tens of decibels) [120].

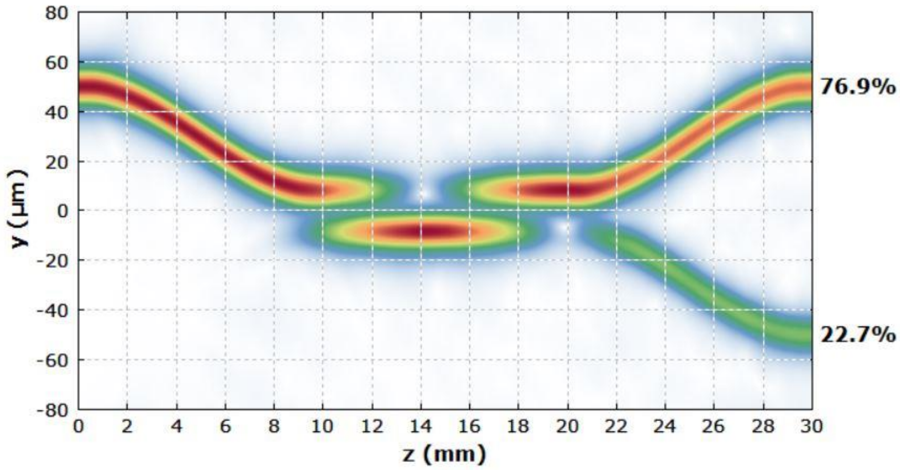

Fig. 2.9: Amplitude distribution in a fiber coupler, obtained with a numerical simulation of beam propagation, done with the software RP Fiber Power [120].

2.2.3 Fiber-connectors

In order to offer temporary connections between fiber-coupled devices, fiber connectors are frequently utilized as the terminations of optical fiber cables (a kind of removable fiber joint). They serve the same purpose as electrical connectors. A connector assembly typically consists of an adapter and two connector plugs, with one fiber placed into each connector plug. The most popular types of fiber connectors are ST, FC, SC, and LC, and there are numerous variants of each [121].

ST connectors are the most popular for multimode fiber-optic networks, which are typically utilized within buildings. The fiber is put in a relatively long, cylindrical, keyed ferrule (often made of ceramic) that provides close physical contact between the fiber ends. ST connections include a bayonet mount with a spring.

FC ("fixed connection") connectors are a common form for single-mode fibers. They provide excellent mechanical isolation of the contact, permitting their usage in high-vibration situations, but they must be handled with care, with the ferrule's key aligned when plugged in. This key prevents the fiber from rotating when the plug is inserted into the socket. This is essential for fibers with slanted ends and polarization-maintaining fibers. Unfortunately, there are two variants with key widths of 2 mm (reduced version, "type R") and 2.14mm ("type N"), which are mutually incompatible. The standard version of FC/PC utilizes "physical contact" with a slightly rounded fiber surface; the fiber tip is polished upon insertion into the ferrule. The spring-loaded ferrule provides a well-defined contact force when the connection is inserted. FC/SPC and FC/UPC connectors feature superior fiber tip polishing (with "super" or "ultra" polish). This results in increased return loss and decreases insertion loss. FC/APC connectors utilize angled fiber ends to achieve a high return loss at the expense of increased insertion loss. Obviously, fiber ends with a precisely controlled tilt angle are more difficult to manufacture, and the two angled fibers must be placed in such a way that their surfaces align.

SC connectors (sometimes known as "subscriber connectors") are push/pull snap-in connections for single-mode fibers. The fiber is contained within a ceramic ferrule, and its orientation is determined by a key. The orientation of the connector's rotations is dictated by its rectangular shape. The snap-in mechanism allows for less delicate handling than FC connectors.

LC connectors (sometimes known as "Lucent connectors") come from "small form factor" connectors (SFF connectors). It contains a ferrule with a diameter of only 1.25mm. It is typically employed for single-mode fibers.

2.2.4 Fiber-Collimators

Frequently, it is required to convert the light output of an optical fiber into a free-space collimated beam. In theory, a simple collimation lens (see figure 2.10) is adequate for this function. Nevertheless, the fiber end must be anchored at a distance from the lens that is roughly equivalent to the focal length. There are two fundamental types of these devices, distinguished by how the fiber is mounted. Some can be connected straight to bare fibers which is the most affordable and small option. Other fiber collimators have a mechanical connection to a fiber connector [122].

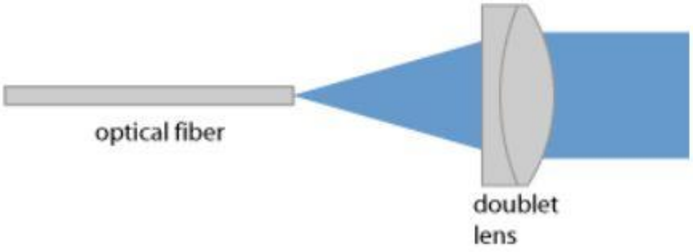

Fig. 2.10: Using a lens as a collimator at the output from a fiber [122].

2.2.5 Optical Isolators and Circulators

Devices known as optical isolators are those that allow light to be transmitted in one direction while blocking transmission in the other direction. To be more specific, they display a propagation loss that is quite low in one direction, but a propagation loss that is significantly higher in the other direction. While most isolators are coupled to waveguides, such as optical fibers, others are utilized with beams that travel through free space. An optical circulator with at least three optical ports is an alternative form of this device. Light injected into port 1 will escape through port 2, while input at port 2 will be transferred to port 3, and input at port 3 will be delivered to port 1 [123].

2.2.6 Optical Saturable Absorbers

A saturable absorber is an optical component with a certain light absorption loss that decreases with increasing optical intensities. This type of nonlinear absorption can occur, for example, in a medium containing absorbing dopant ions when a strong optical intensity depletes the ground state of these ions. Excitation of electrons from the valence band into the conduction band reduces the absorption of photon energies just above the band gap energy in semiconductors and leads to the same effects. There are also artificial saturable absorbers, in which there is no actual absorption but an optical loss that decreases with increasing optical power. The primary applications of saturable absorbers are passive mode locking (which I will discuss in the following chapter) and laser Q switching, such as the generation of short optical pulses.

Some saturable absorbers are reflecting devices. Figure 2.11 illustrates how the reflectance of a slow saturable absorber device varies with the saturation parameter, which is really proportional to the incident pulse energy. The reflectance of a pulse is computed as the ratio of reflected energy to incident pulse energy. Observe that the real reflectance varies over time; it is initially lower but rises as absorber saturation occurs [124].

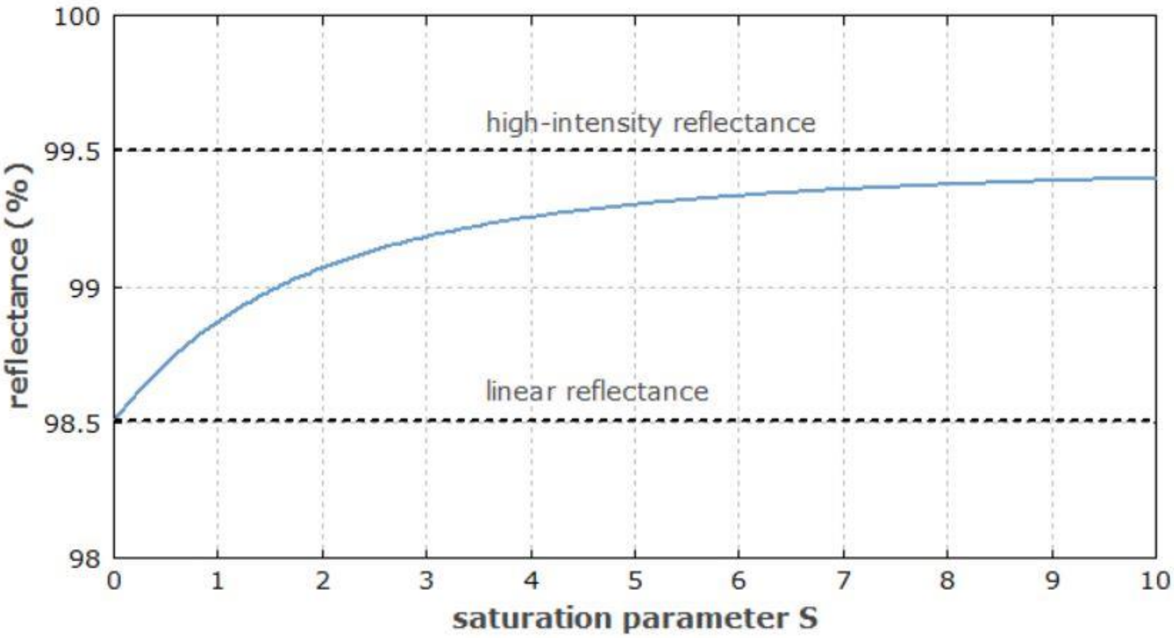

Fig. 2.11: demonstrates the relationship between the reflectance of a slow saturable absorber and the saturation parameter S, which is the pulse fluence divided by the saturation fluence of the device. The modulation depth (maximum reflectance change) is 1 percent, and the no saturable losses are 0.5 percent [124].

Figure 2.12 describes the structure of typical semiconductor saturable absorber mirrors (SESAMs), which we will discuss in Chapter 3.

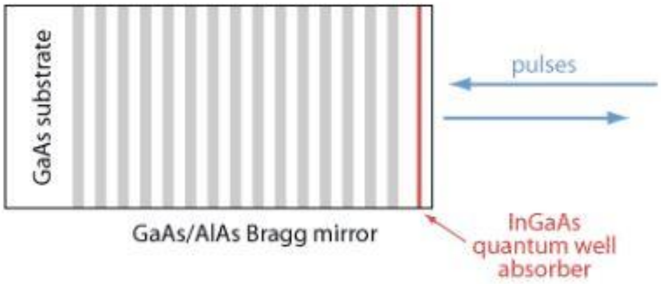

Fig. 2.12: Structure of a typical SESAM.

2.2.7 Wavelength division multiplexing (WDM)

Wavelength division multiplexing is a type of frequency division multiplexing - a technique that combines, transmits, and separates optical signals of distinct wavelengths, as shown in figure 2.13. It is primarily employed in optical fiber communications to transport data through many (or even more) wavelength-differing channels. Thus, the transmission capacity of fiber-optic networks can be significantly boosted, maximizing the utilization of not only the fibers but also the active components, such as fiber amplifiers. In addition to its usage in telecommunications, wavelength division multiplexing has other applications, such as interrogating many fiber-optic sensors inside a single fiber [125].

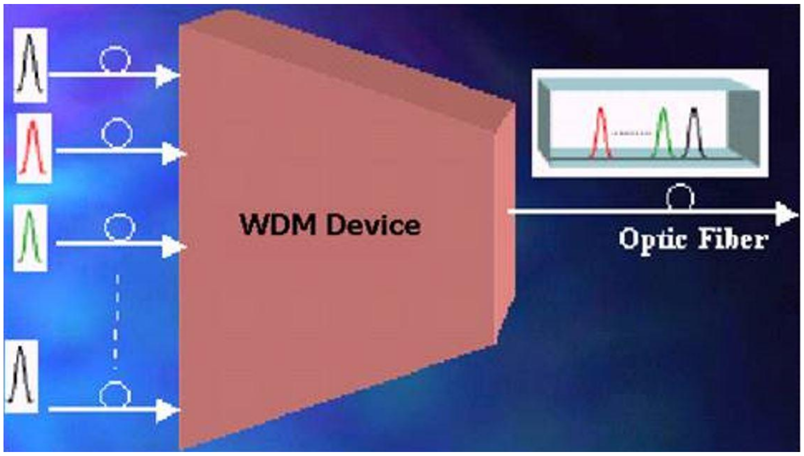

Fig. 2.13: Combining optical signal with different wavelengths at WDM inside the fiber.

2.2.8 Fiber-optic pump combiners

Double-clad, rare-earth-doped fibers serve as the foundation for fiber lasers and amplifiers with high output power. In theory, it is possible to inject pump and signal light into such a fiber by focusing the light coming from this location onto the bare fiber end. In reality, this is commonly done for amplifiers and laser devices during the development phase. However, industrial lasers should be built on an all-fiber configuration in which fiber-coupled pump laser diodes are directly connected to the active fiber via certain passive transport fibers, thereby avoiding any air gaps in the beam path. In addition to these simple transport fibers (which are typically multimode fibers), one also requires fiber-optic pump combiners (or pump couplers), which are specialized fiber couplers used to interface with the active fiber. This method significantly improves the robustness and stability of the devices. Multiple kilowatts of power can be securely managed by some models [126].

2.2.9 Fiber Bragg gratings

A periodic or aperiodic disruption of the effective refractive index in the core of an optical fiber constitutes a fiber Bragg grating (FBG), which is described in figure 2.14. Generally, the disruption is roughly periodic across a particular length, such as a few millimeters or centimeters, and the period is on the order of hundreds of nanometers, or significantly more for long-period fiber gratings. For short time intervals of index modulation, the refractive index disruption results in the reflection of light (propagating through the fiber) in a small range of wavelengths. Fulfilling the Bragg condition is:

$$\boldsymbol{\frac{2\pi}{\Lambda} = 2 \times \frac{2n_{eff}}{\lambda} \rightarrow \lambda = 2n_{eff}\Lambda} \qquad \textbf{Eq (2.5)}$$

Where Λ is the grating period, λ is the vacuum wavelength, and n_{eff} is the effective refractive index of light in the fiber. The condition basically states that the wavenumber of the grating corresponds to the difference between the (opposite) wave vectors of the incident and reflected waves. In this situation, the complex amplitudes corresponding to the reflected field contributions from various regions of the grating are in phase, so they can sum constructively; this is a form of phase matching.

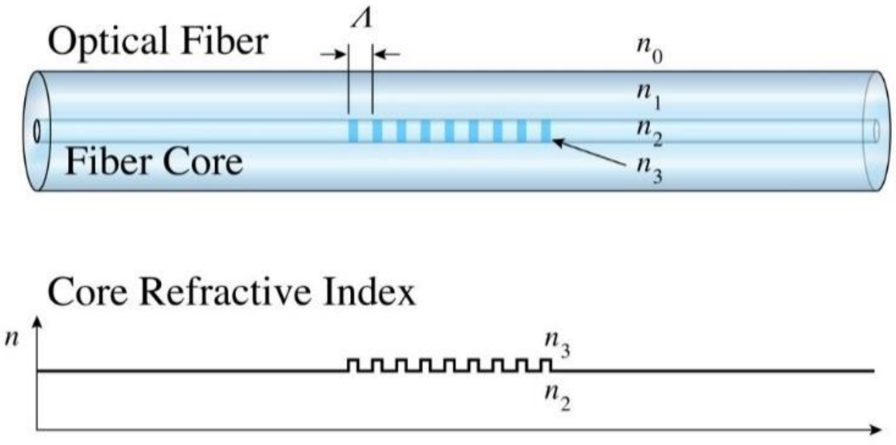

Fig. 2.14: A FBG structure and refractive index profile.

If the grating is sufficiently long, even a weak index modulation (with an amplitude of 104) is adequate to achieve nearly complete reflection. Other wavelengths of light that do not satisfy the Bragg requirement are almost unaffected by the Bragg grating, with the exception of side lobes that frequently appear in the reflection spectrum. The fibers grating reflection bandwidth is influenced by both the length and intensity of the refractive index modulation. Long gratings with weak index modulation produce the narrowest bandwidth values, which are suitable for applications such as the production of single-frequency fiber lasers and specific optical filters and its principle in shown in figure 2.15. Large bandwidths are attainable not just with short, robust gratings but also with longer, aperiodic designs [127].

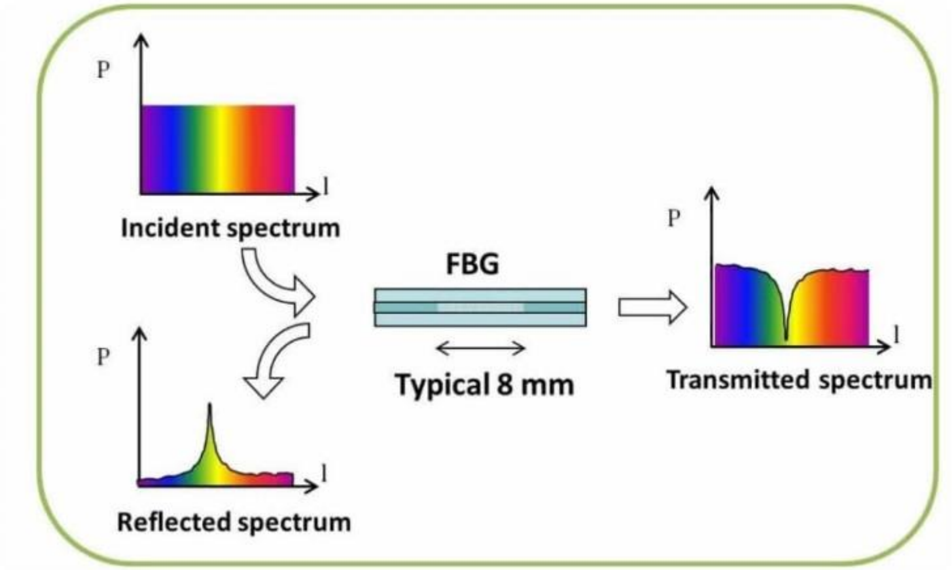

Fig. 2.15: Working principle of FBG [128]

Chapter 3: Ultrashort pulsed fiber lasers and characterization

3.1 Introduction

In fiber lasers, the mode-locking concept is generally utilized to generate ultrashort pulses, also known as dissipative solitons [129]. A laser cavity resonator includes a set of oscillating frequencies which reflect more gain than loss following a cavity round trip; these frequencies are referred to as longitudinal modes. For a standard linear cavity, the mode separation (ΔF) is specified as $\frac{C}{2L}$, and for a loop cavity, it will be $\frac{C}{L}$, in which L is the cavity length and c is the speed of light [130]. Since these longitudinal modes oscillate independently, a continuous laser is produced. In fact, a laser is classified as mode-locked or phase-locked if the phases of neighboring modes are fixed and the intensity is confined at the points where all the modes reach constructive interference, as shown in figure 3.1 [131]. According to the fixed phase relation, the periodic response of a laser is constant across time, and the cavity round trip time determines the repetition rate. Furthermore, when enough longitudinal modes are locked, a very powerful pulse can be generated. In reality, mode-locked laser cavities have additional passive or active devices to periodically modify the resonator losses [132].

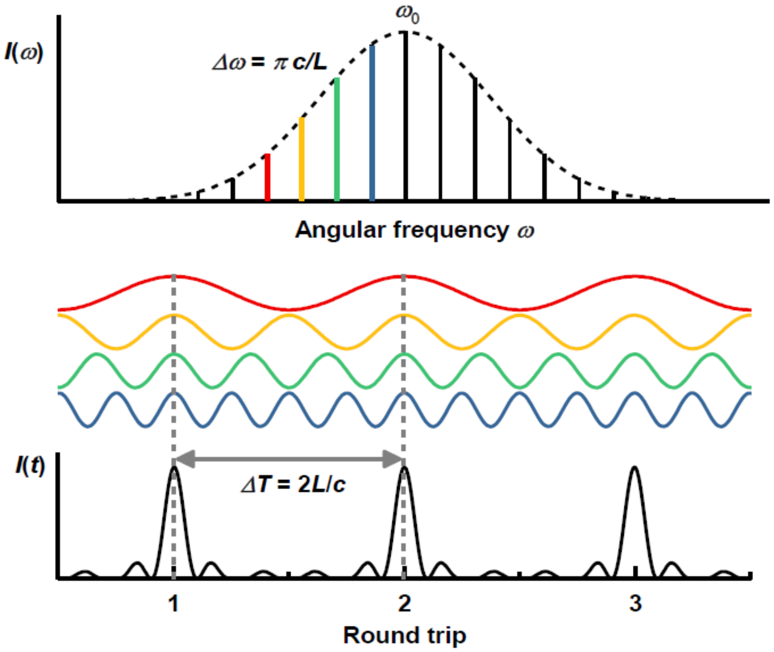

Fig. 3.1: Schematic of a constructive interference for output of mode-locked laser [133].

Kuizenga and *Siegman* initially studied active mode-locking in the 1970s. This term "Active" describes a technique for generating ultrashort pulses using an externally regulated electric signal. Using a phase or amplitude modulator, the active mode-locked laser method's essential structure is realized. When the modulator's frequency is synchronized with the laser's repetition rate, only the modes with modulated phase survive in the laser's cavity [134]. The cavity round-trip frequency is dependent on the modulation potential [135]. Since the output of a pulsed laser is dependent on an external signal, active mode-locking provides advantages for a variety of applications, particularly in telecommunications [135].

Widespread use of passive mode-locking provides shorter optical pulses than active mode-locking. In passive mode-locking, non-linear features (such as saturable absorbers placed within the cavity) establish the pulse, therefore no external modulations are required. In contrast to the previous method, the "Passive" mode-locking methodology relies solely on the saturable absorbing component for loss modulation. In addition, graphite nanotubes, non-linear amplifying loop mirror (NALM) [136], semiconductor saturable absorbers, non-linear polarization evolution (NPE), non-linear optical loop mirror (NOLM), additive pulse mode-locking (APM) [137, 138], and self-phase modulations (SPM) [139] are additional passive mode-locking ways.

3.2 Nonlinear Effects and Pulse Propagation in Optical Fibers

Generally, optical pulses propagating in a nonlinear dispersive system will experience nonlinear distortion, with the effects likely to be more pronounced for greater amplitude pulses. Pulse distortion caused by linear dispersion, including group velocity dispersion, can result in the evolution of optical pulses that is complex. The nonlinear effects can mix with or cancel out the linear dispersive effects, hence influencing the pulses' form and spectrum.

The expression for the electric field E of a propagating optical pulse is [140]:

$$\boldsymbol{E(r,t)=\frac{1}{2}x\{F(x,y)A(z,t)exp[i(\beta_0 z-\omega_0 t)]+c.c.\}} \qquad \textbf{Eq (3.1)}$$

where *x* is the polarization unit vector, A(z, t) is the slowly varying pulse envelope, F(x, y) is the transverse distribution inside the fiber core and β_0 is the propagation constant at the carrier frequency ω_0.

3.2.1 Dispersion in Pulse Propagation

Various spectral components associated with the pulse will travel at different speeds, hence dispersion plays a significant role in the propagation of pulses in optical fiber. This dispersion is evidenced by the frequency dependence of the refractive index n(ω). The combined effect of dispersion and nonlinearity may result in pulse broadening and soliton production [140]. In contrast to laser mirrors, which have distinct GDDs per reflection, dispersion accumulates along the entire fiber. Moreover, because the dispersion of fibers is a combination of material and waveguide dispersion, it is convenient to account for these factors collectively with a mode-propagation constant [141]. To comprehend the effect of dispersion, the mode propagation constant must be derived using a Taylor series at ω_0, the center frequency of the pulse envelope, and can be represented as follows:

$$\boldsymbol{\beta(\omega) = \beta_0 + \beta_1(\omega - \omega_0) + \frac{1}{2}\beta_2(\omega - \omega_0)^2 + \cdots} \qquad \textbf{Eq (3.2)}$$

where β_1 and β_2 are related to the refractive index n and its derivatives through the relations are:

$$\boldsymbol{\beta_1 = \frac{1}{v_g} = \frac{n_g}{c} = \frac{1}{c}(n + \omega\frac{dn}{d\omega})} \qquad \textbf{Eq (3.3)}$$

$$\boldsymbol{\beta_2 = \frac{1}{c}(2\frac{dn}{d\omega} + \omega\frac{d^2n}{d\omega^2})} \qquad \textbf{Eq (3.4)}$$

where v_g is the group velocity and n_g is the group index. Therefore, β_1 is the inverse of the group velocity, which is the speed of the envelope of an optical pulse travelling through the fiber and the group velocity dispersion (GVD) parameter is denoted by β_2.

Accordance with equation (3.4), if $\beta_2 > 0$, the fiber exhibits normal dispersion. The higher wavelength components will propagate faster than the lower wavelength components of the same optical pulse. The reverse occurs if $\beta_2 < 0$, totally, termed as the anomalous dispersion region. The dispersion parameter D is usually used to represent β_2 and the relation between the two are as follows [140]:

$$\boldsymbol{D = -\frac{2\pi C}{\lambda^2}\beta_2} \qquad \textbf{Eq (3.5)}$$

The effect of dispersion on frequency components in the frequency domain will lead each component to travel at a different speed. Based on the dispersion parameter, the pulse will be either stretched or compressed in the temporal domain, but no change will be detected in the frequency domain because dispersion alone does not generate new frequency components. D is often expressed per unit length in terms of ps/nm/km, and its value for standard fiber is zero near 1.31 μm. This wavelength is known as the wavelength of zero dispersion, or λ_D. Third order dispersion becomes dominant, when it is close to λ_D.

3.2.2 Self-Phase Modulation as a non-linear Effects in Pulse Propagation

The presence of light in a fiber causes a (tiny) change in the refractive index (RI) of the fiber. This is because the electromagnetic field that constitutes the light acts on the atoms and molecules that make up the glass. This is called the “Kerr Effect”.

The time domain and frequency domain of a laser pulse are a Fourier transform pair of each other. This indicates that the shorter the pulse duration must be the wider the bandwidth. The concept of SPM for the development of extremely short pulses is to maximize the frequency bandwidth in order to generate the matching short pulse in time. Self-phase modulation (SPM) is an efficient method for expanding the frequency range by producing new frequencies.

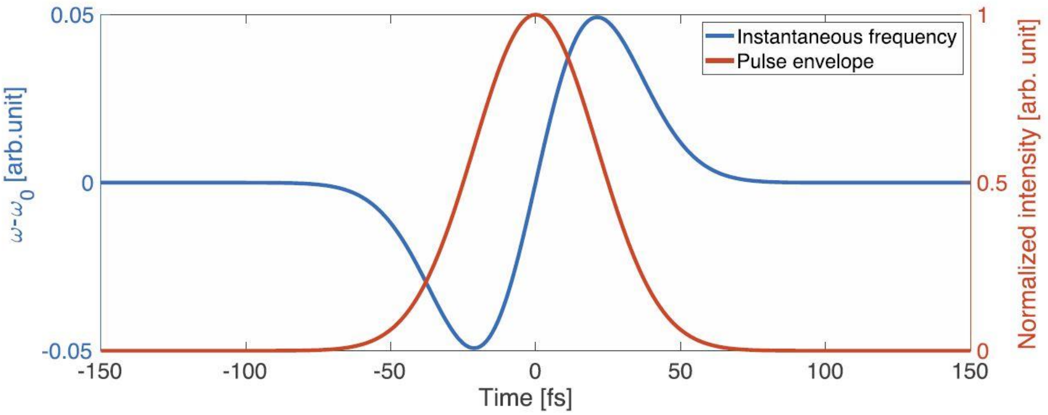

Fig. 3.2: The instantaneous frequency $\Delta\omega$ for SPM based spectral broadening. The red curve shows the pulse envelope, and the blue curve shows instantaneous frequency to the center frequency (ω−ω0) [142].

As a result of Kerr effects at different points within a single pulse of light in the fiber the RI of the glass is different. So, there is a (tiny) difference between the RIs at the leading edge, at the trailing edge, and in the middle. This changes the phase of the light waves that make up the pulse. Changes in phase amount to changes in frequency. Therefore, the frequency spectrum of the pulse is broadened. The frequencies at the pulse's leading edge are reduced, but the frequencies at the pulse's trailing edge are increased, as shown in figure 3.2. As a result, the pulse's spectrum is continuously broadened as it propagates through the fiber. The positive chirp introduced by SPM is observed to be well-behaved and almost linear at the pulse's center, that means SPM creates a chirp (a gradual shift in frequency) over the whole duration of pulses. Typically, the spectrum depends on the pulse shape and the initial chirp imposed on the pulse. The presence of the same chirp at two different values of time indicates that the pulse has the same instantaneous frequency at two different moments. Substantively, these two points represent two waves with the same frequency but distinct phases that, depending on their relative phase difference, might interfere constructively or destructively. As a result of such interference, the typical oscillating structure of the pulse spectrum is observed [143, 144]. Note that for initially chirped pulses, the same chirp can typically occur at many time values. The position of the spectrum's outermost intensity peak provides an estimate of the spectrum's width.

Once an electric field E is added to a transparent dielectric medium, the electron-charge distributions in the medium will be distorted. This will result in an induced polarization P in the medium that, to a first order approximation, is linear with respect to the applied E field. Nevertheless, if a high electric field E is applied, the polarization response in the applied field may become nonlinear. The following equation can be used to express the total polarization P caused by a powerful electric field E [140]:

$$\boldsymbol{P = \varepsilon_0(\chi^{(1)}.E + \chi^{(2)}\colon EE + \chi^{(3)} \vdots EEE + \cdots)} \qquad \textbf{Eq (3.6)}$$

where ε_0 represents the vacuum permittivity and $\chi_{(j)}$ (j=1, 2…) represents *j*th order susceptibility. P is primarily determined by the linear susceptibility $\chi^{(1)}$, which is associated with the refractive index n and the attenuation constant α. Nonlinear effects like second harmonic generation and sum frequency generation are related to the second order susceptibility $\chi^{(2)}$. Centro-symmetric materials such as silica fibers, have zero second order susceptibility, implying that, $\chi^{(2)}=0$. Regarding the third order susceptibility $\chi^{(3)}$, it is primarily responsible for phenomena including third harmonic generation, nonlinear variation of the index of refraction, and four-wave mixing.

The third order nonlinearity creates an intensity-dependent refractive index, which is the primary cause of phase modulation inside a single optical pulse and SPM will generate. The nonlinear dependency of the refraction index on signal intensity is given by [145]:

$$\boldsymbol{n = n_0 + n_2 I} \qquad \textbf{Eq (3.7)}$$

where n_0 is the linear refractive index and n_2 is the nonlinear index of refraction. In addition, the signal intensity *I* which is associated with the electric field is:

$$\boldsymbol{I = |E|^2} \qquad \textbf{Eq (3.8)}$$

In a lossless fiber, the net phase shift is related to the intensity and effective fiber length L_{eff}, then we have [146]:

$$\boldsymbol{\emptyset(t) = 2\pi(n_0 + n_2 I)\frac{L_{eff}}{\lambda}} \qquad \textbf{Eq (3.9)}$$

The total phase shift derivatives, given by:

$$\boldsymbol{\frac{d\emptyset(t)}{dt} = \frac{4\pi n_2 L_{eff}}{\lambda}\frac{dI}{dt} = \frac{4\pi n_2 L_{eff}}{\lambda A_{eff}}\frac{dP}{dt} = \omega(t)} \qquad \textbf{Eq (3.10)}$$

The P is instantaneous power and A_{eff} is the effective mode area of the optical fiber. There is a correlation between the rate of phase change and the instantaneous angular optical frequency of the pulse which is:

$$\boldsymbol{d\omega = \frac{d\emptyset}{dt}} \qquad \textbf{Eq (3.11)}$$

Therefore, it is possible to obtain the instantaneous frequency as:

$$\boldsymbol{\omega(t) = \omega_0 - \frac{4\pi n_2 L_{eff}}{\lambda A_{eff}}\frac{dP}{dt}} \qquad \textbf{Eq (3.12)}$$

According to the above formula, it should come as no surprise that the SPM-induced spectral change has a relation to the changing rate of the instantaneous power of the pulse once the length of the fiber remains the same. When a Gaussian pulse is taken into consideration, the leading edge of the pulse will have a positive $\frac{dP}{dt}$ value. As a result, the value of $d\omega$ will be negative, which indicates that the frequency has decreased. Also, at the trailing edge of the pulse, $d\omega$ will be positive, the frequency will have an upshift, and the generated spectrum because of SPM will be symmetrically broadened from the central frequency. If the pulse is asymmetric, the $d\omega$ will be different at the leading and trailing edges of the pulse, which will cause an asymmetrical broadening of the spectrum.

3.3 All-normal-dispersion fiber lasers

Due to the generation of femtosecond pulses, GVD compensation is one of the most prevalent requirements. In these instances, prisms, chirped mirrors, and diffraction gratings have been utilized to manage the GVD [147]. In addition, mentioning the most recent femtosecond pulse lasers, the pulse generation is involved with the system's dispersion and nonlinearity [148]. Typically, normal, and anomalous GVD partitions are incorporated into ultrashort laser cavities such that the final average cavity dispersion can be either in the normal or anomalous regime. When a laser is designed with entirely anomalous GVD fibers and operated using an anomalous GVD scheme, the soliton pulse creation becomes unstable due to the soliton area theorem, which restricts the pulse's energy [149]. The mode locked lasers with standard GVD fiber segments result in the generation of highly energetic pulses [150]. Consequently, mode-locked all normal dispersion (ANDi) fiber lasers have attracted a great deal of interest because of several experiments undertaken to extract high-power optical pulses, straight from laser oscillators [151-153]. The principle of all-normal dispersion lasers describes systems that exclusively contain normally dispersive elements. Normal GVD causes spectrum broadening of the pulse, which is compensated by gain saturation and spectral filtering [154].

3.4 Mode-locking

Here, the mode-locking principle will be discussed, with a focus on passive mode-locking using an artificial saturable absorber, as this is the method of choice for the ytterbium doped fiber lasers in this thesis.

While Q-switching can produce laser pulses [155], mode locking (ML) is the only method capable of producing the shortest laser pulses. That means laser mode locking is required to generate ultrashort pulses with a duration of a few picoseconds or less. It is based on numerous modes with coupled phases exiting in the laser cavity. Self-starting needs the laser cavity to prioritize short pulses over continuous-wave light. The mode-locked pulse then evolves for several hundred to several thousand round trips before reaching the stable condition [156]. However, unless the dispersion and pulse shaping mechanisms are properly controlled, the pulse length cannot advance to the ultrashort range. By balancing the cavity group delay dispersion and the nonlinear refractive index shift from SPM, the tiny anomalous dispersion required for soliton production often enables shorter pulses. To do this, a rigorous phase relationship must be established between the numerous longitudinal modes that can exist in a laser cavity of a specific length.

For both passive and active mode locking, supporting short pulses requires a broad spectrum. The relation between the pulse width $\Delta\tau_p$ and the spectral width $\Delta\omega_s$ is defined by the Fourier transform limitation, which states that, given a Gaussian pulse, the time-bandwidth product is constant [157].

$$\boldsymbol{\Delta\tau_p \times \Delta\omega_s \geq 0.441} \qquad \textbf{Eq (3.13)}$$

For a hyperbolic secant (sech) pulse shape, this product will be about 0.315. Thus, the shortest pulse duration at 1064 nm with a spectral bandwidth of 20 nm is approximately 83 fs for Gaussian pulses and 59 fs for sech pulses.

3.4.1. Superposition of longitudinal modes

A laser resonator's electromagnetic pulse can be characterized as a superposition of plane waves with varying wavelengths. The possible longitudinal mode wavelengths in a resonator are described as [158]:

$$\boldsymbol{n \times \lambda_n = 2 \times L} \qquad \textbf{Eq (3.14)}$$

and L is the resonator length and λ_n is the wavelength of the longitudinal mode. In concept, a considerable number of modes with distinct frequencies can occur and these modes will be phase and amplitude independent. Then, the total electric field in the resonator will be:

$$\boldsymbol{E(\mathcal{Z},t) = \sum_n E_n(\mathcal{Z},t) = \sum_n E_{0,n^{e^{ik_n\mathcal{Z}-i\omega_n t}}}} \qquad \text{and} \qquad \boldsymbol{E_{0,n} = |E_{0,n}|e^{i\emptyset_n}} \qquad \textbf{Eq (3.15)}$$

where $E_{0,n}$ is the complex amplitude of the n-th mode and φ_n is phase. Assuming that all modes have the same amplitude, the intensity is calculated by:

$$\boldsymbol{I(\mathcal{Z},t) \propto E(\mathcal{Z},t)E^*(\mathcal{Z},t) = |E_0|^2 \sum_{n=1}^{N}\sum_{m=1}^{N} e^{i(\emptyset_n-\emptyset_m)}\,(m-n)\Omega(\frac{\mathcal{Z}}{c}-t)} \qquad \textbf{Eq (3.16)}$$

and

$$\boldsymbol{\Omega = \omega_{n+1} - \omega_n = \frac{\pi c}{L}} \quad \textbf{Eq (3.17)}$$

If all modes have a fixed phase, then we have:

$$\boldsymbol{I(\mathcal{Z}, t) \propto |E_0|^2 e^{i\delta\emptyset} \sum_{n=1}^{N} \sum_{m=1}^{N} e^{i(m-n)\Omega(\frac{\mathcal{Z}}{c} - t)}} \quad \textbf{Eq (3.18)}$$

If we have the following conditions, the second exponential function in the above formula will equal to 1 for all terms of the sum.

$$\boldsymbol{\frac{\Omega}{c}(\mathcal{Z} - ct) = 2\pi \times j \Leftrightarrow \mathcal{Z} - ct = 2L \times j} \quad \textbf{and} \quad \boldsymbol{j = 0, 1, 2, \ldots.} \quad \textbf{Eq (3.19)}$$

and the maximum of I will be:

$$\boldsymbol{I_{max} = N^2 |E_0|^2 = N^2 I_0} \quad \textbf{Eq (3.20)}$$

As a result of deriving the spatial and temporal distances of consecutive pulses as a function of the maximum intensity Imax, one obtains:

$$\boldsymbol{\Delta\mathcal{Z} = 2L} \quad \text{and} \quad \boldsymbol{\Delta t = \frac{2L}{C} = T} \quad \textbf{Eq (3.21)}$$

This indicates that the peak of intensity repeats with the revolution time T of the laser cavity and always exists one maximum inside the resonator. Using the fixed phase relation between the large number of modes in the resonator, regular pulses with a peak intensity of I_{max} will develop, proportional to the square of the number of involved modes which is shown in figure 3.3.

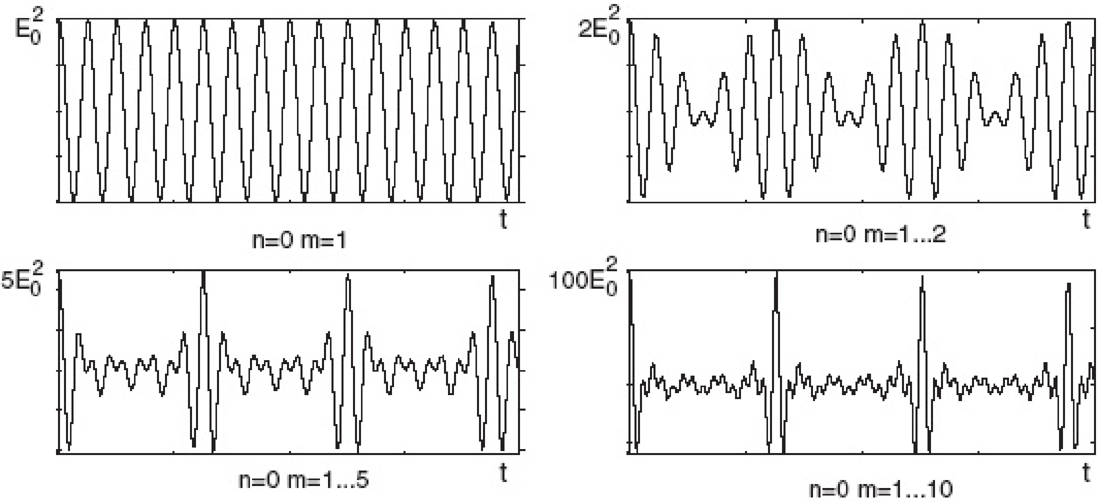

Fig. 3.3: A superposition of many longitudinal modes with a constant phase difference. The intensity of these pulses is proportional to the number of modes engaged [159].

3.4.2 Passive mode-locking using SESAM

Since the first picosecond pulses were produced simply using a passive, saturable absorber element, such as a semiconductor [160, 161], passive mode locking has been used to produce the ultrashort pulses [162]. Use of fast or slow saturable absorbers, nonlinear amplifying loop mirrors (NALM), Kerr-Lens mode locking (KLM), additive pulse mode locking (APM) and polarization APM, as artificial saturable absorbers are nonlinear optical techniques for passive mode locking.

SESAMs have become the most extensively utilized and low-cost mode-locking mechanism for mode-locked fiber lasers among the various approaches. SESAMs provide a new method for designing passively mode-locked, robust pulsed lasers. These components may easily replace the end cavity mirrors of various lasers [134]. Distributed Bragg reflector (DBR) and semiconductor quantum wells (QWs) make up the two primary components of SESAM's overall design. Figure 3.4 depicts a simple illustration of the SESAM. To prevent absorption in this area, the Bragg mirror is composed of a semiconductor material with a high bandgap, and the most common material is GaAs/AlAs [163]. Typically, the semiconductor material used for the saturable absorber layer must have a direct band gap (such as GaAs) but an energy gap that is a little smaller than the photon energy [131]. The inter-band transition between the conduction band and the valence band is related to the saturable absorption.

Figure 3.5 depicts a schematic illustration of the operation of semiconductor saturable absorbers. Once the optical pulse (photons) with enough photon energy hits the absorber layer, electron-hole pairs are formed by absorbing the photon energy and stimulating electrons from the valence band to the conduction band. During the 10 to hundreds of femtoseconds (fs) of the excitation time, it is possible to reveal a partial recovery of carriers' absorption in respective bands. Whenever the absorption time is long enough (in the range of picoseconds (ps) or nanoseconds (ns)), recombination and trapping, remove the electrons from the conduction band. Having two diverse time scales assists in achieving mode-locking. In other words, the rapid time intervals help to the shaping and the slow time constantly aid in the self-starting of mode-locked lasers. Consequently, SESAMs allow the acquisition of mode-locked lasers that can initiate themselves [164]. Low-intensity pulses are absorbed during transmission through the SESAM, while high-intensity pulses are permitted to transmit with minimal loss, resulting in pulse compression. As the pulse travels through the saturable absorber, it becomes shorter during every round trip and begins mode-locking. [165].

Several crucial characteristics, such as non-linear intensity response, absorption recovery time, bandwidth, and modulation depth, have a direct impact on the performance of SESAMs. To obtain a mode-locked laser system with the SESAM, these parameters must be well adjusted. QW structure influences the saturation and non-linear intensity response characteristics.

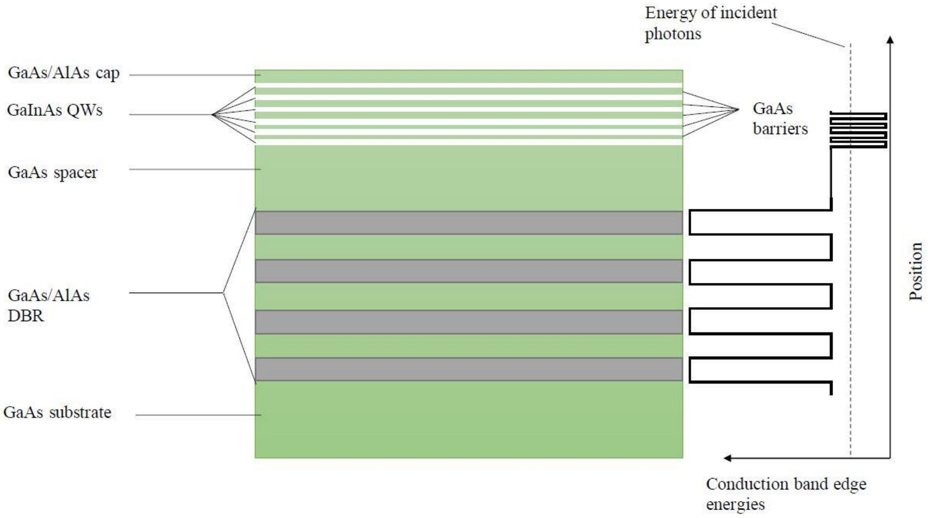

Fig3.4: Structure of the general SESAM [166].

In addition, the QW is defined as a "potential well" made of layers of semiconductor material with small bandgaps. Here, it is possible to regulate the absorption wavelength, hence modifying the dimensions (depth and width) of the QW [166]. The most important factor in determining quantum well-based designs is the inter-band recombination of carriers that leads to the highest modulation frequency. However, the recovery time must be kept to a minimum because it may affect the cavity's pulse dynamics [167].

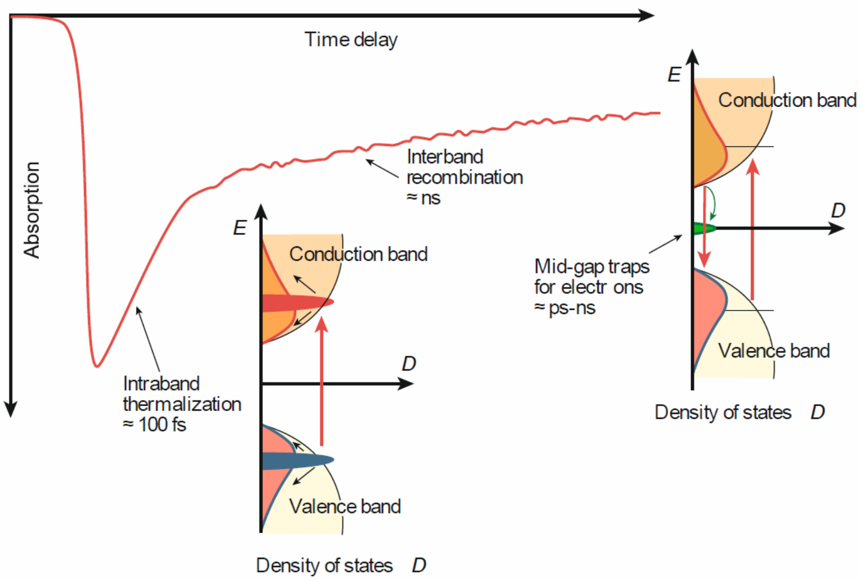

Fig. 3.5: SESAMs relaxation dynamics [164].

3.4.3 Active mode-locking

Fiber laser mode-locking can be achieved either active or passive [168]. Active ML, in which a modulator modulates the amplitude or phase of the laser cavity, necessitates an external signal to maintain mode locking. This extremely prevalent type of mode-locking involves an actively driven element in the laser cavity, modifying either the amplitude (AM mode-locking) or phase (FM mode-locking) of the travelling light. Amplitude or phase must be modulated with a frequency equal to or a harmonic of the mode spacing in order to achieve phase synchronization. Active mode-locking is comprehensible in both the temporal and frequency domains. Amplitude modulation of a sinusoidal signal produces modulation sidebands, as is widely known from AM radio transmission, for instance. If the modulation frequency is the same as mode spacing, modulation sidebands will overlap with adjacent modes, resulting in phase synchronization. In the time domain, the modulator tends to generate cavity losses. As the laser emits more light at loss minimum, this intensity difference will accrue over successive round trips, resulting in a mode-locked state until the laser reaches a stable level. More details are shown in figure 3.6.

The modulator's cavity loss can be expressed as:

$$\boldsymbol{\alpha = \alpha_c + \alpha_m[1 - \cos(\omega_m t)]} \qquad \textbf{Eq (3.22)}$$

where α_c is the regular cavity losses and α_m is the additional loss introduced the modulator and $\boldsymbol{\omega_m}$ is the frequency.

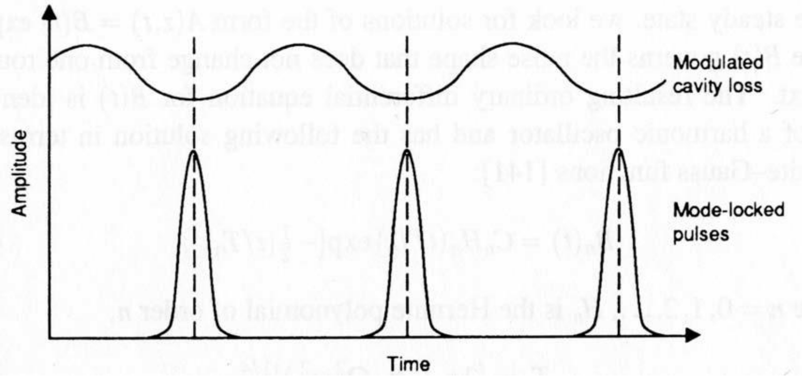

Fig. 3.6: Schematic Explanation of Active mode locking [159].

3.5 High repetition rate ultrashort pulsed fiber laser

In telecom applications, where high repetition rate lasers are commonly used, pulse width is often on the order of tens to hundreds of picoseconds. Furthermore, there are a number of additional applications where a high repetition rate is advantageous, but shorter pulses are required, and the requisite wavelength is outside the region where fast telecom lasers are readily available. The repetition rate of fiber lasers is often in the tens of megahertz (MHz) range. According to the following formula, reducing the length of the laser's cavity makes it more compact and leads to increasing the laser's repetition rate.

$$\boldsymbol{f = \frac{c}{2nL}} \qquad \text{for linear structure} \qquad \textbf{Eq (3.23)}$$

and

$$\boldsymbol{f = \frac{c}{nL}} \qquad \text{for ring structure} \qquad \textbf{Eq (3.24)}$$

where c is the speed of light, n is the effective refractive index of the cavity, and L is the length of the cavity.

The faster repetition rate facilitates the development of innovative technological solutions for a variety of applications. These include devices that monitor fast-moving processes, such as chemical reactions, which require a high repetition rate and short pulses. Reaching high repetition rate is not simple, but fiber lasers like the one proposed in this thesis make it possible. There are three well-established methods to increase the repetition rate of a mode-locked laser: reducing the cavity length, increasing the number of pulses in the cavity (known as harmonic mode locking), or employing a coupled-cavity architecture that also increases the number of pulses in the main cavity [169]. There are further circumstances where a high repetition rate is desired. There are also several applications at 1 μm which needs high repetition rate such as micromachining like drilling process that high speed of material processing is possible by high repetition rate. In two-photon microscopy, high repetition rates and high average powers permit a strong signal and a good signal-to-noise ratio. In nonlinear bioimaging techniques, such as two-photon fluorescence excitation (TPE) microscopy and SHG microscopy, short pulse lasers with a high repetition rate are two crucial factors. Generally, however, only a small portion of the available laser power can be given to the sample before significant photoinduced damage occurs [170]. A high repetition rate is also essential for minimizing photobleaching.

3.6 Optical properties

An ultrashort laser pulse is a tiny burst of electromagnetic energy classified by its electric field. In a pulsed laser, an electric field is the function of the pulse envelope and the sinusoidal carrier function in an ultrashort pulse, the pulse is defined by the amount of its time duration and spectral width. Prior to the development of ultrashort pulsed lasers, measuring the pulse width was one of the critical problems of laser characterization methods. However, these approaches have evolved in parallel with the development of ultrashort pulsed lasers. In early research, the most prevalent electronic detector approaches resolved only pulses in the picosecond range [95].

To ensure the laser's proper operation, the optical spectrum, autocorrelation, and electric pulse train from a photodiode of the pulse must be monitored. If too much energy is introduced into the cavity, the laser will respond by multiple pulsing (doubling, tripling, etc.). It means that two pulses are circulating in the cavity with half the repetition period (period doubling), or two pulses coupled and separated by a few picoseconds, and it will show on the autocorrelation trace and oscilloscope trace. Normally, amplitude and phase noise are measured utilizing the electrical pulse train generated by an optical pulse train incident on a photodetector. The rising time and duration of the electrical pulses are determined by the photodetector's characteristics.

3.6.1 Optical spectrum

The optical spectrum contains information regarding the optical energy distribution of a light beam at various wavelengths, which is usually measured with an optical spectrum analyzer (OSA). In addition to high-precision qualities for determining the optical spectrum, these devices also offer extensive analytical options. Such general applications suit the many laboratory requirements, such as extensive wavelength ranges, the applicability of ranging photodiodes, varying resolution bandwidths, the capability of single and multiple wavelength sweeps, and variable sweep rates. Depending on the source being studied, the input light may be injected in various ways. Numerous optical spectrum analyzers have a fiber-optic input, typically with fiber connectors, as well as an optical input in free space. In an optical domain diagram, spectral elements such as spectral intensity, radiance, and flux as a function of frequency or wavelength are displayed. Usually, the optical spectrum of the beam is provided on a calibrated or uncalibrated arbitrary logarithmic scale. In addition, when the laser is operated under the continuous wave regime, the spectrum line width is defined by a thin spectral line, whereas a wider spectral line reveals the laser's ultrashort pulsed mode-locked operation [171].

3.6.2 Autocorrelation

Autocorrelation is one of the earliest and most widely used method for characterizing optical pulses. The approach is used to determine the temporal structure of ultrashort pulses, including pulse duration and phase modulations [172]. A beam splitter is used to divide the incoming beam with an electric field E(t) into two beams with the same power. One pulse is purposefully delayed relative to the other by sending one beam over a delay line with a temporal delay of τ. Then, these two copies are spatially superimposed in a nonlinear optical medium to create a mixture. This medium is a crystal for generating second harmonic generation, that creates light with twice the input pulse frequency (Half at the wavelength) [173]. As depicted in figure 3.7, due to the temporal overlap of these two pulses, only the intensity component is generated, and this is permitted to pass past the iris to the detector. By recording the average power as a function of the relative delay between two repeated beams, the intensity autocorrelation of the laser pulse is attained [133]. Due to the simplicity of this methodology's underlying idea, autocorrelation has become the most used technique for characterizing ultrashort pulses. When considering lasers with a pulse duration below the femtosecond regime, it is still possible to identify a few limits for these devices. Additionally, the autocorrelation does not provide any information regarding the phase relationship between pulses and pulse shape, which is more important for comprehending the behavior. The FROG and SPIDER pulse characterization techniques are favored.

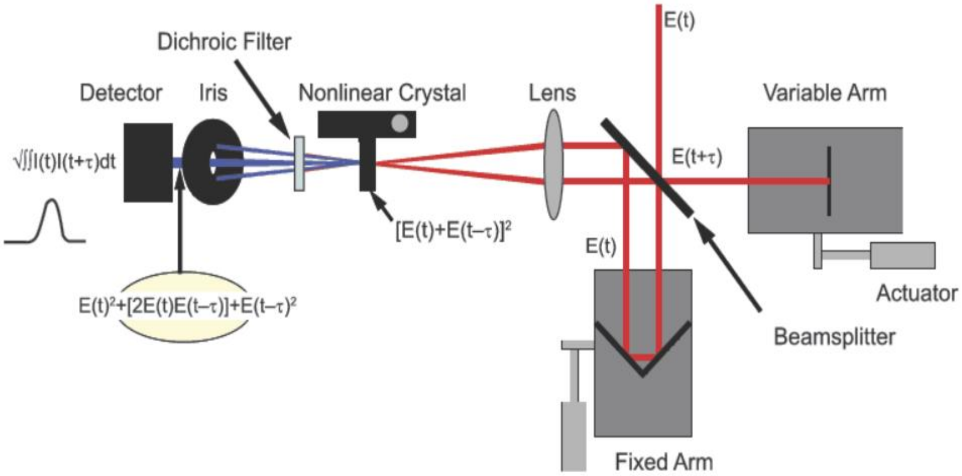

Fig. 3.7: Structure of a typical autocorrelator [174].

3.6.3 Radio frequency Spectrum

Radio frequency (RF) spectrum is known as one of the standard approaches for pulse characterization among the methods currently in use. A special form of spectrum analyzer known as a series analyzer is utilized to monitor and record the measurements. To conduct RF spectrum measurements, two fundamental concepts must be understood: signal-to-noise ratio (SNR) and line width. The SNR parameter establishes the ratio of signal power to noise power (usually expressed in decibels (dB)) between the desired correct signal and the background noise. A higher signal-to-noise ratio is required for an RF estimation to be relatively accurate with respect to the specification. When both the signal and noise levels are measured in decibels (dB), the SNR can be determined by subtracting the noise level from the signal level. In addition, the lowest acceptable SNR parameter value is 20 dB, while values greater than 41 dB are regarded as outstanding.

Chapter 4: Experimental setup and results

4.1 Linear cavity SESAM-based laser

As previously noted, (3.4.2), ultrashort pulses have been reliably generated by passively mode-locked lasers designed with SESAM. In general, the structure of a laser cavity is straightforward, and its configuration can be either ring or linear. Stable mode-lock operation is investigated and realized at variable net cavity group velocity dispersion [142]. In this section, an experimental investigation of SESAM-based linear laser cavity, passive mode-locking is discussed and verified experimentally to generate ultrashort pulsed fiber laser working at 1064 nm wavelength region.

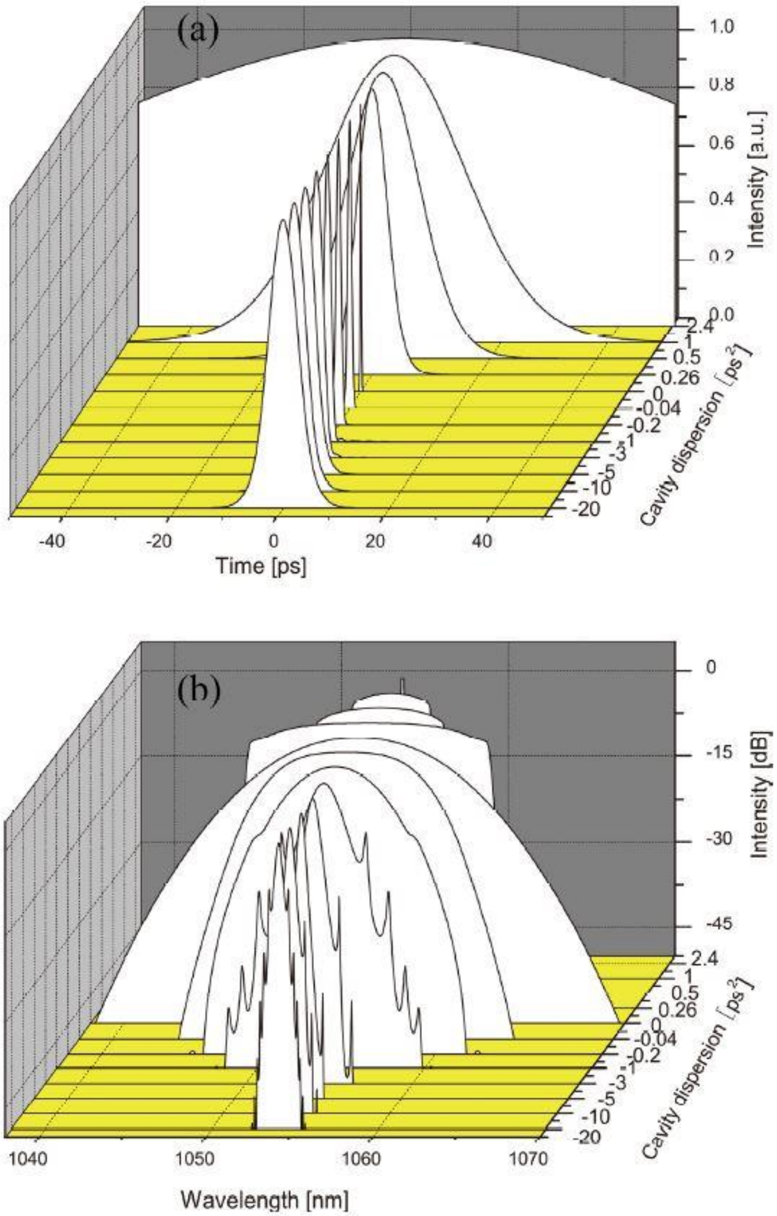

Fig. 4.1: (a) Simulation of mode-locked pulse trains with various cavity dispersion. (b) Simulation of output spectrum of mode-locked fiber laser with varying cavity dispersion [175].

Figures 4.1(a) and 4.1(b) depict the modelling of the mode-locked laser's spectra and pulse forms when the total net dispersion is changed inside the cavity. When the cavity's dispersion increases in the negative dispersion region, the spectra exhibit sidebands caused by interference between the soliton and dispersive waves, and the simulated spectral bandwidth increases. When the net cavity dispersion approaches zero, the spectrum achieves its maximum with a Gaussian profile and the pulse width reaches its minimum; these are characteristics of typical dispersion-managed solitons. When the net cavity dispersion increases in the dispersion cavity's positive region, the laser spectrum displays sharp edges. As the spectral spectrum decreases, the pulse width correspondingly increases. When the cavity dispersion increases, it becomes more challenging to arrive at a stable solution. When the net cavity dispersion is large, the saturable absorber’s parameters must be chosen properly to obtain stable mode-locking [175].

4.1.1 Seed Laser

Mode-locked Ytterbium-doped fiber laser (YDFL) using a uniform FBG and commercial SESAM in a linear structure cavity is generated. The experimental setup for the seed is shown in figure 4.2.

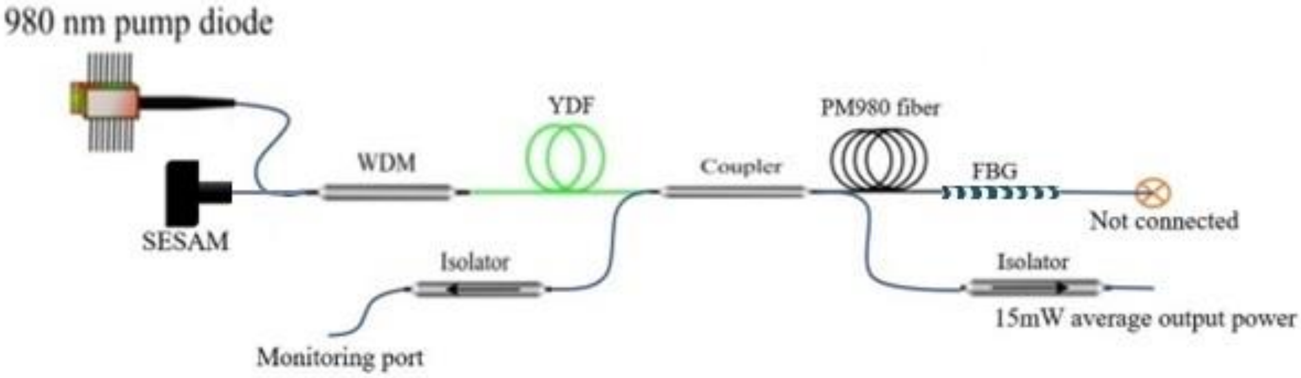

Fig. 4.2: experimental setup for seed.

The SESAM which guarantees the self-starting and stable mode-locking is connected to the signal port of the WDM and the pump light emitting at 976 nm is launched into linear cavity by splicing to the pump port of the WDM. A piece of Yb-doped PM fiber with a core absorption at 976 nm as a gain medium is connected to the common port of the WDM. At the end of the active fiber, a coupler separates the signal, and the main output of the coupler is utilized for the FBG and the free fiber termination at the end of the FBG is angle-cleaved to reduce undesired reflections. The uniform FBG is written within a PM fiber's core. The FBG has a high reflectance, centered at 1064 nm with the narrow spectral bandwidth of. Two PM isolators are connected to the coupler's output to guarantee unidirectional light transmission and avoid any back reflection to the main seed. Using an optical spectrum analyzer, a 40 GSA/s oscilloscope, and a single photodetector, the spectrum and pulse train of the mode-locked laser are measured concurrently. The fiber laser's radio frequency spectrum is monitored using a spectrum analyzer. The repetition rate of 42 MHz is achieved which according to the equation (3.23) is in well agreement with the cavity length as the pulse train is shown in figure 4.3.a. The autocorrelation trace of the generated pulse is measured about 10ps full width half maximum (FWHM) using FR-103 WS Autocorrelator, as illustrated in figure 4.3.b. The laser obtained an exceptional signal-to-noise ratio of 90 dB, as depicted in figure 4.3.c and the laser emission spectrum is shown in figure 4.3.d. The center wavelength at 1064 nm with a 3 dB bandwidth of 0.2 nm. In addition, the average output power of about 15 mW is achieved at the seed's output.

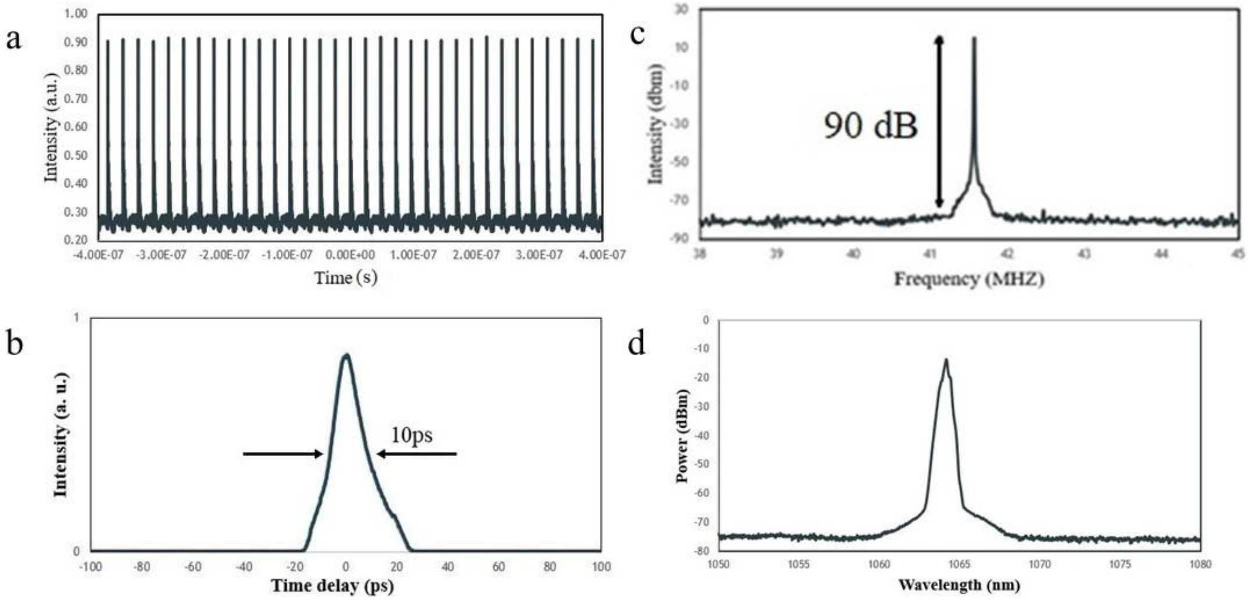

Fig. 4.3: a) pulse train over time. b) Autocorrelation measurement of the pulse after seed. C) RF spectrum over a frequency span of 7MHz. d) Optical spectrum for seed.

4.1.2 Pre-amplifier Stages

Between the seed laser and the power amplifier stage, two stage pre-amplifiers are employed. At the first pre-amplifier stage, the seed output is connected to the signal port of the WDM and the same laser diode as the seed is spliced to the pump port of the WDM. A piece of same Yb-doped PM fiber as used in the seed part is connected to the common port of the WDM. The end of the active fiber is connected to the first port of the PM circulator. The second port of the circulator is spliced to the PM chirped FBG and the free fiber termination at the end of the PM-CFBG is angle-cleaved to reduce undesired reflections. The PM-CFBG is used to filter the unwanted spectrum such as amplification spontaneous emissions (ASE). This PM-CFBG has a high reflectance, centered at 1064 nm. At the last, the third port of the circulator is used as an output of first pre-amplifier stage. Figure 4.4 describes the schematic of the first stage single mode amplification.

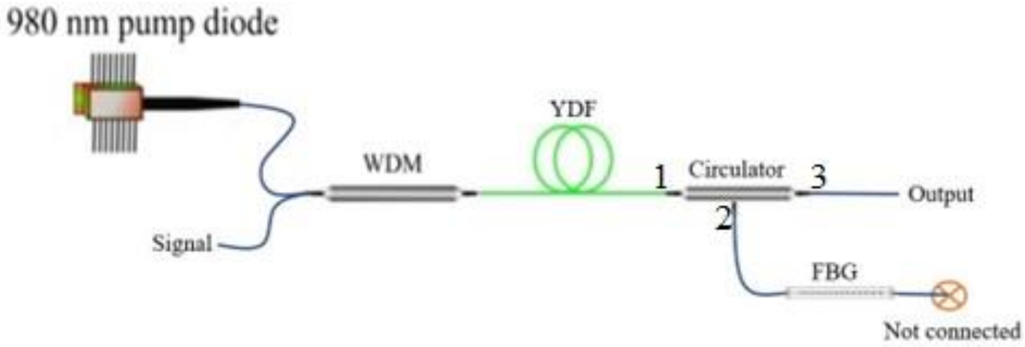

Fig. 4.4: Experimental setup for first pre-amplification stage using CFBG.

At the second pre-amplifier stage, the first pre-amplifier's output is connected to the signal port of the WDM, and the same laser diode as last two stages is spliced to the pump port of the WDM. A piece of same Yb-doped PM fiber, used in the last two parts, is connected to the common port of the WDM. The end of the active fiber is connected to the high-power isolator and the other side of the isolator used as an output port for this stage. The experimental setup for the second pre-amplification stage is shown in figure 4.5.

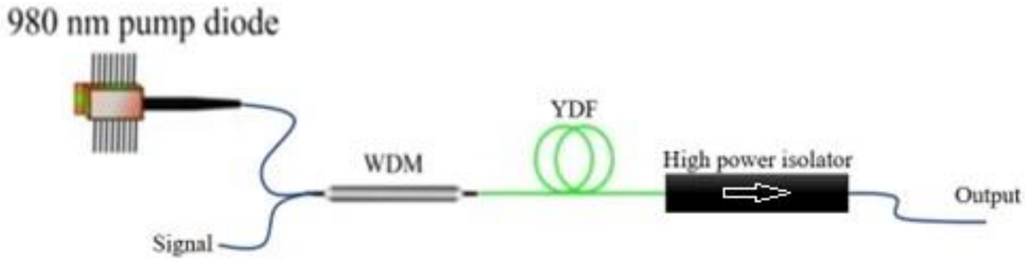

Fig. 4.5: Experimental setup for second pre-amplification stage.

The results of these two stage amplifications are as follows:

1- Increase the output power of the seed source to 20 and 130 mW after first and second stage single mode amplification respectively.
2- The spectral bandwidth of the laser is increased to 0.5 nm and more than 1 nm after each first and second stage pre-amplification due to the SPM, as shown in figure 4.6.a and 4.6.b.
3- Filtering the unwanted spectrum such as amplification spontaneous emissions (ASE).

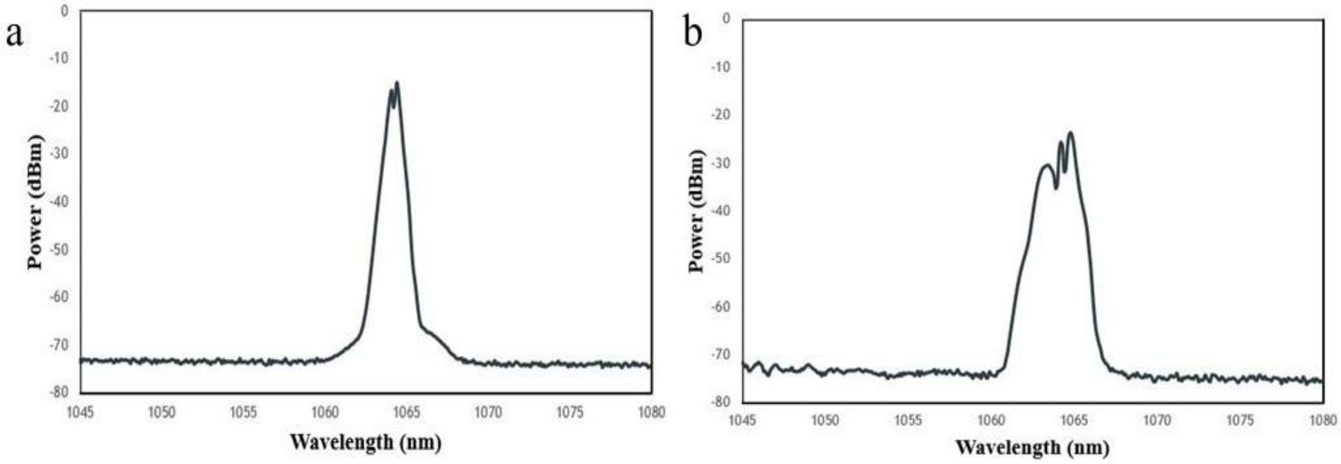

Fig. 4.6: a) Optical spectrum increased to the approximate amount of 0.5nm after the first preamplification stage. b) Optical spectrum increased to more than 1nm after second preamplification stage.

4.1.3 Power (Post) Amplifier Stage

The system's final amplification step is the power amplifier which its setup shown in figure 4.7. At this stage the output, coming from the pre-amplifications, is connected to the signal port of the combiner. Two, 980 nm multimode pumps are spliced to the pumps port of combiner to amplify the average input signal power from 130 mW to more than 10 W after the post-amplification stage. The output of combiner is connected to piece of Yb-doped large mode area fiber and then, passive large mode area fiber respectively. After that the pump stripper is built on the passive double clad fiber to remove the excess pump power. Finally, the output is connected to a collimator to collimate the light with beam diameter of 1.5 mm.

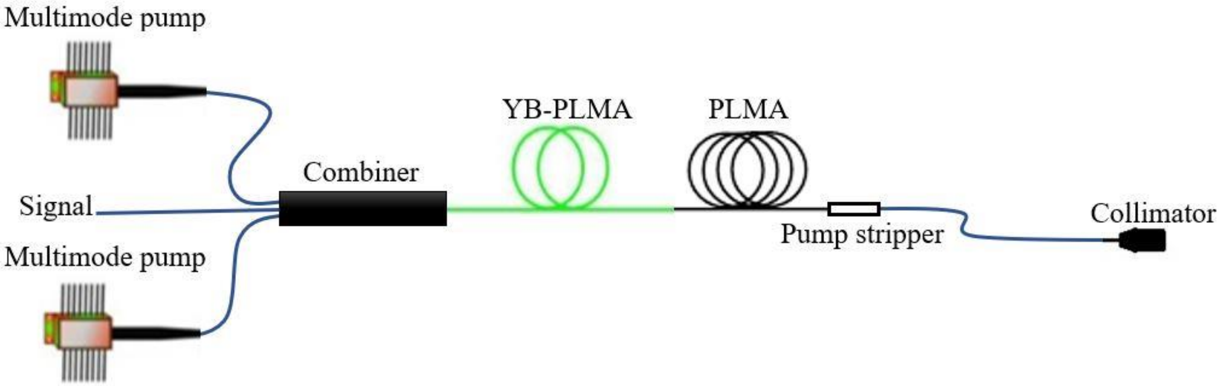

Fig. 4.7: Experimental setup for power amplification stage.

Since the peak power of the pulse in the post-amplifier is high, SPM is occurring and leading broadening of the bandwidth to about 20nm, as shown in figure 4.8.

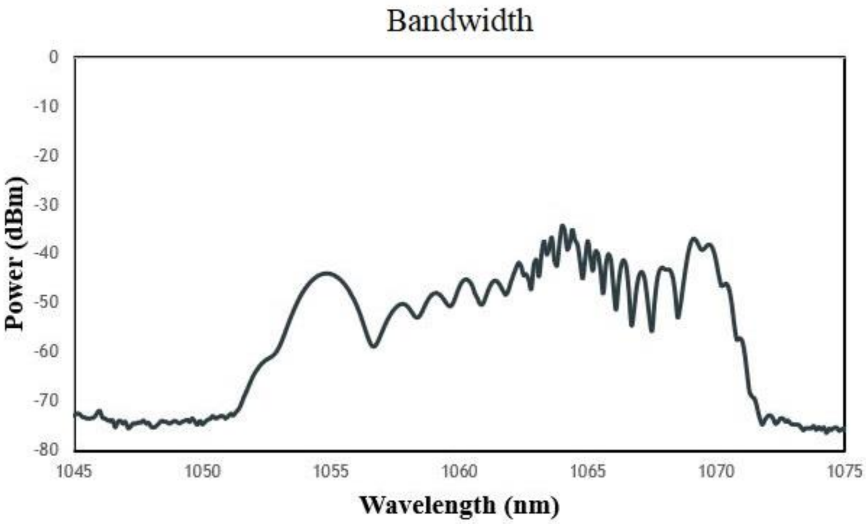

Fig. 4.8: Optical spectrum after power preamplification stage.

4.2 Grating pulse compressor

Pulse compression is an effective method that benefits from correlation between the pulse width and its optical spectrum. It is possible to amplify pulses beyond the conventional damage threshold limits which are imposed by the optical components of the laser system. It is feasible to reduce the pulse width by applying dispersion at the opposite side, which is also known as negative dispersion, to obtain the shortest pulses after dispersive propagation. This would bring the pulses to their smallest possible length. Because most materials at the 1 µm spectral region exhibit positive dispersion, it is typically necessary to employ alternative methods to apply negative dispersion. In order to satisfy this objective, one of the most frequently used methods is to use grating pairs. Compared to other techniques for achieving negative dispersion, such as using prisms, gratings can achieve significantly higher levels of negative dispersion in less space than those other techniques. Negative dispersion is achieved by a grating pair in its most fundamental form because different wavelengths travel different paths. This is due to longer wavelengths having higher speeds during their propagation. Therefore, longer wavelengths need to travel longer path compared to the lower wavelength to compress the pulse as shown in figure 4.9(a). The incident pulse on a diffraction grating diffracts spatially and different wavelengths diffract with different angles according to their wavelength. The pulse's trailing section (shorter wavelengths) diffracts at a lower angle and is directed toward the leading edge of the second grating as shown in figure 4.9(b). When the light diffracts from the second grating, which is aligned parallel to the first grating, the distinct parts of the pulse (with their correspondingly varying wavelengths) diffract at angles that produce a pulse whose parts are almost synchronized in time. Since the overall energy of the laser remain at the same level, the Peak power will increase significantly [176].

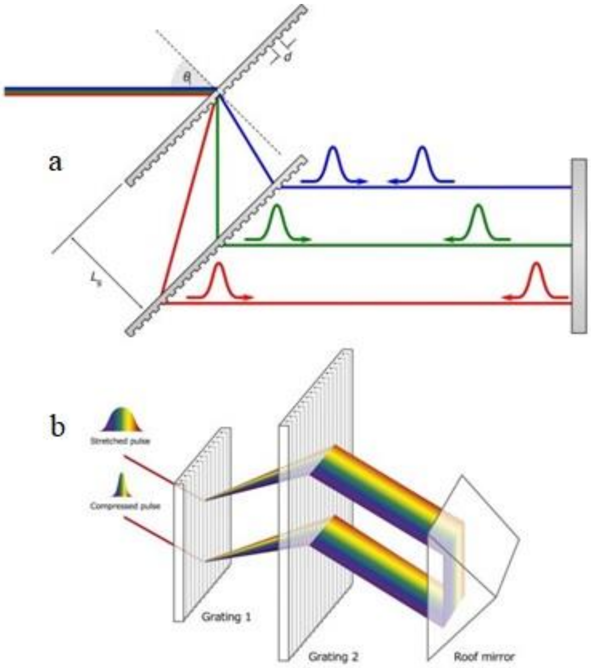

Fig. 4.9: Schematic of pulse compression with a pair of parallel diffraction gratings [177].

As mentioned in 3.4 using the time-bandwidth product relation mentioned in equation (3.13), it is possible to calculate the maximum amount of compressing (Minimum pulse width that can achieve) for a chirped pulse. Then using the final and primary amount of pulse width it is possible to calculate how much dispersion is needed to compensate the pulse chirp as follows:

$$\boldsymbol{\tau_{out} = \tau_{in} \times \sqrt{1 + \left(\frac{4ln2\varphi_2}{\tau_{in}^2}\right)^2}} \qquad \text{which} \qquad \boldsymbol{\tau_{out} > \tau_{in}} \qquad \textbf{Eq (4.1)}$$

and

$$\boldsymbol{\varphi_2 = \frac{1}{4(ln2)} \times \sqrt{\left(\frac{c_B\Delta t_{out}}{\Delta v}\right)^2 - \left(\frac{c_B}{\Delta v}\right)^4}} \qquad \text{which} \qquad \boldsymbol{\Delta v = \frac{c\Delta\lambda}{\lambda^2}} \qquad \textbf{Eq (4.2)}$$

By having the gratings angle of incidence (θ_i), grating line density (d), amount of dispersion (φ_2) and of course the wavelength (λ) it is possible to calculate the GDD and TOD dispersion of a double pass grating pair compressor.

$$\boldsymbol{GDD = -\frac{Nm^2L\lambda^3}{2\pi c^2d^2} \times \left[1 - \left(-m\frac{\lambda}{d} - \sin(\theta_i)\right)^2\right]^{-\frac{3}{2}}} \qquad \textbf{Eq (4.3)}$$

$$\boldsymbol{TOD} = -\frac{\mathbf{3}\boldsymbol{\lambda}}{\mathbf{2}\boldsymbol{\pi c}} \times \frac{\mathbf{1}+\frac{\boldsymbol{\lambda}}{\boldsymbol{d}}\mathbf{sin}\,\boldsymbol{\theta_i}-\mathbf{sin}^2\,\boldsymbol{\theta_i}}{\mathbf{1}-(\frac{\boldsymbol{\lambda}}{\boldsymbol{d}}-\mathbf{sin}\,\boldsymbol{\theta_i})^2} \times \boldsymbol{GDD} \qquad \textbf{Eq (4.4)}$$

where N is the number of passes, m is the diffraction order, λ is the center wavelength, d is the grating period, which is equal to inverse of the line density, L is the distance between two gratings, and θ_i is the incidence angle. According to the equation (4.3) the distance between the pair of grating calculated as:

$$\boldsymbol{L} = -\sqrt{\left[\mathbf{1}-(-\boldsymbol{m}\frac{\boldsymbol{\lambda}}{\boldsymbol{d}}-\mathbf{sin}(\boldsymbol{\theta_i}))^2\right]^3} \times \frac{\mathbf{2}\boldsymbol{\pi c}^2\boldsymbol{d}^2}{\boldsymbol{N m}^2\boldsymbol{\lambda}^3} \times \boldsymbol{GDD} \qquad \textbf{Eq (4.5)}$$

The Littrow angle (θ_L), which is the incidence angle optimal for maximum diffraction efficiency in blazed transmission gratings is calculated as:

$$\boldsymbol{\theta_L} = \mathbf{arcsin}(\frac{\boldsymbol{\lambda}}{\mathbf{2}\boldsymbol{d}}) \qquad \textbf{Eq (4.5)}$$

Also, θ_D is the angle of diffraction and can be define as:

$$\boldsymbol{\theta_D} = \mathbf{arcsin}(\mathbf{sin}\,\boldsymbol{\theta_i} + \boldsymbol{m}\frac{\boldsymbol{\lambda}}{\boldsymbol{d}}) \qquad \textbf{Eq (4.6)}$$

Therefore, the initial pulse width of 10ps is compressed to 200fs in the pulse compression section. The autocorrelator trace of compressed pulse using transmission grating pair is depicted in figure 4.10.

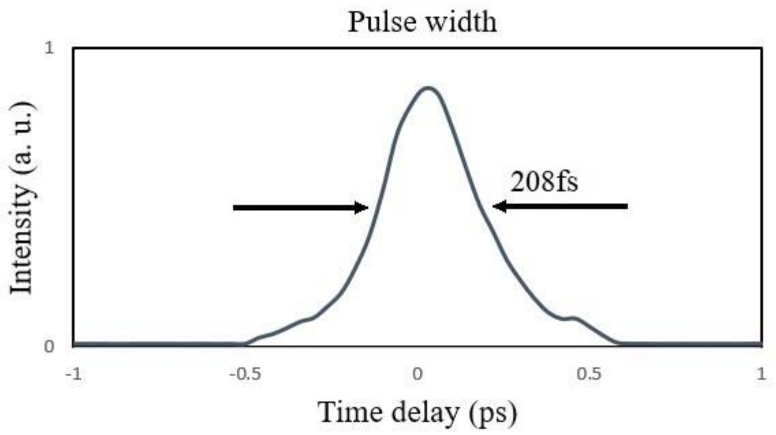

Fig. 4.10: Autocorrelation trace of the pulse after compressor part.

Since the insertion loss of each transmission grating is about 6% as depicted in figure 4.11, the total loss of about 24% is expected due to four times passing the beam through the gratings in the compressor and consequently the average output power drops from 10W to 7W.

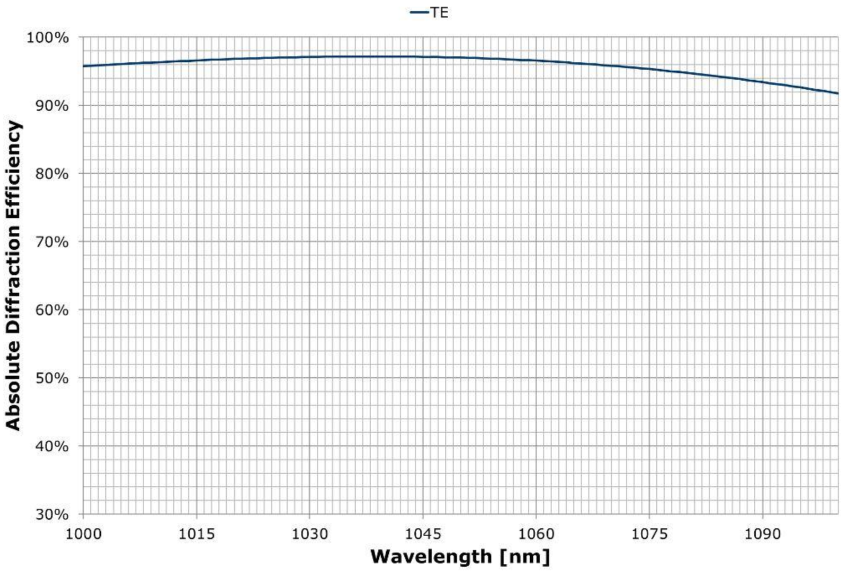

Fig. 4.11: Transmission gratings performance diagram [178].

4.3 Optical power

If the right parameters are known, it is not difficult to compute the power or energy of optical pulses. When working with laser pulses and power or energy meters, it is often necessary to understand the relationships between several fundamental quantities. Take into consideration a train of optical pulses that occurs at regular intervals and has a repetition rate of $f = \frac{1}{T}$, as illustrated in figure 4.12.

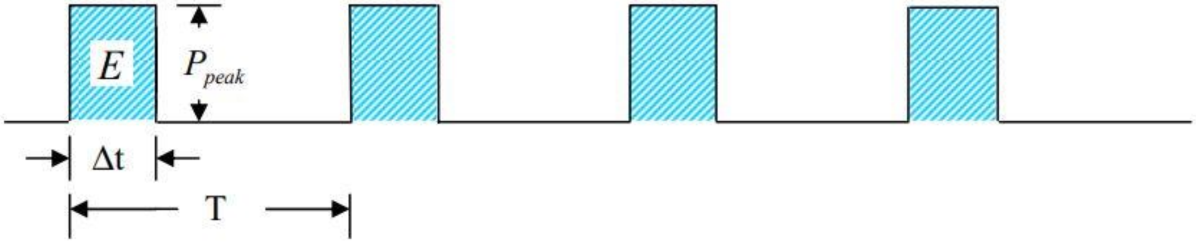

Fig. 4.12: The schematic of pulse train with constant repetition rate [179].

There are two completely distinct definitions of the term optical power that can be found in scientific literature.

1- Peak power is the rate of energy flow in every pulse. The maximal optical power that occurs during a light pulse is referred to as the pulse's peak power. As a result of the relatively short pulse durations that may be achieved with optical pulses, peak powers can reach very high levels even when the pulse energies are just moderate. The peak power can be expressed as:

$$\boldsymbol{P_{peak} = \frac{E}{\Delta t}} \qquad \textbf{Eq (4.7)}$$

where E is the energy, and Δt is the pulse duration.

2- Average power, which is rate of energy flow averaged over one full period.

$$\boldsymbol{P_{avg} = \frac{E}{T} = Ef} \qquad \textbf{Eq (4.8)}$$

where f is the repetition rate and T is one full period.

The equation (4.9) is driven utilizing equation (4.7) and (4.8).

$$\boldsymbol{P_{peak} \times \Delta t = P_{avg} \times T} \qquad \textbf{Eq (4.9)}$$

Duty cycle is the fractional amount of time that the laser is "on" during any period, and it expressed by:

$$\boldsymbol{D = \frac{P_{avg}}{P_{peak}} = \frac{\Delta t}{T}} \qquad \textbf{Eq (4.10)}$$

Therefore, the peak power of a pulse can be easily calculated if the average power and the duty cycle are known:

$$\boldsymbol{P_{peak} = \frac{P_{avg}}{\textbf{Duty Cycle}}} \qquad \textbf{Eq (4.11)}$$

As a result, for this part, according to the above equations, the 166.67 nJ and 797448 W are calculated as laser energy and pulse peak power respectively for the laser in this work. In addition, the power stability diagrams are shown in figure 4.13 for the seed laser and final free space output respectively.

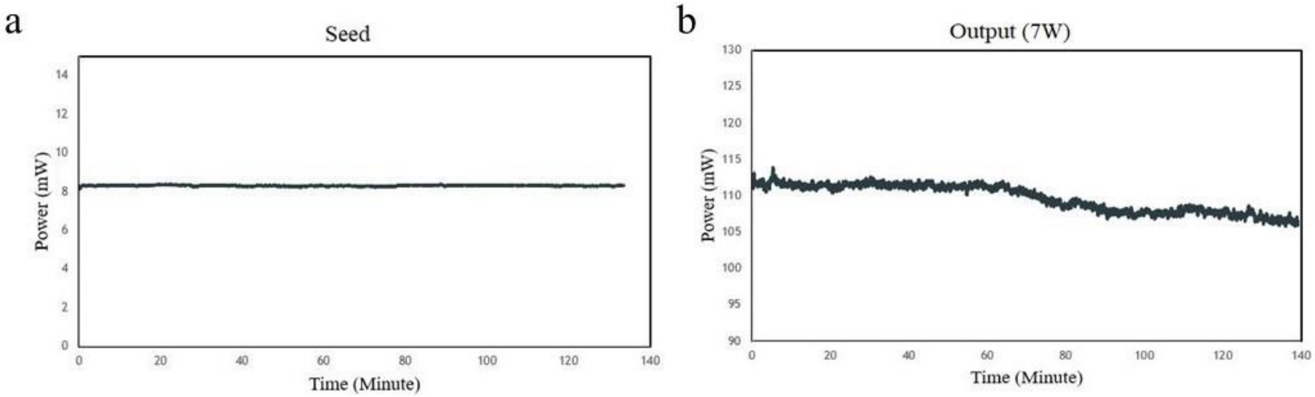

Fig. 4.13: a) Average output-power stability more than two hours for the seed using an attenuator. b) Average output-power stability more than two hours for the final laser output using an attenuator.

4.4 Laser Beam Profile

The beam quality is one of the most significant parameters to consider for Gaussian beams. It is independent of the wavelength and its quantitative factor called M^2. It shows that, how close the beam is to the fundamental mode $TEM00$, Gaussian beam. It defines the minimum beam spot size and beam divergence.

The beam divergence is the angular measure of the beam's spreading as it moves away from its source. It is especially applicable in the far distance. The laser's output light is restricted in the form of a small cone; however, at long distances, it spreads out gradually. Divergence is the angular measurement of the increase in diameter with increasing distance from an optical source.

Beam profile is the representation of the intensity profile at a given place along the beam's path. Flat top profiles and Gaussian beam profiles are the two most popular types for beam profile. The beam profile determines the energy density, the light's concentration, and light's collimation.

High-resolution two-dimension (2D) and three-dimension (3D) beam profiles can be presented together. Important beam profile parameters including intensity, beam diameter, and peak density can be monitored rapidly. Figure 4.14 shows an image of the input beam. On the left side the vertical and horizontal profile of the beam are displayed and both have a Gaussian profile distribution. The window on the right shows a 2D of the beam profile which red represents the highest intensity while purple is the lowest. On the other hand, the power measurement of 132 mW and beam widths of 1.69 mm × 1.69 mm in directions x and y can be observed by the analyzer.

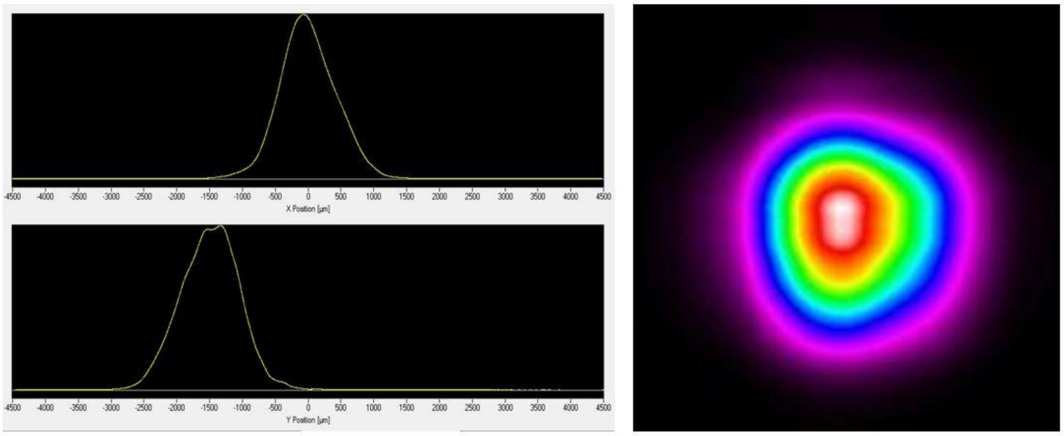

Fig. 4.14: Beam profile of laser output.

4.5 Pulse-to-pulse (p2p) stability

Stability measurement of ultrashort optical pulses in real-time is crucial for various applications such as frequency comb generation, arbitrary optical waveform generation, timing and frequency distribution by optical fiber links and especially wide-field second harmonic generation microscopy using a high-power (more than 4 W) and high-repetition-rate (in the range of MHz) laser oscillator to achieve high-speed imaging over a large area [180, 181].

The laser output beam was collimated to measure the shot-to-shot power fluctuations of this pulsed fiber laser. Pulse-to-pulse fluctuations were measured using the method provided in reference [182]. Since the energy of pulses is related to their peak power, rogue events and their associated characteristics can be captured through a measurement of pulse energy from shot to shot. In our trials, this was accomplished utilizing a photodiode and a 40 GSA/s analogue oscilloscope. This apparatus offers a measurement of the average energy of each pulse in our experiments. This enables for the characterization of power density fluctuations. To quantify the oscillations of spectral power density, histograms were plotted across one million pulses acquisitions with the same photodiode signal amplitude and trigger level for each measurement. As linear detection was used, there were no saturation effects. The proportion of shot-to-shot fluctuations was calculated using equation 4.12, where V_{max} and V_{min} represent the maximum and minimum photodiode signal amplitudes.

$$\frac{\boldsymbol{V_{max} - V_{min}}}{\boldsymbol{V_{max} + V_{min}}} \times \mathbf{100} \qquad \textbf{Eq (4.12)}$$

First the power is reduced by sending the beam through the polarizer and half wave-plate to prevent any damaging to the photodetector. Figure 4.15 shows one sample of pulse for the seed and output beam, which are displayed on the screen of oscilloscope. As a result of this part, the P2P stability of about 2.4 and 3.4 percent are realized for the seed and output of 1064 nm mode locked fiber laser respectively.

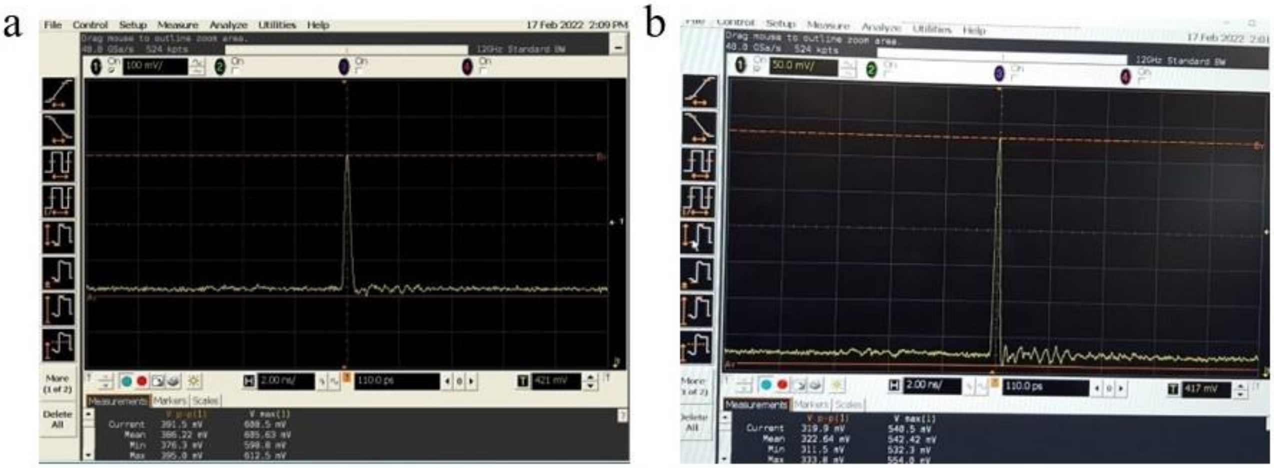

```
          V p-p(1)     V max(1)
Current   391.5 mV     608.5 mV
   Mean   386.22 mV    605.63 mV
    Min   376.3 mV     598.0 mV
    Max   395.0 mV     612.5 mV
```

```
          V p-p(1)     V max(1)
Current   319.9 mV     540.5 mV
   Mean   322.64 mV    542.42 mV
    Min   311.5 mV     532.3 mV
    Max   333.8 mV     554.0 mV
```

Fig. 4.15: a) Minimum and maximum pulse amplitude measurement of the pulse trin over time slot for seed. b) Minimum and maximum pulse amplitude measurement of the pulse trin over time slot for output beam.

To quantify the results, corresponding histograms plotted over 1,000,000 acquisitions are plotted in figure 4.16 for the seed and final output beam.

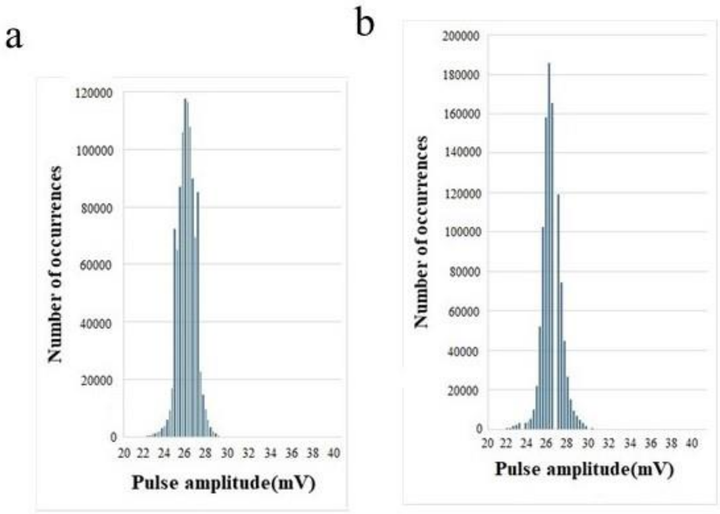

Fig. 4.16: a) Corresponding histograms displaying the number of occurrences as a function of amplitude signal pulses at 1064nm (from top to bottom) for seed. b) Corresponding histograms displaying the number of occurrences as a function of amplitude signal pulses at 1064nm (from top to bottom) for final output beam.

4.6 SESAMs calculations

The SESAM's structure and operation have already been discussed in the third chapter. However, there are several essential concepts that need to be considered when dealing with them. These concepts are explained in this section of the thesis and help to choose the right SESAM for generating stable mode-locking.

4.6.1 Modulation depth

The modulation depth is the maximum change in reflectance or absorption that can be generated by incident light of a particular wavelength in the context of saturable absorbers used for passive mode locking of lasers. This is a crucial design parameter for lasers that are passively mode locked. Large modulation depth provides very good pulse shaping by the saturable absorber, which can result in a short pulse length and dependable self-starting. For SESAMs, the modulation depth is defined as the largest change in reflectance caused by light (ΔR) and may rely heavily on the operation wavelength. Typically, it is on the order of 1% for mode-locked bulk lasers, whereas significantly greater values (on the order of 10%) are required for mode-locked fiber lasers. The obtained modulation depth is a significant portion of the unsaturated reflectance loss caused by the integrated absorber. It can be raised by utilizing a thicker absorber or several thin absorbers. It is dependent on the absorber's thickness as well as the material, the wavelength of the light, and the absorber's structure's optical field penetration.[183]

4.6.2 Saturation fluence

The saturation fluence (F_{sat}) depends on the optical design of the SAM and the type of the material which is used in semiconductors. The advantage of low saturation fluence is that laser mode-locking can be initiated at low power levels. This prevents fast absorber degradation. In order to minimize the saturation fluence, the thickness of the semiconductor absorber layer is decreased to less than 10 nm. A quantization of the electron energy and the momentum in the perpendicular direction to the absorber layers occur and lead to decrease the states density to smaller value of a compact semiconductor. The absorber layers in a SAM consist of tiny quantum wells with a lower band gap than the side barriers. Rather than employing a thick absorber layer, the number of quantum wells is raised, when a higher SAM absorption value is required. The intensity of electric field in front of the SAMs Bragg mirror is a periodic function of nodes and antinodes. In order to achieve a low saturation fluence, the absorbing quantum wells are placed close to the antinodes. In conjunction with the Fresnel reflection at the semiconductor-air interface, the Bragg mirror makes a Fabry-Perot like resonator that includes quantum wells. The resonant or anti-resonant nature of the cavity is determined by the optical thickness of the semiconductor material that lies between the reflectors. Because of the enhanced field inside the cavity, the saturation fluence of a resonant SAM is lower than that of an anti-resonant SAM. This is because of the SAM's resonant mode. Usually, saturation fluence for resonant and anti-resonant SAMs, are $F_{sat} \sim 30\ \mu J/cm^2$ and $F_{sat} \sim 120\ \mu J/cm^2$ respectively [184].

4.6.3 Recovery time

Recovery time, also known as relaxation time, is the exponential time constant of absorption recovery following a saturated pulse. The relaxation time τ of SAMs typically ranges between 500 fs and 30 ps. The recovery time is significantly affected by the defect density of the absorber, and possibly surrounding structures. The layer of saturable absorber is composed of a semiconductor material with a direct band gap that is somewhat less than the photon energy of the laser beam. In the absorber film, electron-hole pairs are generated because of photon absorption. For laser mode-locking, the carrier relaxation period shall be slightly longer than the pulse duration. [179]

4.6.4 SESAM parameters for pulse durations

Typical reflectivity of fluence-dependent SESAM is illustrated in Fig. 4.17. For mode locking in the high-power and short-pulse regime, a high value of saturation fluence F_{sat} (hundreds of J/cm2) is often preferred so that, less sensitive resonator designs can operate with reasonably tiny laser spot diameters. Furthermore, about 1% of moderate modulation depth ΔR is usually used for one gain path per roundtrip. To generate the shorter pulses, the moderate to short recovery time 1/e (< 20ps) is required. For minimal thermal impacts, the non-saturable loss ΔR_{ns} should be kept as low as possible. The "rollover" of reflectivity is defined as the fluence F_0 when, the saturated reflectivity reaches its maximum value. The rollover should be shifted to high fluences to prevent multiple pulsing instabilities.

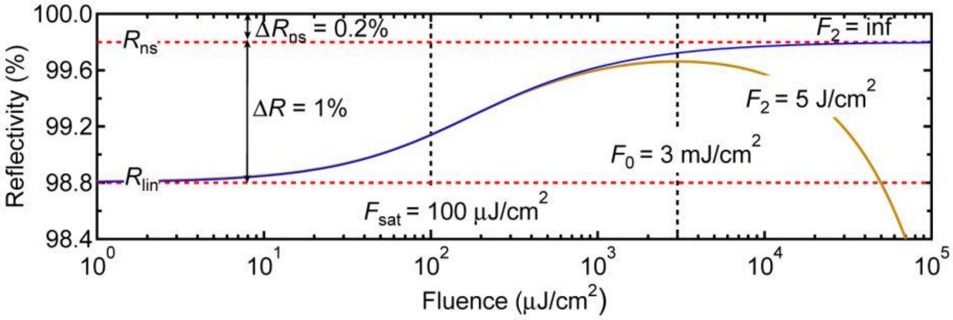

Fig. 4.17: Example of a typical nonlinear reflectivity curve for SESAM, illustrating all pertinent saturation factors. The F_0 represents the fluence when the reflectivity achieves to the highest level. In case of infinite F_2, no rollover can be seen and F_0 is also infinite [185].

The F_2 factor defines the inverse saturable absorption observed in the high-fluence region, to characterize the strength of the reflectivity rollover [186]. In the femtosecond regime, the inverse saturable absorption is dominated by two photon absorption (TPA) and F_2 is expressed by [187]:

$$F_2 = \frac{\tau_P}{0.585 \int \beta_{TPA}(Z) n^2(Z) |E(Z)|^4 dz} \qquad \textbf{Eq (4.13)}$$

Where, z is the vertical location in the epitaxial layer stack, n(z) is the refractive index, E(z) is the normalized electric field in the structure, $\beta_{TPA}(z)$ is the material dependent TPA coefficient and τ_p is the duration of the pulse. Based on the equation 4.13, shorter pulses decreased F_2 coefficient at the same pulse fluence and lead to an earlier rollover effect of the SESAM. Then, this is a crucial factor for generating the shorter pulses.

Thermal effects do not have an impact on performance, if the SESAMs are not operated deep in the reflectivity rollover. Performance can also benefit from the thin SESAM structure in combination with large laser spot sizes to avoid high heating flow. In this regime, it is possible to scale the power by increasing the laser cavity mode size on the SESAM, which maintains a constant saturation level.

Our SESAM was chosen properly to establish mode-locking in short pulse. SESAMs that will be able to generate shorter pulses (less than 300 fs) will need to have a more demanding set of parameters and for using SESAMs in high average power regime, SESAMs require to have a greater saturation fluence, a rollover that is moved towards higher fluence, a higher damage threshold, and lower non-saturable losses. Shorter pulses need fast recovery times (few picoseconds) [188, 189], low TPA and a large ΔR (>1%) [190, 191].

There is another important parameter for SESAMs called, SESAMs reflectance. There is no transmission in the stop band of the Bragg mirror and as a result, the formula for calculating reflectance is R = 1 - A. For the two-photon absorption with the recovery time of much less than the pulse duration, the SAM reflectance R can be calculated by:

$$R(F) = R_{ns}\frac{\ln\left(1+\left(\frac{R_{lin}}{R_{ns}}\right)\left(e^{\frac{F}{F_{sat}}}-1\right)\right)}{F/F_{sat}}e^{-F/F_2} \qquad \textbf{Eq (4.14)}$$

Where, R_{lin} and R_{ns} are constant, F is pulse fluence, F_{sat} is saturation fluence. [192]

Fluence F_0, at which maximum reflectivity is achieved is another key characteristic that can be retrieved from the nonlinear reflectivity curve and can be calculated by:

$$F_0 = \sqrt{F_2 F_{sat}\,\Delta\mathrm{R}} \qquad \textbf{Eq (4.15)}$$

To select the appropriate SESAM for the configuration. It is necessary to have a thorough understanding of the precise values of the laser's pulse parameter. In the following of this chapter, we will discuss regarding to these important factors.

Pulse fluence, also known as pulse energy density, is one of the important parameters to choose the right SESAM. As it mentioned before for working properly of SESAM, the pulse fluence should be larger than the SESAM saturation fluence and the pulse fluence is calculated by [193]:

$$Pulse\ fluence\left(\frac{J}{cm^2}\right) = \frac{Energy\ per\ pulse(J)}{Beam\ area(cm^2)} \qquad \textbf{Eq (4.16)}$$

Where the pulse energy is calculated by [194]:

$$Pulse\ energy(J) = \frac{Average\ power(W)}{Repetition\ rate(Hz)} \qquad \textbf{Eq (4.17)}$$

And beam area, A expressed as:

$$A = \pi\left(\frac{d}{2}\right)^2 \qquad \textbf{Eq (4.18)}$$

While d is the Focused beam spot diameter on the SESAM and calculate with the following formula [195]:

$$Spot\ size(mm) = \frac{4\times Focal\ length(mm)\times Wavelength(mm)\times M^2}{\pi\times Beam\ diameter\ at\ lens(mm)} \qquad \textbf{Eq (4.19)}$$

Note that, the M^2 is the beam quality parameter and measure of how much a laser beam deviates from the ideal Gaussian beam, in our case $M^2 = 1$.

Chapter 5: Nonlinear Optical Microscopy

5.1 Introduction

Light plays an important role for human survival since photosynthesis is the cornerstone of food creation. Therefore, humans have always utilized sunshine, despite having just a few millennia's worth of knowledge about what light is and how it operates [196]. Today, light is also significant from a technological standpoint. The United Nations named 2015 the International Year of Light, and Light-Based Technologies to highlight the significance of light and enhance our knowledge of light-based technologies in our daily lives and how they can be exploited in the future. Everyone is aware, for instance, that we cannot see without light. Still, light may also aid us in energy production, education, agriculture, communications, and health [197]. As sight is so integral to our existence, it is not unexpected that people have been fascinated with light for centuries. Mirrors were the earliest optical devices created more than 3,000 years ago. Moreover, a positive lens, which focuses light, has been known since at least 2000 B.C [198]. Starting with mirrors and lenses, the progress of optics, both theoretically and practically, has provided humans with numerous useful tools. It was discovered towards the end of the 16th century that when several lenses were coupled, even more magnification could be attained. The resulting instrument, a microscope, is utilized to discern minute objects and structures. Galileo invented a telescope at the beginning of the 17th century, allowing for the observation of distant objects shortly after the invention of the microscope [199]. The discovery of light's quantum nature marked the beginning of the enormous growth of optics and optical technology during the 20th century. On this basis, the first laser was constructed in the 1960s, introducing a new type of light source capable of creating a high-powered coherent beam. Consequently, a new age in optics began, which resulted in the discovery of numerous unique phenomena and the design of devices and applications. Nonlinear optics was one of the latest and critical optical fields found after the invention of the laser [200]. Typically, nonlinear effects are so faint that they are undetectable, but when illuminated by a powerful laser, they become visible. This chapter focuses on one of the nonlinear effects known as second-harmonic generation (SHG) and its application in microscopy. In this process, the intense excitation field interacts with the material to generate new frequency components. In nonlinear microscopy, the excitation field is concentrated on the sample, and the magnified image is usually created by detecting the sample's nonlinear signal point-by-point. As the signal usually originates from a limited focus volume, the nature of nonlinear processes enables optical sectioning. In principle, the nonlinear microscope includes a laser source described in the previous chapters, a microscope objective, a beam or sample scanning apparatus, filter, condenser, and a detector.

5.2 Nonlinear Optics (NLO)

As it is mentioned in part 3.2.2 of this thesis, in linear optics, because susceptibility is not a function of the electric field, the equations between polarization and the electric field are rigorously valid. Nonlinear optics needs to examine the effect of an electric susceptibility that varies with the electric field intensity of the incident light beam and its following optical properties [201]. The real and imaginary parts of the dielectric constant determine the optical characteristics of a medium and ε_r is derived from the polarization $\vec{P}$ of the medium:

$$\boldsymbol{\vec{D} = \varepsilon_0 \vec{E} + \vec{P} = \varepsilon_0 \varepsilon_r \vec{E}} \qquad \textbf{Eq (5.1)}$$

At lower excitation intensity, once the optical response of a medium is linear, the relation between the induced dielectric polarization and the electric field of the incident radiation is linear and can be expressed as:

$$\boldsymbol{\vec{P} = \varepsilon_0 \chi^{(1)} \vec{E}} \qquad \textbf{Eq (5.2)}$$

Where $\chi^{(1)}$ is known as the linear susceptibility [202].

The combination of Equations (5.1) and (5.2) gives the following relation:

$$\boldsymbol{\varepsilon_r = 1 + \chi^{(1)}} \qquad \textbf{Eq (5.3)}$$

In nonlinear optics, the relation between $\vec{E}$ and $\vec{P}$ can be described as the sum of a response of first order and a series of nonlinear factors of increasing order:

$$\boldsymbol{\vec{P} = \vec{P}^{L} + \vec{P}^{NL} = \vec{P}^{(1)} + \vec{P}^{(2)} + \vec{P}^{(3)} + \cdots} \qquad \textbf{Eq (5.4)}$$

where $\boldsymbol{\vec{P}^{(n)}}$ is the $\boldsymbol{n}$th order nonlinear polarization.

The combination of Equations (5.2) and (5.4) gives the following relation, which is the material's nonlinear response as a Taylor expansion of the applied electric field of $\vec{E}$:

$$\boldsymbol{P = \varepsilon_0 (\chi^{(1)} E_\omega + \chi^{(2)} E_\omega E_\omega + \chi^{(3)} E_\omega E_\omega E_\omega + \cdots)} \qquad \textbf{Eq (5.5)}$$

where $\chi^{(n)}$ is the tensor of nth order nonlinear process.

Since the linear susceptibility $\chi^{(1)}$ is significantly more prominent than the nonlinear susceptibilities, optical nonlinearities are only discernible in fields of high amplitude. This implies that, to a very reasonable approximation, the material response to incident fields of weak to moderate intensities will be linear. With more significant fields, the higher-order terms of the Taylor expansion become prominent as the nonlinear response of electrons within the medium. By high intensity fields ($E_{incident} \geq E_{atom}$), the Taylor expansion fails, and optical field ionization rips electrons from atoms [203].

5.3 Second harmonic generation (SHG)

Nonlinear optics is a part of science that includes numerous phenomena, including the second harmonic generation. A medium displays a linear response to light under typical conditions, assuming that optical parameters such as the refractive index, absorption coefficient, and reflectivity are independent of the optical power. This estimate, though, is only valid at low power levels. With the emergence of lasers in 1960 and the rapid development of mode-locked lasers since the early 1980s, optical powers escalated to a level where the response of the medium started to deviate from the linear behavior [201]. The discovery of nonlinear interactions between light and matter spawned an entirely new subject of nonlinear optics, enabling the study of various exciting phenomena, including second harmonic generation and other frequency mixing phenomena [204]. As depicted in figure 5.1, SHG is a nonlinear operation in which a portion of the energy of an optical wave with frequency ω traveling through a nonlinear medium is converted into a wave with frequency 2ω, which is twice the original frequency. SHG is also known as frequency doubling, a special instance of sum frequency generation [204]. It is a parametric process characterized by $\omega_1 + \omega_2 = \omega_3$. In the instance of SHG, the pump frequency is ω_1=ω_2 and the output harmonic frequency, ω_3, is double the pump frequency. As there is no residual energy in the material, the process results in no losses, and this procedure is considered coherent [205].

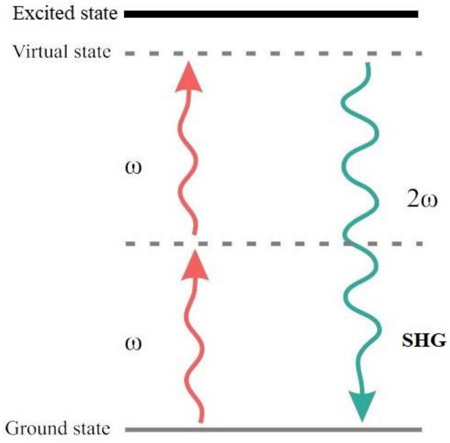

Fig. 5.1: Energy-level diagram for SHG process.

As the techniques of nonlinear optics have become more complex, SHG has found a wider range of applications, from confirming fundamental parts of quantum theory to studying optical surfaces [206, 207]. SHG microscopy is a use of SHG that is becoming increasingly significant. Specifically, new approaches for analyzing and visualizing the fine structure of collagen tissues have undergone considerable development over the past decades. Several positive characteristics of SHG microscopy make it a suitable imaging technique for examining biological substances and living organisms. As SHG is a parametric process that results from energy transferring, the sample is substantially less susceptible to photobleaching and phototoxicity compared to other methods of nonlinear microscopy. Non-linear optical microscopy techniques, including SHG microscopy, are used not only for micrometric resolution but also for penetration depth with infrared lasers in biological tissues. Light penetration into tissue is highly wavelength dependent. Thus, the higher wavelength lights will penetrate deeper into the tissues than the lower wavelength lights. Then, comparatively long near-infrared wavelengths commonly employed in SHG microscopy provide great penetration depths and are well tolerated by tissue samples.

5.4 Phase-matching

In general, the magnitudes of nonlinear optical phenomena are small and tend to reduce with higher harmonic order. A sufficiently long nonlinear medium is necessary to achieve functional nonlinear conversion efficiency. To obtain optimal SHG conversion efficiency, the phase of the second harmonic waves created throughout the crystal must be the same to permit coherent summation of the fields. This is referred to as phase-matching [201, 203, 208].

Franken's experiment in 1961, in which a very weak 347 nm-SHG signal was obtained by focusing a ruby laser (694 nm) into a quartz crystal. Considering that the field of the laser is a z-propagating plane wave, the expression is as follows:

$$\boldsymbol{E_1 = A_1 \cos(2\omega t - k_1 z)} \qquad \textbf{Eq (5.10)}$$

Where, $k_1 = \frac{n_1\omega}{c}$, is the angular wave number of the fundamental beam and $n_1$is the refractive index.

Consequently, the polarization element of the second-harmonic term is given by:

$$\boldsymbol{P^{(2)} = \frac{1}{2}\varepsilon_0 \chi^{(2)} A_1^2 \, cos(2\omega t - 2k_1 z)} \qquad \textbf{Eq (5.11)}$$

comparison of the space-time dependence in Equation 5.10 with that of a freely propagating field at twice the same frequency expressed as:

$$\boldsymbol{E_2 = A_2\cos(2\omega t - k_2 z)} \qquad \textbf{Eq (5.12)}$$

Where, $k_2 = \frac{n_2\omega}{c}$, the arguments of equations 5.10 and 5.11 are different, unless $2k_1 = k_2(\Delta k = 0)$, and it is only true when $n_1 = n_2$. As all substances are dispersive, the quartz crystal's refractive index has different value at 694 nm and 347 nm [201, 203, 208].

As a result, the second harmonic and fundamental waves will travel with distinct phase velocities, and the front-generated second-harmonic waves will arrive at the back of the quartz crystal at a different time than the fundamental waves depicted in figure 5.2 (b). Consequently, waves of 347 nm created at the back of the crystal will be out of phase with those generated at the front.

In addition, the coherence length can be calculated as:

$$\boldsymbol{l_c = \frac{\pi}{|k_2 - k_1|} = \frac{\lambda}{4|n_2 - n_1|}} \qquad \textbf{Eq (5.13)}$$

The average coherence length is on the order of tens of microns, which means that only a few microns of the 1-mm quartz crystal contributed to the exceedingly faint SHG signal seen.

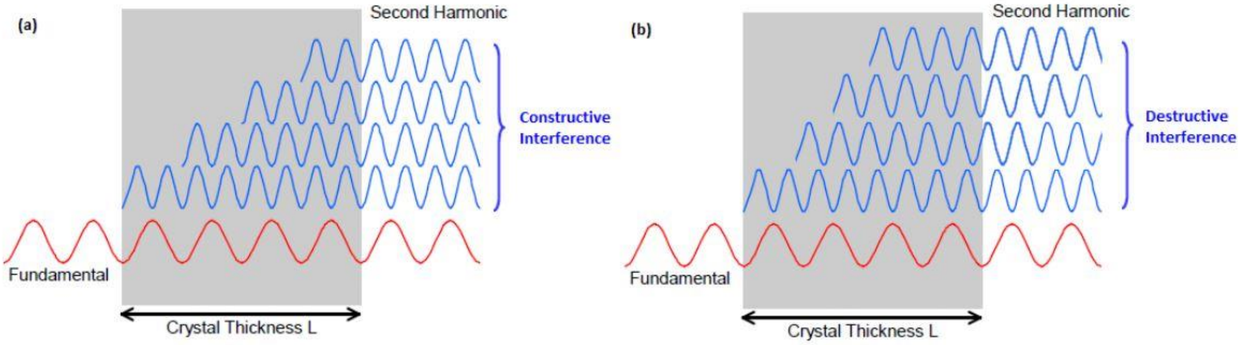

Fig. 5.2: (a) Phase-matching principle, in which all generated dipoles radiate in-phase in the forward direction so that SHG adds up constructively. (b) phase-matching is not satisfied, and the SHG interfere destructively [209].

In order to observe SHG signals, it is essential to phase-match the emitted electric field. Phase-matching guarantees that the second harmonic contributions from all points in the crystal sum coherently and are not cancelled out by destructive interference. Figure 5.2(a) depicts the state of phase-matching in a nonlinear crystal. This criterion is typically met by utilizing the birefringence of anisotropic crystals.

SHG is a coherent process, then, phase plays a crucial role in formation of signal, from molecular to macromolecular level. Considering the slowly varying envelop approximation and using an incident laser beam with fixed polarization and propagation direction, the SHG intensity can be written as follows:

$$\boldsymbol{I_{SHG} \propto |\psi|^4 L^2 \mathrm{sinc}^2\left(\frac{\Delta KL}{2}\right) = I_{\mathrm{in}}^2 L^2 \mathrm{sinc}^2\left(\frac{L}{L_c}\right)} \qquad \textbf{Eq (5.14)}$$

Where ψ is the complex amplitude of the incident beam, L is the length over which SHG occurs in the medium, I_{in} is the intensity of the incident laser beam, $\Delta k = 2k_{\omega} - k_{2\omega}$ is the phase mismatch between the excitation and the emitted light (expressed as the difference of wave-vectors) and $L_c = \frac{2}{\Delta k}$ is the coherence length. When the phase-matching condition is $\Delta k = 0$, the SHG intensity directly scales with the square of the input laser intensity and with the square of L. If $\Delta k \neq 0$, the SHG intensity reaches a maximum value after an interaction length of $\frac{\pi L_c}{2}$. In this case, if the interaction length L is any longer in the material, the SHG intensity oscillates between zero and the maximum value over a spatial period of $2\pi L_c$. Figure 5.3 efficiency of SHG as a function of phase matching.[210]

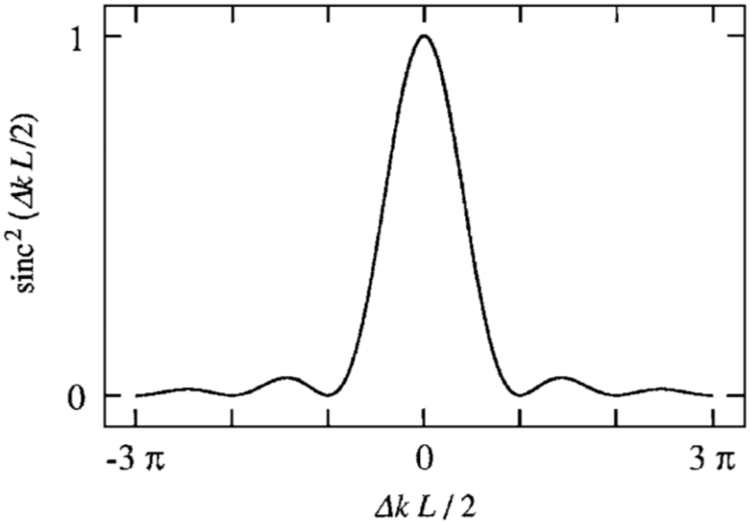

Fig. 5.3: Efficiency of SHG as a function of phase matching [211].

5.4.1 BBO and LBO crystals

Beta barium borate (-Ba2BO4) and Lithium tri borate (LiB3O5), known as BBO and LBO crystals respectively, are the most important nonlinear optical crystals used in laser optics, due to their remarkable optical properties, including a broad spectral range for nonlinear frequency conversion that ranges from the ultraviolet to the infrared and possesses a broad optical transmittance range as well as a high laser damage threshold [212, 213]. Those are chemically stable crystals with a high melting point and wide temperature stability. Anisotropy and its angle-tuning range for phase matching are the defining characteristics of the BBO crystal. BBO is a birefringent crystal with a single axis. At room temperature, its ordinary-ray (n_0) and extraordinary-ray (n_e) refractive indices are 1.6558 and 1.5429, respectively, at 1032 nm. BBO has a remarkable high effective nonlinear coefficient (deff= 1.94 pm/V) nearly four times greater than other standard nonlinear crystals such as, potassium titanyl phosphate (KTiOPO4) or KDP crystals. This indicates that BBO is far more efficient than KDP at generating second harmonics [214].

The variation of the refractive indices and the group velocities as functions of wavelength in a tuning range of these crystals are shown in figure 5.4. According to the diagram, the group reflective index of BBO and LBO is increasing from 1Micron to 532 nm. This amount in both crystals at 532nm is higher than 1064 nm.

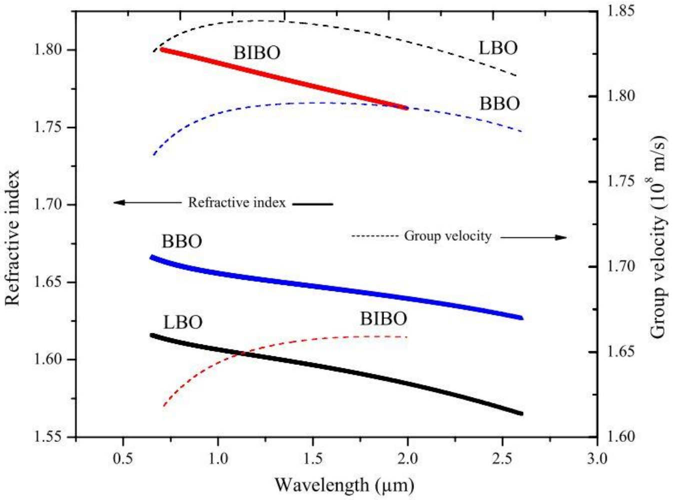

Fig. 5.4: The refractive index profiles and the group velocities versus the wavelength at room temperature [215].

Nonlinear crystal's phase-matching properties are dependent on its crystal structure, the polarization states of the interacting waves, wavelength, and crystal orientation. The phase-matched interaction will occur under two conditions: the energy conservation condition (ω3 = ω2 + ω1), and the momentum conservation condition (k3 = k2 + k1), where ωj=1,2,3 and kj=1,2,3 are the frequencies and wavenumbers of pump, signal, and idler, respectively. On the other hand, a suitable phase-matching is dependent on the range of wavelengths, and the angular and temperature sensitivities of the chosen crystal. The BBO crystal does not significantly respond to temperature changes and its best performance will occur at approximately room temperature while the LBO has its best efficiency at about 160 ◦C [215].

5.5 Nonlinear microscopy

Optical microscopes traditionally rely on linear optical effects. Nonetheless, the focus of this chapter is on SHG microscopy which is a kind of nonlinear optical microscopy (NLOM) and contains all methods that depend on NLO effects for imaging. NLOM differs fundamentally from basic optical microscopy, in NLOM measured amount is not scattered, reflected, or fluorescent light, but rather the light generated in the target object as a result of nonlinear interactions. Infrared light is frequently utilized in nonlinear microscopy [26]. In NLOM approaches, the target is often excited by a concentrated laser beam, as the nonlinear response exists only at regions with extremely high input light intensities. Due to these two factors, the observed nonlinear signal originates only from a small volume at the focal point of the incoming field, and contributions from out-of-focus regions are negligible. This makes it feasible to obtain optical sectioning images of not only surfaces, but also objects within the sample [216]. Using near-infrared wavelengths, biological samples can be penetrated to a depth of 500μm or more in SHG microscopy [217]. Using confocal techniques, which reject out-of-focus light from the detector with a spatial filter like a pinhole in the focal plane of the focusing lens, optical sectioning is also achievable in linear microscopy [218].

Nevertheless, linear microscopy often employs lower wavelengths than nonlinear microscopy, therefore, the penetration depth length into biological tissue is not as good as in nonlinear microscopy. Since the signal in nonlinear microscopy always comes from a focal volume, it is impossible to scan the entire sample area in one time, unless using wide-field microscopy. Therefore, a scan of the area under consideration is required. This technique is known as laser scanning microscopy, in which an image of the sample is created by traversing the sample region point-by-point, forming a raster pattern. Changing the position between the sample and the beam can be performed by moving the sample stage relative to a stable excitation beam or by utilizing mirrors to move the excitation beam along the sample surface. The improvement of the laser methods over the past few decades has provided the foundation for developing NLOM techniques [217]. NLOM was primarily employed for material science like engineering in the past, but it is currently a popular study approach in biology [219]. It gives spatial resolutions as small as sub-micrometric regimes and temporal scales as small as femtoseconds. As stated previously, NLOM permits deeper penetration into sample material and a higher signal-to-noise ratio than linear approaches. NLOM techniques include two-photon excited fluorescence (TPEF), third harmonic generation (THG), second harmonic generation, sum frequency generation (SFG), coherent anti-Stokes Raman scattering, and four wave mixing (FWM), each with its own application goals. For specific applications, it is also advantageous to combine two or more NLOM techniques, such as TPEF, SHG, and THG, and it is conceivable to combine NLOM with other imaging modalities [220-222].

5.6 Linear and nonlinear fluorescence microscopy

Single-photon excited fluorescence (SPEF) microscopy is a form of linear optical microscopy. In fluorescence, a molecule named a fluorophore absorbs a photon of high energy and, after a short delay, emits a photon with less energy. Between the final state of absorption and the beginning state of fluorescence transition, a non-radiative vibrational relaxation occurs that results in the loss of energy, as shown in figure 5.5. In fluorescence microscopy, the emitted fluorescence signal is measured, allowing for the investigation of phenomena such as the movement of molecules within cells. The return of an excited molecule to its ground state is not limited to fluorescence [223]. The wavelength of fluorescent light roughly correlates to the energy difference between the ground state and the excited state and is therefore nearly constant for every given molecule. Consequently, the fluorescence signal is easily distinguished from other spectrum components of radiation using filters suited for differentiating between fluorescence and excitation.

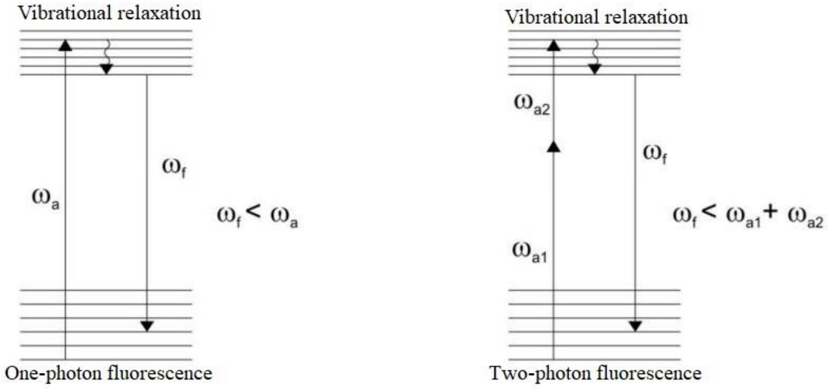

Fig. 5.5: depiction of single- and two-photon fluorescence phenomena.

TPEF is the nonlinear equivalent of fluorescence. The concept is like one-photon fluorescence, but in TPEF the stimulation to the high-energy state is triggered by the simultaneous absorption of two photons instead of one photon. The total of these two photons' energies should equal the energy difference between the ground and excited states. Since the absorption of the two photons must be nearly synchronous, the possibility of this occurrence under ambient conditions is extremely low (almost zero). By focusing a pulsed laser beam on the sample, a high photon density can be obtained for TPEF. Therefore, the chance of TPEF is relatively high within the narrow focal volume but rapidly diminishes outside the focal volume. This enables imaging with higher quality than SPEF, as TPEF fluorescence emanates exclusively from the desired region [223].

The fluorescence signal from a sample for SPEF and TPEF is depicted in figure 5.6. The SPEF signal arises from the whole path of the excitation beam, while the TPEF signal is produced only at the focus.

Furthermore, to its quality, an additional benefit of TPEF is that the longer wavelength utilized for excitation enables deeper penetration into highly scattering tissues, such as living cells, than is possible with conventional fluorescence microscopy [216].

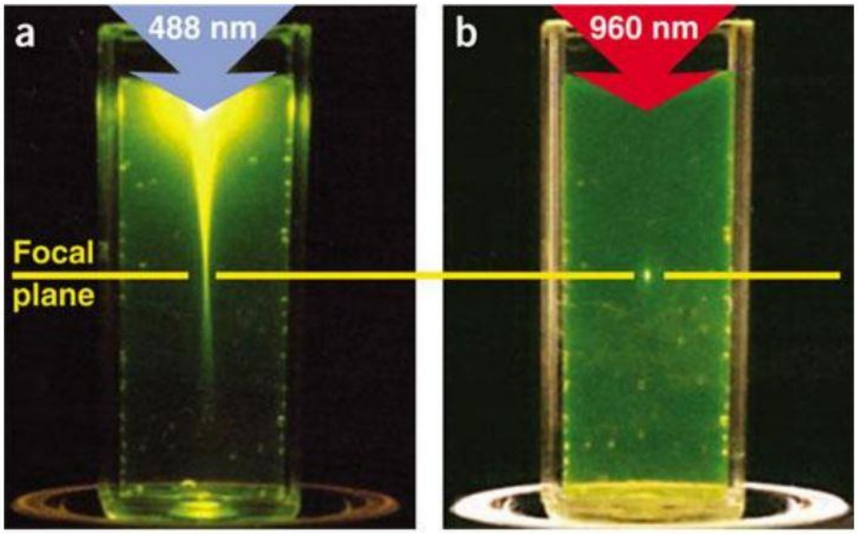

Fig. 5.6: a) In SPEF the signal originates from the whole excitation path through the sample, (b) In TPEF the signal comes only from the small focal volume [20].

5.7 Second-harmonic generation microscopy

In this part we will discuss the relationship between the polarization vector P and the electric field component E of the light. In optical media, an electric field oscillating at high frequency would cause the induction of polarization in the material by pulling the electrons back and forth [211]. Totally the polarization of the material interacting with light is given by equations in section 5.2 of this thesis.

As it is mentioned at session 5.2, $\chi^{(1)}$ term corresponds to linear effects, the $\chi^{(2)}$ term defines second order nonlinear interactions, like SHG [211], and the $\chi^{(3)}$ term describes third order nonlinear effects such as: two-photon absorption [18], third harmonic generation [224] and self-phase modulation [143].

In the field of microscopy, 2PEF and SHG have numerous similar technical characteristics that make their combination simple and effective for using the same instrument. The laser wavelength is typically in the NIR-I range (700-1000 nm) to avoid absorption by biomaterials such as water and hemoglobin [25], but there are several other optical "windows" are satisfying this condition, as shown in figure 5.7. Regarding biological materials, imaging of deep tissue is of paramount importance. The depth of imaging is depends on the excitation wavelength of the laser [19, 225]. Longer wavelengths, for example NIR-II region in

Figure 5.7, provide a deeper tissue penetration since sufficient light can reach the focal volume of the tissue with minimal scattering [19, 225].

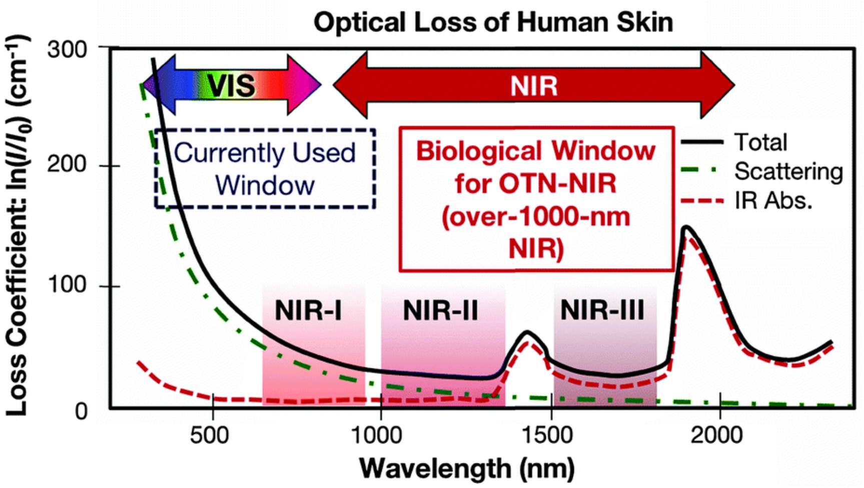

Fig. 5.7: Absorption spectrum of the human skin, indicating 3 possible transparency windows [25].

To generate the efficient nonlinear optical signal, a typical pulse duration of 100 femtoseconds with a repetition rate of a few tens of megahertz is utilized [19]. In the space, a high numerical aperture (NA) objective is utilized to focus the laser pulse energy by focusing light on the sample [14]. For thin samples in which light can detect in the forward direction, a high numerical aperture condenser is added to efficiently collect the light [226]. Due to the confinement of signal production in the focal volume, both modalities exhibit a quadratic dependence of the generated signal on the input laser intensity [14], resulting in a three-dimensional spatial resolution [18]. Despite these similarities, SHG and 2PEF modes are based on fundamentally different methods: in SHG, frequency conversion is performed through virtual states without a net energy transfer to the system, whereas in 2PEF, population transfer from ground to excited electronic states is involved (Figure 5.8).

Second-order nonlinear processes, like SHG, can be effectively characterized by an anharmonic oscillator model in which the atomic potential generates a nonlinear restoring force. Using a one-dimensional molecule as an illustration, the anharmonic potential surface will cause a temporal distortion of the induced polarization [227]. The degree of inharmoniousness is proportional to the driving field input. In fact, each element of the second-order nonlinear susceptibility $\chi^{(2)}$, disappears in centrosymmetric materials, preventing the development of SHG. This is simply explicable by analyzing the nonlinear polarization formulas (Session 5.2) for the second order. In the scale of one molecule, SHG can be generated by a single dipole moment in the presence of a non-zero field, while in the macroscopic scale, the coherent nature of

SHG mandates that the molecules must be aligned and structured for SHG emission because each dipole moment contribution is added.

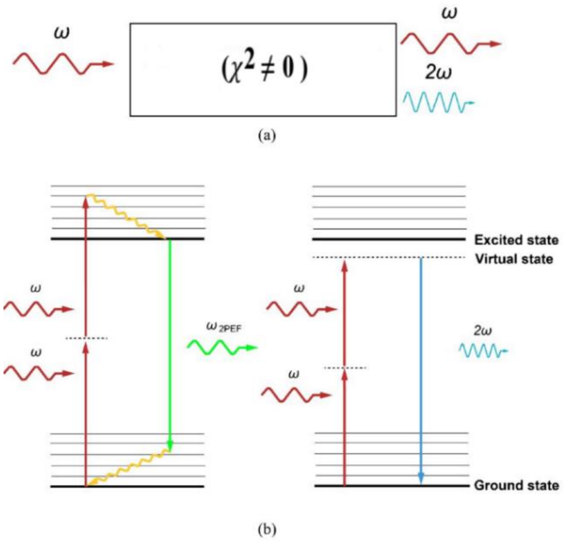

Fig. 5.8: 2PEF vs SHG. (a) For SHG to occur, a noncentrosymmetric material ($\chi^2 \neq 0$) is illuminated by a pulsed laser at central frequency ω and SHG, light at 2 ω is generated [228]. (b) Diagram of corresponding energy levels for 2PEF and SHG. Two photons are absorbed in 2PEF, causing electronic excitation of the molecules (fluorophores). Following internal relaxation, spontaneous emission takes place. In the instance of SHG, two incident photons interact with the medium via a virtual state, resulting in the creation of a photon with a frequency (2ω) exactly double that of the incident photons. SHG is a parametric process in which there is no energy transfer [229].

In conclusion, well-ordered non-centrosymmetric molecules exhibit a substantial second-order nonlinear susceptibility that is necessary for SHG [227]. Figure 5.9 shows an example of SHG with two dipoles which have a negligible distance with respect to the wavelength of the incoming light wave (i.e., d<<λ):

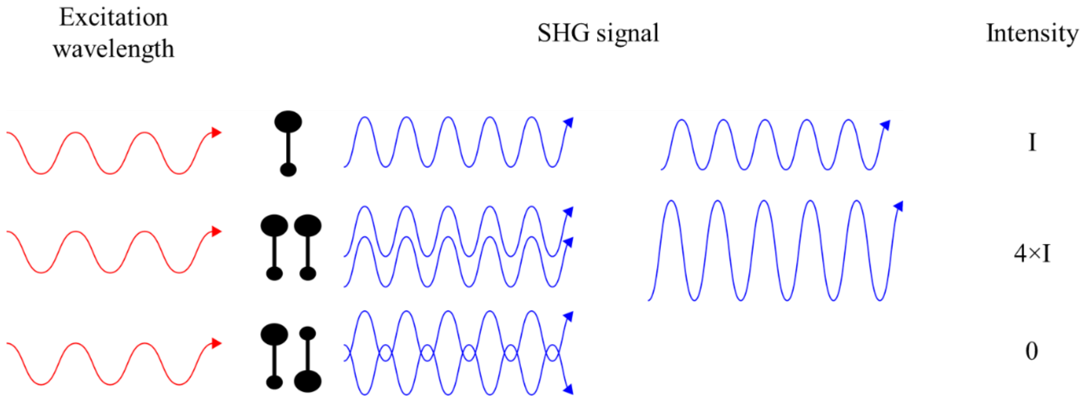

Fig. 5.9: SHG signal from two parallel and anti-parallel dipoles. Extracted from [230].

The first case, which illustrates a single dipole moment, SHG is generated proportionate to the intensity I. In the second situation, two dipole moments are in phase and constructively interfere, resulting in a higher

SHG intensity of 4 × I. In the last situation, although SHG is formed from each dipole moment, the resulting intensity is 0 since they are fully out of phase with each another.

A medium needs to satisfy three conditions for SHG to occur: the presence of a permanent dipole moment in the molecules of the medium, the hyperpolarizability should not be zero, and the presence of an ordered array of aligned dipole moments [227].

5.8 Wide-field SHG microscopy

Scanning SHG imaging is such a well technique that has been utilized in a variety of applications. one of the basic limits of this approach is its low-speed imaging output. This limitation hinders its use for label-free imaging of extremely rapid biological processes (millisecond time scale) [27]. To increase the imaging performance, two ways are imaginable: increasing the scanning speed or parallelize photon emission [28]. Acousto-optic deflectors [231] and resonant scanners [232] have been utilized well to increase scanning speed. However, they are ultimately constrained by the time necessary to emit sufficient photons to produce a recordable signal. Wide-field SHG microscopy appears to be the ultimate parallelization for the latter method, as the entire area of interest is concurrently illuminate and signals are detected on a pixelated detector [233].Wide-field SHG microscopy (WF-SHG) is a method in which the entire area of interest is concurrently illuminated, and signals are detected by a camera for this latter strategy [233]. Wide-field SHG microscopy enables live imaging of vast areas (500 × 500 mm) with submicron lateral resolution at >10 frames per second [30]. Wide-field SHG microscopy enables rapid live imaging of contracting muscle and provides non-invasive quantitative information on the contraction dynamics of sarcomeres [30]. During muscle contraction, the synchronization of sarcomere shortening, and elongation can be recorded, allowing for applications in basic contractility research and the study of arrhythmias, muscular dystrophies, and the effects of drugs on the synchronization dynamics of sarcomeres during muscle contraction. In digital histopathology, rapid wide-field SHG imaging can be used for scanning entire slides [30]. During the progression of cancer, the extra cellular matrix (ECM) of several tissues, including the thyroid, frequently becomes disorganized; consequently, SHG imaging can be used to assist diagnosis by quantifying ECM. Collagen, the most abundant protein in the ECM, may be easily seen and structurally investigated by SHG polarimetry, generating structural information from the tissue. Early detection allows for effective treatment of most malignancies. The SHG digital pathology with wide field imaging can give pathologists more information. To visualize the full histopathology slides from biopsies, novel automated imaging technologies with high scanning speed and big image size are required [234]. Compared to scanning microscopy, WF-SHG microscopy boosts image throughput by two to three orders of magnitude [28]. Due to the sensitivity of living cell samples, specific care must be taken to prevent photodamage. Multiple research study the damage threshold in WF-SHG microscopy for various cells, with the primary takeaway being to maintain pulse energy and, consequently, heat deposition below the damage threshold of the samples [30]. Traditionally, wide-field SHG microscopy was performed using high-energy (Micro Jules level) pulses from lasers operated at multi-kHz repetition rate. Recent developments have enabled the development of a high repetition rate (MHz) WF-SHG microscope for live imaging of contracting muscle tissue that employs laser pulses with pulse energies as low as around 60nJ [30]. A typical wide-field SHG setup is shown in figure 5.10.

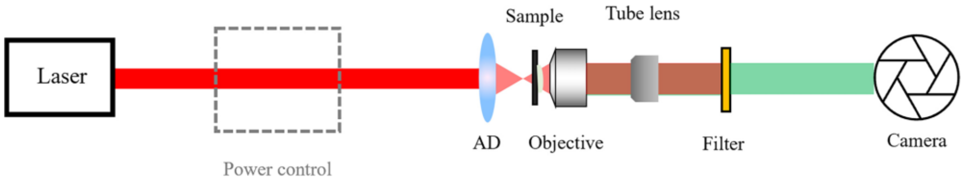

Fig. 5.10: Standard WF-SHG setup the laser light source is between 700 and 1100 nanometers. For power control, the Half wave plate and a polarizer are utilized. The incoming laser beam is focused using an achromat doublet lens, and the sample is placed slightly above the focus. Using the objective and tube lens, the SHG signal from the sample is collected. After filtration, a scientific camera acquires the SHG signal [210].

5.9 Experimental Setup

The main goal of the project was to build a unique pulsed fiber laser to use as an excitation light source for wide-field SHG microscopy. Thus, the custom-built SHG microscope is designed to test the efficiency of the laser, which is shown in figure 5.11.

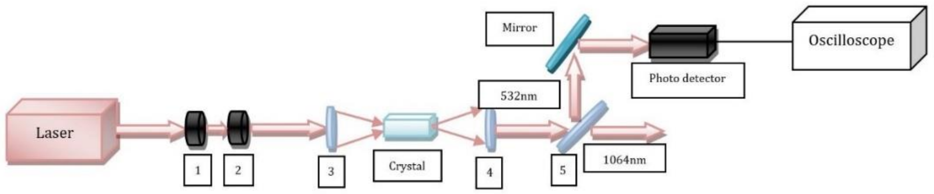

1. Half waveplate
2. Polarizer
3. Lens
4. Lens
5. Harmonic separator

Fig. 5.11: Experimental setup for SHG.

Beam alignment is critical for minimizing signal losses in SHG microscopy, so all the optical components are fixed on the table using the post holders to improve the efficiency and reduce its susceptibility to misalignment. The laser output beam is precisely aligned to propagate through the Half wave plate and polarizer, which are employed to control the amount of power. The first lens is used to focus the laser beam on the BBO crystal, the BBO crystal emits frequency-doubled light (532 nm) in both forward and backward directions. The second lens is positioned after the crystal to correct the beam divergence so that the microscope detector collects maximal incident light. For forward SHG measurements, the setup will work in transmission mode, in which the forward component of SHG light propagates in the same direction as the laser beam. The harmonic separator will filter out the 1064 nm laser light, allowing the photo detector to detect only the SHG signal. As a result, the SHG setup produces 2.5 W green light (532 nm), which means around 40 percent efficiency, as illustrated by figure 5.12.

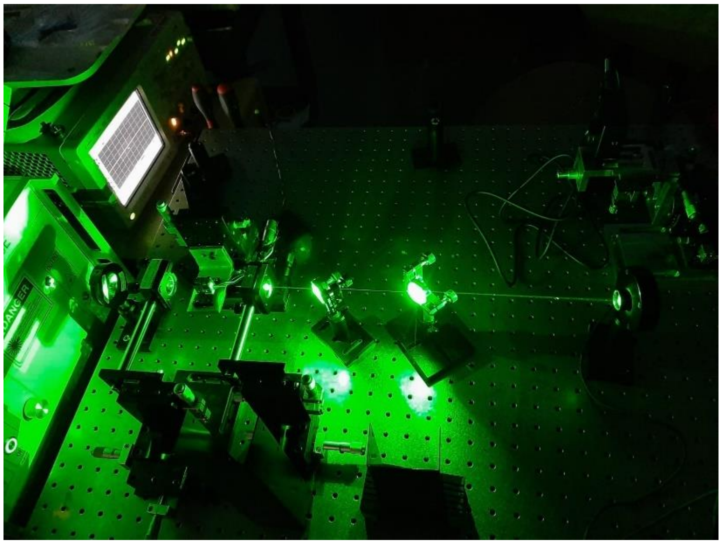

Fig. 5.12: Setup for SHG.

Chapter 6: Conclusion

In nonlinear optics, an optical beam focused on a sample produces a response proportional to the excitation beam. This phenomenon is applicable, for instance, to microscopy, where it serves as a basic tool for analyzing optical metamaterials and biological samples. In comparison to linear optical microscopy techniques, the advantages of nonlinear techniques are deeper tissue penetration and greater contrast. SHG is the basis for one of the most popular nonlinear microscopy techniques. The wavelength of the signal in SHG is half of the wavelength of the initial excitation field. SHG microscopies can be used, for example, to investigate the surface impacts of nanoparticles and the processes of biological systems.

Since image acquisition rate of microscopy is limited by the laser scanning speed, in wide-field SHG microscopy, which is a kind of SHG microscopy, the entire area of interest is concurrently illuminated and signals are detected by a camera for this latter strategy which enables fast large area imaging however, it requires short laser pulses with high energy. Because of the sensitivity of living cell samples, special precautions must be taken to avoid photodamage. For deeper tissue penetration, longer wavelengths in the region of 1000-1300 nm are used for minimal scattering.

One of the main parts of nonlinear microscopy setup is the pulsed laser which is used as the excitation light source. In addition, the laser requires a stable environment and high P2P stability to operate effectively which I presented in this thesis.

In summary, the study provided in this thesis falls under two main research categories. First, present a comprehensive examination of passive mode-locked polarization-maintaining fiber laser operating in the 1 μm wavelength region. Consequently, we proved the pulse characteristics of a SESAM-based laser with a linear cavity. Standard ultrashort pulse characterization techniques were employed to diagnose laser behaviors. The optical spectrum and the RF spectrum were also examined. The laser schemes proposed in this study utilized Yb-doped active fiber as the gain medium and were operated under all-normal dispersion regimes. Experiments were conducted on the proposed linear cavity SESAM laser in a mode-locked region with an average output power of 7 W. On the oscilloscope, the fundamental repetition rate was observed to be 42 MHz, which corresponds to a cavity length of around 2.5 m. After compression, the 200 fs pulse width was measured using an autocorrelator. In consequence, the peak power and pulse energy were 798 kW and 166 nJ, respectively. Also, the P2P stability of the seed and output of the 1064 nm mode-locked fiber laser was around 2.4% and 3.4%, respectively. In the second section of this thesis, nonlinear microscopy investigations were reported as an application of this laser.

As I have covered the majority of the characterization and measurements of these pulsed fiber lasers in this study, I am convinced that the observations presented in this thesis will provide researchers in the field of fiber lasers with more benefits.

REFERENCES

[1] A. Prylepa, G. Luckeneder, K. Stellnberger, and D. Stifter, "Low coherence interferometric second harmonic generation microscopy for non-destructive material testing using a broadband 1550 nm fs-fiber laser," *Laser Physics,* vol. 24, no. 4, p. 045407, 2014.

[2] R. Lehneis, A. Steinmetz, J. Limpert, and A. Tünnermann, "All-fiber pulse shortening of passively Q-switched microchip laser pulses down to sub-200 fs," *Optics letters,* vol. 39, no. 20, pp. 5806-5809, 2014.

[3] Z. Zhang, Z. Yan, K. Zhou, and L. Zhang, "All-fiber 250 MHz fundamental repetition rate pulsed laser with tilted fiber grating polarizer," *Laser Physics Letters,* vol. 12, no. 4, p. 045102, 2015.

[4] C. Zhao *et al.*, "Ultra-short pulse generation by a topological insulator based saturable absorber," *Applied Physics Letters,* vol. 101, no. 21, p. 211106, 2012.

[5] Z. Zhang, C. Mou, Z. Yan, K. Zhou, L. Zhang, and S. Turitsyn, "Sub-100 fs mode-locked erbium-doped fiber laser using a 45-tilted fiber grating," *Optics express,* vol. 21, no. 23, pp. 28297-28303, 2013.

[6] M. Ober, M. Hofer, and M. E. Fermann, "42-fs pulse generation from a mode-locked fiber laser started with a moving mirror," *Optics Letters,* vol. 18, no. 5, pp. 367-369, 1993.

[7] H. Haus and M. Islam, "Theory of the soliton laser," *IEEE journal of quantum electronics,* vol. 21, no. 8, pp. 1172-1188, 1985.

[8] K. Hill *et al.*, "Chirped in-fiber Bragg gratings for compensation of optical-fiber dispersion," *Optics letters,* vol. 19, no. 17, pp. 1314-1316, 1994.

[9] Y. Wang *et al.*, "Strain compensated robust semiconductor saturable absorber mirror for fiber lasers," *Chinese Optics Letters,* vol. 17, no. 7, p. 071404, 2019.

[10] L. A. Vazquez-Zuniga and Y. Jeong, "Wavelength-tunable, passively mode-locked erbium-doped fiber master-oscillator incorporating a semiconductor saturable absorber mirror," *Journal of the Optical Society of Korea,* vol. 17, no. 2, pp. 117-129, 2013.

[11] J. R. Blackford, "Sintering and microstructure of ice: a review," *Journal of Physics D: Applied Physics,* vol. 40, no. 21, p. R355, 2007.

[12] O. Shtyrina, M. Fedoruk, S. Turitsyn, R. Herda, and O. Okhotnikov, "Evolution and stability of pulse regimes in SESAM-mode-locked femtosecond fiber lasers," *JOSA B,* vol. 26, no. 2, pp. 346-352, 2009.

[13] T. Hakkarainen *et al.*, "Optical properties of ion irradiated and annealed InGaAs/GaAs quantum wells and semiconductor saturable absorber mirrors," *Journal Of Physics D: Applied Physics,* vol. 38, no. 7, p. 985, 2005.

[14] P. J. Campagnola and L. M. Loew, "Second-harmonic imaging microscopy for visualizing biomolecular arrays in cells, tissues and organisms," *Nature biotechnology,* vol. 21, no. 11, pp. 1356-1360, 2003.

[15] G. Cox, "Biological applications of second harmonic imaging," *Biophysical reviews,* vol. 3, no. 3, pp. 131-141, 2011.

[16] W. E. Lamb Jr, "Theory of an optical maser," *Physical Review,* vol. 134, no. 6A, p. A1429, 1964.

[17] P. J. Campagnola, A. C. Millard, M. Terasaki, P. E. Hoppe, C. J. Malone, and W. A. Mohler, "Three-dimensional high-resolution second-harmonic generation imaging of endogenous structural proteins in biological tissues," *Biophysical journal,* vol. 82, no. 1, pp. 493-508, 2002.

[18] X. Chen, O. Nadiarynkh, S. Plotnikov, and P. J. Campagnola, "Second harmonic generation microscopy for quantitative analysis of collagen fibrillar structure," *Nature protocols,* vol. 7, no. 4, pp. 654-669, 2012.

[19] E. E. Hoover and J. A. Squier, "Advances in multiphoton microscopy technology," *Nature photonics,* vol. 7, no. 2, pp. 93-101, 2013.

[20] W. R. Zipfel, R. M. Williams, and W. W. Webb, "Nonlinear magic: multiphoton microscopy in the biosciences," *Nature biotechnology,* vol. 21, no. 11, pp. 1369-1377, 2003.

[21] P. Campagnola, "Second harmonic generation imaging microscopy: applications to diseases diagnostics," *Analytical chemistry,* vol. 83, no. 9, pp. 3224-3231, 2011.

[22] G. Cox, E. Kable, A. Jones, I. Fraser, F. Manconi, and M. D. Gorrell, "3-dimensional imaging of collagen using second harmonic generation," *Journal of structural biology,* vol. 141, no. 1, pp. 53-62, 2003.

[23] H. Lim, "Harmonic generation microscopy 2.0: new tricks empowering intravital imaging for neuroscience," *Frontiers in Molecular Biosciences,* vol. 6, p. 99, 2019.

[24] W. Mohler, A. C. Millard, and P. J. Campagnola, "Second harmonic generation imaging of endogenous structural proteins," *Methods,* vol. 29, no. 1, pp. 97-109, 2003.

[25] E. Hemmer, A. Benayas, F. Légaré, and F. Vetrone, "Exploiting the biological windows: current perspectives on fluorescent bioprobes emitting above 1000 nm," *Nanoscale Horizons,* vol. 1, no. 3, pp. 168-184, 2016.

[26] F. Helmchen and W. Denk, "Deep tissue two-photon microscopy," *Nature methods,* vol. 2, no. 12, pp. 932-940, 2005.

[27] P. T. So, E. Y. Yew, and C. Rowlands, "High-throughput nonlinear optical microscopy," *Biophysical journal,* vol. 105, no. 12, pp. 2641-2654, 2013.

[28] C. Macias-Romero *et al.*, "High throughput second harmonic imaging for label-free biological applications," *Optics express,* vol. 22, no. 25, pp. 31102-31112, 2014.

[29] E. Shaffer, P. Marquet, and C. Depeursinge, "Real time, nanometric 3D-tracking of nanoparticles made possible by second harmonic generation digital holographic microscopy," *Optics Express,* vol. 18, no. 16, pp. 17392-17403, 2010.

[30] R. Cisek, H. Zhao, and V. Barzda, "Wide-field second harmonic generation microscopy using a high power Yb laser," in *2017 Photonics North (PN)*, 2017: IEEE, pp. 1-1.

[31] T. A. Mokhiemer, "On the Quantum Theory of Radiation," 2008.

[32] R. Ladenburg, "Untersuchungen über die anomale Dispersion angeregter Gase," *Zeitschrift für Physik,* vol. 48, no. 1, pp. 15-25, 1928/01/01 1928, doi: 10.1007/BF01351571.

[33] J. P. Gordon, H. J. Zeiger, and C. H. Townes, "Molecular microwave oscillator and new hyperfine structure in the microwave spectrum of N H 3," *Physical Review,* vol. 95, no. 1, p. 282, 1954.

[34] J. Hecht, "A short history of laser development," *Applied optics,* vol. 49, no. 25, pp. F99-F122, 2010.

[35] T. H. Maiman, "Stimulated optical radiation in ruby," 1960.

[36] R. Terhune, P. Maker, and C. Savage, "Optical harmonic generation in calcite," *Physical Review Letters,* vol. 8, no. 10, p. 404, 1962.

[37] R. Hellwarth and F. McClung, "Giant pulsations from ruby," *Appl Phys*, vol. 33, pp. 838-841, 1962.

[38] E. Ippen, C. Shank, and A. Dienes, "Passive mode locking of the cw dye laser," *Applied Physics Letters,* vol. 21, no. 8, pp. 348-350, 1972.

[39] R. L. Fork, C. B. Cruz, P. Becker, and C. V. Shank, "Compression of optical pulses to six femtoseconds by using cubic phase compensation," *Optics letters,* vol. 12, no. 7, pp. 483-485, 1987.

[40] D. E. Spence, P. N. Kean, and W. Sibbett, "60-fsec pulse generation from a self-mode-locked Ti: sapphire laser," *Optics letters,* vol. 16, no. 1, pp. 42-44, 1991.

[41] D. Strickland and G. Mourou, "Compression of amplified chirped optical pulses," *Optics communications,* vol. 55, no. 6, pp. 447-449, 1985.

[42] P. Kelley, "Self-focusing of optical beams," *Physical Review Letters*, vol. 15, no. 26, p. 1005, 1965.

[43] M. Nisoli, S. De Silvestri, and O. Svelto, "Generation of high energy 10 fs pulses by a new pulse compression technique," *Applied Physics Letters,* vol. 68, no. 20, pp. 2793-2795, 1996.

[44] E. Goulielmakis *et al.*, "Single-cycle nonlinear optics," *Science,* vol. 320, no. 5883, pp. 1614-1617, 2008.

[45] T. Brabec and H. Kapteyn, *Strong field laser physics*. Springer, 2008.

[46] M. I. Dzhibladze, Z. G. Ésiashvili, É. S. Teplitskiĭ, S. K. Isaev, and V. R. Sagaradze, "Mode locking in a fiber laser," *Soviet Journal of Quantum Electronics,* vol. 13, no. 2, pp. 245-247, 1983/02/28 1983, doi: 10.1070/qe1983v013n02abeh004112.

[47] G. Chang and Z. Wei, "Ultrafast fiber lasers: an expanding versatile toolbox," *Iscience,* vol. 23, no. 5, p. 101101, 2020.

[48] C. Xu and F. Wise, "Recent advances in fibre lasers for nonlinear microscopy," *Nature photonics,* vol. 7, no. 11, pp. 875-882, 2013.

[49] T. Kobayashi, "Development of ultrashort pulse lasers for ultrafast spectroscopy," in *Photonics*, 2018, vol. 5, no. 3: MDPI, p. 19.

[50] T. Westphäling, "Pulsed Fiber Lasers from ns to ms range and their applications," *Physics Procedia*, vol. 5, pp. 125-136, 2010.

[51] "Fiber Laser: 7 Advantages and Differences. Access from:." https://www.findlight.net/blog/7-advantages-of-fiber-laser/. (accessed 2022).

[52] J. Jeong, S. Cho, S. Hwang, B. Lee, and T. J. Yu, "Modeling and Analysis of High-Power Ti: sapphire Laser Amplifiers–A Review," *Applied Sciences,* vol. 9, no. 12, p. 2396, 2019.

[53] C. B. Schaffer, A. Brodeur, J. F. García, and E. Mazur, "Micromachining bulk glass by use of femtosecond laser pulses with nanojoule energy," *Optics letters,* vol. 26, no. 2, pp. 93-95, 2001.

[54] R. R. Gattass and E. Mazur, "Femtosecond laser micromachining in transparent materials," *Nature photonics,* vol. 2, no. 4, pp. 219-225, 2008.

[55] B. N. Chichkov, C. Momma, S. Nolte, F. Von Alvensleben, and A. Tünnermann, "Femtosecond, picosecond and nanosecond laser ablation of solids," *Applied physics A,* vol. 63, no. 2, pp. 109-115, 1996.

[56] E. G. Gamaly, A. V. Rode, B. Luther-Davies, and V. T. Tikhonchuk, "Ablation of solids by femtosecond lasers: Ablation mechanism and ablation thresholds for metals and dielectrics," *Physics of plasmas,* vol. 9, no. 3, pp. 949-957, 2002.

[57] T. Brixner and G. Gerber, "Femtosecond polarization pulse shaping," *Optics letters,* vol. 26, no. 8, pp. 557-559, 2001.

[58] M. Plewicki, F. Weise, S. M. Weber, and A. Lindinger, "Phase, amplitude, and polarization shaping with a pulse shaper in a Mach-Zehnder interferometer," *Applied optics,* vol. 45, no. 32, pp. 8354-8359, 2006.

[59] A. Assion *et al.*, "Control of chemical reactions by feedback-optimized phase-shaped femtosecond laser pulses," *Science,* vol. 282, no. 5390, pp. 919-922, 1998.

[60] I. Pastirk, E. J. Brown, Q. Zhang, and M. Dantus, "Quantum control of the yield of a chemical reaction," *The Journal of chemical physics,* vol. 108, no. 11, pp. 4375-4378, 1998.

[61] R. J. Levis, G. M. Menkir, and H. Rabitz, "Selective bond dissociation and rearrangement with optimally tailored, strong-field laser pulses," *Science,* vol. 292, no. 5517, pp. 709-713, 2001.

[62] W. Denk, J. H. Strickler, and W. W. Webb, "Two-photon laser scanning fluorescence microscopy," *Science,* vol. 248, no. 4951, pp. 73-76, 1990.

[63] M. Fricke and T. Nielsen, "Two-dimensional imaging without scanning by multifocal multiphoton microscopy," *Applied optics,* vol. 44, no. 15, pp. 2984-2988, 2005.

[64] C. L. Evans and X. S. Xie, "Coherent anti-Stokes Raman scattering microscopy: chemical imaging for biology and medicine," *Annual review of analytical chemistry,* vol. 1, no. 1, p. 883, 2008.

[65] M. R. HEE, J. A. IZATT, J. M. JACOBSON, J. G. FUJIMOTO, and E. A. SWANSON, "Femtosecond transillumination optical coherence tomography," *SPIE milestone series,* vol. 165, pp. 177-179, 2001.

[66] I. Hartl *et al.*, "Ultrahigh-resolution optical coherence tomography using continuum generation in an air–silica microstructure optical fiber," *Optics letters,* vol. 26, no. 9, pp. 608-610, 2001.

[67] G. Tearney, B. Bouma, S. Boppart, B. Golubovic, E. Swanson, and J. Fujimoto, "Rapid acquisition of in vivo biological images by use of optical coherence tomography," *SPIE milestone series,* vol. 165, pp. 611-613, 2001.

[68] R. Vilson *et al.*, "All-optical switch on a Silicon chip," in *Proceedings of the Conference on lasers and electro-optics/international quantum electronics conference and photonic applications systems technologies, technical digest (CD), Optical Society of America, CTuFF3*, 2004.

[69] Z. Chang, A. Rundquist, H. Wang, M. M. Murnane, and H. C. Kapteyn, "Generation of coherent soft X rays at 2.7 nm using high harmonics," *Physical Review Letters,* vol. 79, no. 16, p. 2967, 1997.

[70] A. Braun, G. Korn, X. Liu, D. Du, J. Squier, and G. Mourou, "Self-channeling of high-peak-power femtosecond laser pulses in air," *Optics letters,* vol. 20, no. 1, pp. 73-75, 1995.

[71] P. Young and P. Bolton, "Propagation of subpicosecond laser pulses through a fully ionized plasma," *Physical review letters,* vol. 77, no. 22, p. 4556, 1996.

[72] R. Paschotta and U. Keller, "Passive mode locking with slow saturable absorbers," *Applied Physics B,* vol. 73, no. 7, pp. 653-662, 2001.

[73] J. D. Kafka, M. L. Watts, and J.-W. Pieterse, "Picosecond and femtosecond pulse generation in a regeneratively mode-locked Ti: sapphire laser," *IEEE journal of quantum electronics,* vol. 28, no. 10, pp. 2151-2162, 1992.

[74] J. Herrmann, "Theory of Kerr-lens mode locking: role of self-focusing and radially varying gain," *Josa b,* vol. 11, no. 3, pp. 498-512, 1994.

[75] M. Takeda, H. Ina, and S. Kobayashi, "Fourier-transform method of fringe-pattern analysis for computer-based topography and interferometry," *JosA,* vol. 72, no. 1, pp. 156-160, 1982.

[76] C. Dorrer, N. Belabas, J.-P. Likforman, and M. Joffre, "Spectral resolution and sampling issues in Fourier-transform spectral interferometry," *JOSA B,* vol. 17, no. 10, pp. 1795-1802, 2000.

[77] V. C. K. Chauhan, "Pulse compression and dispersion control in ultrafast optics," Georgia Institute of Technology, 2011.

[78] P. Bowlan, P. Gabolde, A. Shreenath, K. McGresham, R. Trebino, and S. Akturk, "Crossed-beam spectral interferometry: a simple, high-spectral-resolution method for completely characterizing complex ultrashort pulses in real time," *Optics express,* vol. 14, no. 24, pp. 11892-11900, 2006.

[79] P. Bowlan, P. Gabolde, and R. Trebino, "Directly measuring the spatio-temporal electric field of ultrashort pulses in and near a focus," in *2007 Conference on Lasers and Electro-Optics (CLEO)*, 2007: IEEE, pp. 1-2.

[80] V. Chauhan, "PULSE COMPRESSION AND DISPERSION CONTROL IN ULTRAFAST OPTICS," PHD, Georgia Institute of Technology, 2010.

[81] A. E. Siegman, "Defining, measuring, and optimizing laser beam quality," *Laser Resonators and Coherent Optics: Modeling, Technology, and Applications,* vol. 1868, pp. 2-12, 1993.

[82] V. Supradeepa, D. Leaird, and A. Weiner, "Fourier pulse shaping with enhanced spectral control using a 2-D VIPA grating pulse shaper," in *2008 Conference on Lasers and Electro-Optics and 2008 Conference on Quantum Electronics and Laser Science*, 2008: IEEE, pp. 1-2.

[83] F. Verluise, V. Laude, Z. Cheng, C. Spielmann, and P. Tournois, "Amplitude and phase control of ultrashort pulses by use of an acousto-optic programmable dispersive filter: pulse compression and shaping," *Optics letters,* vol. 25, no. 8, pp. 575-577, 2000.

[84] J. Travers *et al.*, "Pulse compression in dispersion decreasing photonic crystal fiber," in *Conference on Lasers and Electro-Optics*, 2007: Optical Society of America, p. CFK1.

[85] F. Druon and P. Georges, "Pulse-compression down to 20 fs using a photonic crystal fiber seeded by a diode-pumped Yb: SYS laser at 1070 nm," *Optics express,* vol. 12, no. 15, pp. 3383-3396, 2004.

[86] L. Vuong *et al.*, "Optimal pulse compression via sequential filamentation," in *Photonic Applications Systems Technologies Conference*, 2007: Optical Society of America, p. JWE1.

[87] R. Salem, M. A. Foster, A. C. Turner, D. F. Geraghty, M. Lipson, and A. L. Gaeta, "Signal regeneration using low-power four-wave mixing on silicon chip," *Nature photonics,* vol. 2, no. 1, pp. 35-38, 2008.

[88] "R. Paschotta. RP Photonics Encyclopedia access from: https://www.rpphotonics.com/encyclopedia.html." (accessed 2022).

[89] "S. Addanki, I. S. Amiri, and P. Yupapin. Review of optical fibers-introduction and applications in fiber lasers. Results in Physics, 10:743–750, 2018.."

[90] W. A. Gambling, "The rise and rise of optical fibers," *IEEE journal of selected topics in quantum electronics,* vol. 6, no. 6, pp. 1084-1093, 2000.

[91] V. N. Kothalawala, "PULSE DYNAMICS OF PASSIVELY MODE-LOCKED POLARIZATION MAINTAINING FIBER LASERS," Master, Lappeenranta-Lahti University of Technology LUT, 2021.

[92] W. Liu, "Advanced ultrafast fiber laser sources enabled by fiber nonlinearities," Staats-und Universitätsbibliothek Hamburg Carl von Ossietzky, 2016.

[93] C. Huang *et al.*, "Rare earth doped optical fibers with multi-section core," *Iscience,* vol. 22, pp. 423-429, 2019.

[94] F. Sidiroglou, A. Roberts, and G. Baxter, "Contributed Review: A review of the investigation of rare-earth dopant profiles in optical fibers," *Review of Scientific Instruments,* vol. 87, no. 4, p. 041501, 2016.

[95] V. N. Kothalawala, "Pulse dynamics of passively mode-locked polarization maintaining fiber lasers," 2021.

[96] R. Paschotta, J. Nilsson, A. C. Tropper, and D. C. Hanna, "Ytterbium-doped fiber amplifiers," *IEEE Journal of quantum electronics,* vol. 33, no. 7, pp. 1049-1056, 1997.

[97] 오민 *et al.*, "Measurement of the absorption coefficient of Yb-doped fibers by a side light analysis," *새물리,* vol. 67, no. 4, pp. 499-503, 2017.

[98] M. N. Zervas, "High power ytterbium-doped fiber lasers—fundamentals and applications," *International Journal of Modern Physics B,* vol. 28, no. 12, p. 1442009, 2014.

[99] Y. Wang, "Optimization of pulse amplification in ytterbium-doped double-clad fiber amplifiers," *Journal of lightwave technology,* vol. 23, no. 6, p. 2139, 2005.

[100] K. Igarashi, D. Souma, T. Tsuritani, and I. Morita, "Performance evaluation of selective mode conversion based on phase plates for a 10-mode fiber," *Optics express,* vol. 22, no. 17, pp. 20881-20893, 2014.

[101] "https://www.fiberlabs.com/glossary/optical-fiber/." (accessed 2022).

[102] J. Daniel, J. Chan, J. Kim, J. Sahu, M. Ibsen, and W. Clarkson, "Novel technique for mode selection in a multimode fiber laser," *Optics express,* vol. 19, no. 13, pp. 12434-12439, 2011.

[103] R. Shahzadi, A. Shahzad, F. Qamar, R. Shahzadi, and M. Ali, "Effective refractive index and v-parameter characterization for guided modes in multimode, nano and three layer optical fibers," *International Journal of Information Technology and Electrical Engineering,* vol. 7, no. 3, 2018.

[104] M. Arumugam, "Optical fiber communication—An overview," *Pramana,* vol. 57, no. 5, pp. 849-869, 2001.

[105] P. Clarricoats, J. Arnold, and G. Crone, "Transmission characteristics of graded-index fibers," *Fiber & Integrated Optics,* vol. 2, no. 2, pp. 145-160, 1979.

[106] "Optical fibers. https://www.miniphysics.com/optical-fibres.html." (accessed 2022).

[107] C. Emslie, A. Méndez, and T. Morse, "Polarization maintaining fibers," ed: Academic, 2007, pp. 243-277.

[108] J. Szczepanek, T. M. Kardaś, C. Radzewicz, and Y. Stepanenko, "Ultrafast laser mode-locked using nonlinear polarization evolution in polarization maintaining fibers," *Optics Letters,* vol. 42, no. 3, pp. 575-578, 2017.

[109] S. Ezekiel and H. J. Arditty, *Fiber-Optic Rotation Sensors and Related Technologies: Proceedings of the First International Conference MIT, Cambridge, Mass., USA, November 9–11, 1981*. Springer, 2013.

[110] A. R. Bahrampour, S. Tofighi, M. Bathaee, and F. Farman, "Optical fiber interferometers and their applications," *Interferometry-Research and Applications in Science and Technology,* vol. 1, pp. 3-30, 2012.

[111] W. Zheng, "Auto-aligning and splicing PM-fibers of different types with a passive method," in *Fiber Optic Gyros: 20th Anniversary Conference*, 1996, vol. 2837: SPIE, pp. 356-367.

[112] A. D. Yablon, *Optics of fusion splicing*. Springer, 2005.

[113] J. Noda, K. Okamoto, and Y. Sasaki, "Polarization-maintaining fibers and their applications," *Journal of Lightwave Technology,* vol. 4, no. 8, pp. 1071-1089, 1986.

[114] R. Ulrich, S. Rashleigh, and W. Eickhoff, "Bending-induced birefringence in single-mode fibers," *Optics letters,* vol. 5, no. 6, pp. 273-275, 1980.

[115] J. Limpert *et al.*, "High-average-power picosecond Yb-doped fiber amplifier," *Optics Letters,* vol. 26, no. 23, pp. 1849-1851, 2001.

[116] N. Broderick, H. Offerhaus, D. Richardson, R. Sammut, J. Caplen, and L. Dong, "Large mode area fibers for high power applications," *Optical Fiber Technology,* vol. 5, no. 2, pp. 185-196, 1999.

[117] M.-J. Li *et al.*, "Effective area limit for large mode area laser fibers," in *OFC/NFOEC 2008-2008 Conference on Optical Fiber Communication/National Fiber Optic Engineers Conference*, 2008: IEEE, pp. 1-3.

[118] H. L. Offerhaus, J. A. Alvarez-Chavez, J. Nilsson, P. Turner, W. Clarkson, and D. Richardson, "Multi-mJ, multi-Watt Q-switched fiber laser," in *Technical Digest. Summaries of papers presented at the Conference on Lasers and Electro-Optics. Postconference Edition. CLEO'99. Conference on Lasers and Electro-Optics (IEEE Cat. No. 99CH37013)*, 1999: IEEE, pp. CPD10/1-CPD10/2.

[119] "https://www.rp-photonics.com/fiber_coupled_diode_lasers.html." (accessed 2022).

[120] "https://www.rp-photonics.com/fiber_couplers.html." (accessed 2022).

[121] "https://www.rp-photonics.com/fiber_connectors.html." (accessed 2022).

[122] "https://www.rp-photonics.com/fiber_collimators.html." (accessed 2022).

[123] "Optical Isolators from: https://www.rp-photonics.com/optical_isolators.html." (accessed 2022).

[124] "Saturable Absorbers from: https://www.rp-photonics.com/saturable_absorbers.html." (accessed 2022).

[125] "Wavelength Division Multiplexing from: https://www.rp-photonics.com/wavelength_division_multiplexing.html." (accessed 2022).

[126] "Fiber-optic Pump Combiners from: https://www.rp-photonics.com/fiber_optic_pump_combiners.html." (accessed 2022).

[127] "Fiber Bragg Gratings from: https://www.rp-photonics.com/fiber_bragg_gratings.html." (accessed 2022).

[128] "FBG Principle from: https://fbgs.com/technology/fbg-principle/." (accessed 2022).

[129] S. Kobtsev, S. Smirnov, S. Kukarin, and S. Turitsyn, "Mode-locked fiber lasers with significant variability of generation regimes," *Optical Fiber Technology,* vol. 20, no. 6, pp. 615-620, 2014.

[130] S. W. Harun and H. Arof, *Current developments in optical fiber technology*. BoD–Books on Demand, 2013.

[131] C. K. Nielsen, "Mode locked fiber lasers: theoretical and experimental developments," *IEEE J. Sel. Top. Quantum Electron,* vol. 10, no. 1, pp. 129-136, 2006.

[132] N. Meiser, "Novel Technologies for Mode-Locking of Solid-State Lasers," KTH Royal Institute of Technology, 2013.

[133] F. Frank, "Generation and application of ultrashort laser pulses in attosecond science," Imperial College London, 2011.

[134] A. Isomäki, *Ultrafast Fiber Lasers Using Novel Semiconductor Saturable Absorbers and Photonic-Crystal Dispersion Compensators*. Tampere University of Technology, 2007.

[135] T. F. Carruthers and I. N. Duling, "10-GHz, 1.3-ps erbium fiber laser employing soliton pulse shortening," *Optics Letters,* vol. 21, no. 23, pp. 1927-1929, 1996.

[136] T. Wang, W. Ma, Q. Jia, Q. Su, P. Liu, and P. Zhang, "Passively mode-locked fiber lasers based on nonlinearity at 2-µm band," *IEEE Journal of Selected Topics in Quantum Electronics,* vol. 24, no. 3, pp. 1-11, 2017.

[137] L. F. Mollenauer and R. H. Stolen, "Erratum: The soliton laser [Opt. Lett. 9, 14-16 (1984)," *Optics Letters,* vol. 9, no. 3, p. 105, 1984.

[138] L. F. Mollenauer and R. H. Stolen, "The soliton laser," *Optics letters,* vol. 9, no. 1, pp. 13-15, 1984.

[139] M. Hofer, M. E. Fermann, F. Haberl, M. Ober, and A. Schmidt, "Mode locking with cross-phase and self-phase modulation," *Optics letters,* vol. 16, no. 7, pp. 502-504, 1991.

[140] G. Agrawal, "Nonlinear Fiber Optics 3rd edn (New York: Academic)," 2001.

[141] G. Agrawal, "Nonlinear Fiber Optics 3rd edition, 2001 Academic Press," *San Diego*.

[142] R. S. mohammadabadi, "Towards the advanced high-energy multidimensional laser technology through harnessing the spatiotemporal nonlinear enhancement," PHD, EMT, INRS, 2020.

[143] F. Shimizu, "Frequency broadening in liquids by a short light pulse," *Physical Review Letters,* vol. 19, no. 19, p. 1097, 1967.

[144] C. Finot, F. Chaussard, and S. Boscolo, "Simple guidelines to predict self-phase modulation patterns," *JOSA B,* vol. 35, no. 12, pp. 3143-3152, 2018.

[145] "A. E. Siegman, Lasers (Oxford University Press, 1986).".

[146] R. H. Stolen and C. Lin, "Self-phase-modulation in silica optical fibers," *Physical Review A,* vol. 17, no. 4, p. 1448, 1978.

[147] R. Szipöcs, K. Ferencz, C. Spielmann, and F. Krausz, "Chirped multilayer coatings for broadband dispersion control in femtosecond lasers," *Optics letters,* vol. 19, no. 3, pp. 201-203, 1994.

[148] H. A. Haus, J. G. Fujimoto, and E. P. Ippen, "Analytic theory of additive pulse and Kerr lens mode locking," *IEEE Journal of quantum electronics,* vol. 28, no. 10, pp. 2086-2096, 1992.

[149] "S. M. J. Kelly. Electronics Letters, 28:806–807(1), April 1992.."

[150] K. Tamura, E. Ippen, H. Haus, and L. Nelson, "77-fs pulse generation from a stretched-pulse mode-locked all-fiber ring laser," *Optics letters,* vol. 18, no. 13, pp. 1080-1082, 1993.

[151] A. Chong, J. Buckley, W. Renninger, and F. Wise, "All-Normal-Dispersion Femtosecond Fiber Laser with Pulse-Shaping due to Spectral Filtering," in *Advanced Solid-State Photonics*, 2007: Optical Society of America, p. ME5.

[152] A. Cabasse, B. Ortaç, G. Martel, A. Hideur, and J. Limpert, "Dissipative solitons in a passively mode-locked Er-doped fiber with strong normal dispersion," *Optics express,* vol. 16, no. 23, pp. 19322-19329, 2008.

[153] X. Liu, "Numerical and experimental investigation of dissipative solitons in passively mode-locked fiber lasers with large net-normal-dispersion and high nonlinearity," *Optics Express,* vol. 17, no. 25, pp. 22401-22416, 2009.

[154] Z. Zhang and P. Liang, "All-normal-dispersion dissipative soliton Yb fiber laser," in *Asia Communications and Photonics Conference and Exhibition*, 2010: Optica Publishing Group, p. 79860V.

[155] "B. Braun, F. X. Kärtner, G. Zhang, M. Moser, and U. Keller,"56-ps passively Q-switched diode-pumped microchip laser," OpticsLetters, vol. 22, no. 6, pp. 381–383, 1997. [Online]. Available: http://ol.osa.org/abstract.cfm?URI=ol-22-6-381."

[156] S. Kivisto, R. Herda, and O. G. Okhotnikov, "Electronically tunable Yb-doped mode-locked fiber laser," *IEEE Photonics technology letters,* vol. 20, no. 1, pp. 51-53, 2007.

[157] T. Yu, E. A. Golovchenko, A. N. Pilipetskii, and C. R. Menyuk, "Dispersion-managed soliton interactions in optical fibers," *Optics Letters,* vol. 22, no. 11, pp. 793-795, 1997/06/01 1997, doi: 10.1364/OL.22.000793.

[158] U. Klotzbach, "Untersuchungen zum Trennen von polykristallinen Siliziumwafern mit frequenzverfielfachten Kurzpuls-Nd: YAG-Lasern," 2006.

[159] v. von, "Fiber Laser Master Oscillators for Optical Synchronization Systems," zur Erlangung des Doktorgrades des Department Physik der Universit ¨ at Hamburg, 2008.

[160] "A. J. DeMaria, D. A. Stetser, and H. Heynau, "Self mode-locking of lasers with saturable absorbers," Applied Physics Letters, vol. 8, no. 7, pp. 174–176,

1966. [Online]. Available: http://link.aip.org/link/?APL/8/174/1."

[161] "A. J. DeMaria, C. M. Ferrar, and G. E. Danielson, Jr., "Mode locking of a Nd3+-doped glass laser," Applied Physics Letters, vol. 8, no. 1, pp. 22–24,

1966. [Online]. Available: http://link.aip.org/link/?APL/8/22/1."

[162] "E. P. Ippen, "Principles of passive mode locking," Applied Physics B: Lasers and Optics, vol. 58, no. 3, pp. 159–170, March 1994.."

[163] V. Liverini, S. Schön, R. Grange, M. Haiml, S. Zeller, and U. Keller, "Low-loss GaInNAs saturable absorber mode locking a 1.3-μ m solid-state laser," *Applied Physics Letters,* vol. 84, no. 20, pp. 4002-4004, 2004.

[164] U. Keller, "Recent developments in compact ultrafast lasers," *nature*, vol. 424, no. 6950, pp. 831-838, 2003.

[165] U. Keller *et al.*, "Semiconductor saturable absorber mirrors (SESAM's) for femtosecond to nanosecond pulse generation in solid-state lasers," *IEEE Journal of selected topics in QUANTUM ELECTRONICS*, vol. 2, no. 3, pp. 435-453, 1996.

[166] R. Herda, *Semiconductor mirrors for ultrafast fiber technology*. Tampere University of Technology, 2006.

[167] S. Schmitt-Rink, D. Chemla, and D. A. Miller, "Theory of transient excitonic optical nonlinearities in semiconductor quantum-well structures," *Physical Review B*, vol. 32, no. 10, p. 6601, 1985.

[168] L. E. Nelson, D. Jones, K. Tamura, H. A. Haus, and E. Ippen, "Ultrashort-pulse fiber ring lasers," *Applied Physics B: Lasers & Optics*, vol. 65, no. 2, 1997.

[169] "Mode Locking of Fiber Lasers at High Repetition Rates by Nicholas G. Usechak-page16."

[170] N. Ji, J. C. Magee, and E. Betzig, "High-speed, low-photodamage nonlinear imaging using passive pulse splitters," *Nature methods*, vol. 5, no. 2, pp. 197-202, 2008.

[171] "R. Paschotta. RP Photonics Encyclopedia. https://www.rpphotonics.com/encyclopedia.html." (accessed.

[172] I. A. Walmsley and C. Dorrer, "Characterization of ultrashort electromagnetic pulses," *Advances in Optics and Photonics*, vol. 1, no. 2, pp. 308-437, 2009.

[173] "R. Trebino and E. Zeek. pages 61–99. Springer US, Boston, MA, 2000."

[174] R. Trebino, *Frequency-Resolved Optical Gating: The Measurement of Ultrashort Laser Pulses: The Measurement of Ultrashort Laser Pulses*. Springer Science & Business Media, 2000.

[175] L. Zhang, A. El-Damak, Y. Feng, and X. Gu, "Experimental and numerical studies of mode-locked fiber laser with large normal and anomalous dispersion," *Optics express*, vol. 21, no. 10, pp. 12014-12021, 2013.

[176] "Diffraction gratings from: https://www.newport.com/n/pulse-compression-diffraction-gratings." (accessed.

[177] " Diffraction gratings from: https://ibsen.com/wp-content/uploads/White-paper-Pulse-stretching-and-compressing-using-grating-pairs_v1-1.pdf." (accessed.

[178] "https://ibsen.com/products/transmissiongratings/pulsecompressiongratings/gclid=CjwKCAiAwomeBhBWEiwAM43YIBJ4tKegnHIDVSQZZBbA3PxclgiitQmqKIlK25Xz-y2OGehutn93RBoCTecQAvD_BwE." (accessed 2022).

[179] " Average-and-Peak-Power-Calculation from: https://www.newport.com/medias/sys_master/images/images/h8f/h7a/8797052108830/Average-and-Peak-Power-Calculation-Tech-Note-1.pdf." (accessed.

[180] S. Watanabe, "Novel fiber Kerr-switch with parametric gain: demonstration of optical demultiplexing and sampling up to 640 Gb/s," *ECOC 2004, PDP, Stockholm, Sweden*, 2004.

[181] M. Attygalle, A. Nirmalathas, and H. Liu, "All-optical coding of mode-locked semiconductor laser pulse trains for high bit rate optical communications," *Optics communications*, vol. 217, no. 1-6, pp. 161-167, 2003.

[182] A. Kudlinski, B. Barviau, A. Leray, C. Spriet, L. Héliot, and A. Mussot, "Control of pulse-to-pulse fluctuations in visible supercontinuum," *Optics express,* vol. 18, no. 26, pp. 27445-27454, 2010.

[183] "https://www.rp-photonics.com/modulation_depth.html." (accessed.

[184] "https://www.batop.de/information/SAM_infos.html," 2022.

[185] C. G. Alfieri, A. Diebold, F. Emaury, E. Gini, C. J. Saraceno, and U. Keller, "Improved SESAMs for femtosecond pulse generation approaching the kW average power regime," *Optics express,* vol. 24, no. 24, pp. 27587-27599, 2016.

[186] R. Grange *et al.*, "New regime of inverse saturable absorption for self-stabilizing passively mode-locked lasers," *Applied Physics B,* vol. 80, no. 2, pp. 151-158, 2005.

[187] P. Langlois *et al.*, "High fluence ultrafast dynamics of semiconductor saturable absorber mirrors," *Applied Physics Letters,* vol. 75, no. 24, pp. 3841-3843, 1999.

[188] T. Südmeyer *et al.*, "High-power ultrafast thin disk laser oscillators and their potential for sub-100-femtosecond pulse generation," *Applied Physics B,* vol. 97, no. 2, pp. 281-295, 2009.

[189] C. J. Saraceno *et al.*, "Cutting-edge high-power ultrafast thin disk oscillators," *Applied Sciences,* vol. 3, no. 2, pp. 355-395, 2013.

[190] U. Keller, "Landolt-Börnstein: Laser Physics and Applications, ch. 2," ed: Springer-Verlag, 2007.

[191] J. A. Der Au, D. Kopf, F. Morier-Genoud, M. Moser, and U. Keller, "60-fs pulses from a diode-pumped Nd: glass laser," *Optics letters,* vol. 22, no. 5, pp. 307-309, 1997.

[192] C. J. Saraceno *et al.*, "SESAMs for high-power oscillators: design guidelines and damage thresholds," *IEEE Journal of Selected Topics in Quantum Electronics,* vol. 18, no. 1, pp. 29-41, 2011.

[193] "https://www.gentec-eo.com/laser-calculators/energy-density-fluence," 2022.

[194] "https://www.calctool.org/optics/laser-pulse," 2022.

[195] "https://www.omnicalculator.com/physics/laser-spot-size," 2022.

[196] M. Oelgemöller and G. Vamvounis, "International year of light and light-based technologies," *Australian Journal of Chemistry,* vol. 68, no. 11, pp. 1619-1620, 2015.

[197] "International Year of Light and Light Based Technologies, About the Year of Light, FAQ, website. Available (accessed on 2022): http://www.light2015.org/Home/About/FAQ.html."

[198] S. F. Ray, *Applied photographic optics: Lenses and optical systems for photography, film, video, electronic and digital imaging*. Routledge, 2002.

[199] W. J. Croft, *Under the microscope: a brief history of microscopy*. World Scientific, 2006.

[200] P. Franken, A. E. Hill, C. e. Peters, and G. Weinreich, "Generation of optical harmonics," *Physical Review Letters,* vol. 7, no. 4, p. 118, 1961.

[201] G. New, *Introduction to nonlinear optics*. Cambridge University Press, 2011.

[202] " Boyd R., Nonlinear Optics Second Edition, Academic Press, San Diego, (2003)."

[203] Y.-R. Shen, "Principles of nonlinear optics," 1984.

[204] I. W. L. Au, "The Design and Construction of a Second Harmonic Generation Microscope For Collagen Imaging," 2012.

[205] R. Boyd, "Nonlinear Optics 3rd edn, Ch. 9," ed: Elsevier, 2008.

[206] P. Guyot-Sionnest, W. Chen, and Y. Shen, "General considerations on optical second-harmonic generation from surfaces and interfaces," *Physical Review B,* vol. 33, no. 12, p. 8254, 1986.

[207] A. Yariv and P. Yeh, *Photonics: optical electronics in modern communications*. Oxford university press, 2007.

[208] P. N. Prasad and D. J. Williams, *Introduction to nonlinear optical effects in molecules and polymers*. Wiley New York, 1991.

[209] H. Liu, J. Yao, and A. Puri, "Second and third harmonic generation in BBO by femtosecond Ti: sapphire laser pulses," *Optics communications,* vol. 109, no. 1-2, pp. 139-144, 1994.

[210] A. Aghigh, S. Bancelin, M. Rivard, M. Pinsard, H. Ibrahim, and F. Légaré, "Second harmonic generation microscopy: a powerful tool for bio-imaging," *Biophysical Reviews,* pp. 1-28, 2023.

[211] R. W. Boyd, *Nonlinear optics*. Academic press, 2020.

[212] D. Eimerl, L. Davis, S. Velsko, E. Graham, and A. Zalkin, "Optical, mechanical, and thermal properties of barium borate," *Journal of applied physics,* vol. 62, no. 5, pp. 1968-1983, 1987.

[213] R. C. Eckardt, H. Masuda, Y. X. Fan, and R. L. Byer, "Absolute and relative nonlinear optical coefficients of KDP, KD* P, BaB/sub 2/O/sub 4/, LiIO/sub 3/, MgO: LiNbO/sub 3/, and KTP measured by phase-matched second-harmonic generation," *IEEE Journal of Quantum Electronics,* vol. 26, no. 5, pp. 922-933, 1990.

[214] T. Honma, Y. Benino, T. Fujiwara, R. Sato, and T. Komatsu, "Spatially selected crystallization in glass by YAG laser irradiation," *Journal of non-crystalline solids,* vol. 345, pp. 127-131, 2004.

[215] R. Akbari and A. Major, "Optical, spectral and phase-matching properties of BIBO, BBO and LBO crystals for optical parametric oscillation in the visible and near-infrared wavelength ranges," *Laser Physics,* vol. 23, no. 3, p. 035401, 2013.

[216] S. Brasselet, "Polarization-resolved nonlinear microscopy: application to structural molecular and biological imaging," *Advances in Optics and Photonics,* vol. 3, no. 3, p. 205, 2011.

[217] B. Di Bartolo and J. Collins, *Biophotonics: Spectroscopy, Imaging, Sensing, and Manipulation*. Springer, 2010.

[218] P. N. Prasad, *Introduction to biophotonics*. John Wiley & Sons, 2003.

[219] R. Carriles *et al.*, "Invited review article: Imaging techniques for harmonic and multiphoton absorption fluorescence microscopy," *Review of scientific instruments,* vol. 80, no. 8, p. 081101, 2009.

[220] G. Bautista, M. J. Huttunen, J. M. Kontio, J. Simonen, and M. Kauranen, "Third-and second-harmonic generation microscopy of individual metal nanocones using cylindrical vector beams," *Optics express,* vol. 21, no. 19, pp. 21918-21923, 2013.

[221] M. J. Huttunen, G. Bautista, M. Decker, S. Linden, M. Wegener, and M. Kauranen, "Nonlinear chiral imaging of subwavelength-sized twisted-cross gold nanodimers," *Optical Materials Express,* vol. 1, no. 1, pp. 46-56, 2011.

[222] M. Kauranen and A. V. Zayats, "Nonlinear plasmonics," *Nature photonics,* vol. 6, no. 11, pp. 737-748, 2012.

[223] M. Oheim, D. J. Michael, M. Geisbauer, D. Madsen, and R. H. Chow, "Principles of two-photon excitation fluorescence microscopy and other nonlinear imaging approaches," *Advanced drug delivery reviews,* vol. 58, no. 7, pp. 788-808, 2006.

[224] J. A. Squier, M. Müller, G. Brakenhoff, and K. R. Wilson, "Third harmonic generation microscopy," *Optics express,* vol. 3, no. 9, pp. 315-324, 1998.

[225] H. Fritjof and D. Winfried, "Deep tissue two-photon microscopy," *Nature Methods,* vol. 2, no. 12, pp. 932-940, 2005.

[226] G. Cox, "Biological applications of second harmonic imaging," *Biophysical reviews,* vol. 3, pp. 131-141, 2011.

[227] F. S. Pavone and P. J. Campagnola, *Second harmonic generation imaging*. CRC Press Boca Raton, 2014.

[228] "Second-harmonic generation - Wikiwand [Internet]. [cited 2020 Mar 27]. Available from: https://www.wikiwand.com/en/Second-harmonic_generation." (accessed.

[229] P. Pantazis, J. Maloney, D. Wu, and S. E. Fraser, "Second harmonic generating (SHG) nanoprobes for in vivo imaging," *Proceedings of the National Academy of Sciences,* vol. 107, no. 33, pp. 14535-14540, 2010.

[230] S. Bancelin *et al.*, "Second Harmonic Generation imaging of collagen fibrillogenesis," in *The European Conference on Lasers and Electro-Optics*, 2013: Optica Publishing Group, p. CL_P_4.

[231] Y. Shao *et al.*, "Addressable, large-field second harmonic generation microscopy based on 2D acousto-optical deflector and spatial light modulator," *Applied Physics B,* vol. 108, pp. 713-716, 2012.

[232] N. Kirkpatrick *et al.*, "Video-rate resonant scanning multiphoton microscopy: An emerging technique for intravital imaging of the tumor microenvironment," *Intravital,* vol. 1, no. 1, pp. 60-68, 2012.

[233] C. Macias-Romero, V. Zubkovs, S. Wang, and S. Roke, "Wide-field medium-repetition-rate multiphoton microscopy reduces photodamage of living cells," *Biomedical optics express,* vol. 7, no. 4, pp. 1458-1467, 2016.

[234] D. Tokarz, R. Cisek, A. Golaraei, S. L. Asa, V. Barzda, and B. C. Wilson, "Ultrastructural features of collagen in thyroid carcinoma tissue observed by polarization second harmonic generation microscopy," *Biomedical Optics Express,* vol. 6, no. 9, pp. 3475-3481, 2015.